

# Detailed chemical abundances of neutron-capture elements - from 523 local giant stars

*Rebecca Forsberg*

---

Lund Observatory  
Lund University



2019-EXA147

Degree project of 60 higher education credits (for a degree of Master)  
May 2019

Supervisor: Henrik Jönsson

Lund Observatory  
Box 43  
SE-221 00 Lund  
Sweden

## Abstract

*Purpose:* The purpose of this work is to determine the abundances of neutron-capture elements in solar neighborhood giant stars. This enables constraints to be put on the the cosmic origin of these elements. I have determined abundances of elements produced in both the weak s-process (Cu), the first and second s-process peaks (Y, Zr and La, Ce, Pr, Nd, respectively) and the r-process (Eu, Gd). The weak s-process is predicted to take place in the interior of massive stars, whereas the main s-process takes place in low-mass AGB stars. There are still several possibilities for production sites of the r-process. Comparing the abundances of these elements for a range of stellar metallicities can increase the understanding of their production sites and give clues to the evolution of the Galaxy.

*Method:* The stellar sample consists of 523 giant stars in the local disk, all observed with the optical high-resolution spectrograph FIES at the Nordic Optical Telescope, on La Palma. The abundance determination is done by synthesising line profiles and comparing them to observed data. The use of giant stars in this work prepares for further and deeper probing of the Galaxy and its components. In addition, I can minimise the possible systematic uncertainties that comes with analysing giant stars. The stellar sample is divided into separate stellar populations, primarily based on chemistry and secondarily on kinematics.

*Results:* The abundances determined are of high accuracy and compare well with previous work done on dwarf stars. This high quality allows outliers in the data to be found in addition to tracing the disk populations. In general I find that the thin disk is enriched in s-process-dominated elements, whilst the thick disk is enriched in r-process-dominated elements. The time delay of AGB stars becomes very clear in my results as well as allowing for detailed investigation of the first and second s-process peaks. I also note that the r-process-dominated elements have similar features as that of  $\alpha$ -elements.

*Conclusions:* With careful spectral analysis, detailed abundance determination of giant stars is possible, allowing measurements of distant stars at high resolution to be made. This is important for constraining models of the Galactic evolution and permits accurate abundance determinations of the neutron-capture elements.

## Acknowledgements

*I would like to thank my supervisor Henrik Jönsson for his constant support and encourage throughout this thesis. I am specially thankful in him for trusting me to conduct observations using the NOT on my own, allowing me to grow as an astronomy student. I would also like to give my deepest of thanks to Nils Ryde, Brian Thorsbro, Maria Lomaeva, and Ivalu Barlach Christensen for all the help of interpreting data, solving problems and for all rewarding discussions. A special thanks to Colin Carlile for feedback and being the best desk-mate anyone could wish for and to Ross Church and Thomas Ronnet for feedback and corrections. Finally, endless gratitude to Johan Appलगren for never-ending support.*



## Populärvetenskaplig beskrivning

*Tiden går, om hundra år  
är du stjärndamm, min vän*

- kent, Om gyllene år

Grundämnena, som bygger upp komplexa molekyler som vårt DNA, är samma material som stjärnor består av. Faktum är att vi människor består till 93 % av så kallat stjärnstoft, eller stjärndamm. De simplaste ämnena, väte och helium, skapades i Big Bang, för ungefär 13,7 miljarder år sedan. De resterande 90 ämnena i periodiska systemet bildas i olika typer av stjärnor och i detta arbete har jag tagit fram fler ledtrådar till var, och hur, några av de tyngsta grundämnena skapas.

Precis som människor finns det stjärnor som är unga, gamla, lite mindre och lite större. Inuti stjärnor pågår fusion, sammanslagning av grundämnen till tyngre sådana, vilket frigör den energi som ger uppehov till stjärnors sken. Denna process pågår tills dess att fusion inte längre kan frigöra mer energi, vilket sker när hela stjärnans kärna består av renaste järn.

När energi slutar att flöda ut ur stjärnan, börjar materia istället flöda inåt mot stjärnans mitt. Slutligen blir kärnan så pass massiv att atomerna inte kan hålla emot det gravitationella trycket vilket leder till en kollaps. Kollapsen resulterar i en explosion (en så kallad supernova) som lämnar efter sig ett svart hål, eller den lite mindre massiva varianten, en neutronstjärna.

Stjärnans massa avgör dess livsöde. Desto mer massa, desto snabbare går hela utvecklingsprocessen. Mer massa innebär också högre temperatur – som att en varmare ugn skulle bränna upp din mat snabbare än en svalare. Med snabbare talar vi om miljoner år, till skillnad från de mindre och lättare stjärnorna, så som solen, som kan brinna i miljarder år. De mest massiva stjärnorna väger som 100 solar. De mindre stjärnorna (mindre än 10 solmassor), med lägre temperaturer, fusionerar endast upp till grundämnen som kol och syre innan de långsamt tynar bort till vita dvärgar.

Hur bildas de resterande två tredjedelar av grundämnen, de som är tyngre än järn? Själva produktionen sker genom att neutroner tränger in i atomkärnan vilket skapar tyngre isotoper som sönderfaller till tyngre grundämnen. Beroende på mängden neutroner kan olika grundämnen skapas. Vi kallar dessa ämnen för neutroninfångarämnena, vilket är ämnena som jag undersökt i detta arbete.

Ungefär hälften av grundämnena tyngre än järn i det periodiska systemet skapas under dödsprocessen hos de lättare stjärnorna, innan de blir vita dvärgar. Under några miljoner år sväller dessa stjärnor och blir jättestjärnor. I detta stadie finns neutroner tillgängliga i stjärnans inre, vilket skapar neutroninfångarämnena.

Dock har denna neutronmängd visat sig inte vara tillräcklig för att skapa de allra tyngsta grundämnena. Här är vi astronomer faktiskt inte riktigt säkra på vilken mekanism i universum som kan förklara förekomsten av ämnena, men den extremt höga tillgängligheten av neutroner som krävs begränsar möjliga produktionsplatser till explosiva miljöer, så som supernovor eller krockar mellan neutronstjärnor.

Genom att försöka svara på frågorna kring grundämnenas uppkomst kan astronomer även få ledtrådar i pusslet för att förstå hur vår galax, Vintergatan, har skapats. Vintergatan består av flera hundra miljarder stjärnor, där de flesta stjärnor finns i galaxens skiva. Halterna av ämnen bildade genom neutroninfångning i både gamla och unga stjärnor i Vintergatans skiva ger oss en bättre uppfattning om hur den såg ut när dessa stjärnor skapades. Detta låter oss tyda vilka processer som krävs och hur Vintergatan har utvecklats med tiden.

Frågor som *Fanns det många tunga ämnen redan i ett tidigt stadie av galaxens utveckling?* och *Har något tillkommit eller förändrats i Galaxen som resulterat i en högre produktion av grundämnen?* har jag undersökt genom att samla in spektroskopisk data, alltså ljus, från stjärnor som är närliggande vår egna sol i galaxskivan. Ljuset är som ett fingeravtryck som avslöjar vilka ämnen stjärnan innehåller, där jättestjärnor har visat sig bevara sin initiala halt av grundämnen bäst i sin atmosfär.

Jättestjärnor är väldigt ljusstarka vilket innebär att de kan observeras på långt avstånd, något som är fördelaktigt när större delar av galaxen, så som dess mittersta, eller yttersta, delar ska utforskas. Då analysen av jättestjärnors fingeravtryck är komplex har den största delen av detta arbete ägnats åt att noggrannt överkomma dessa svårigheter och utveckla en fungerande metod som kan användas för framtida forskning inom samma fält.

Jag analyserar nio stycken ämnen bildade genom neutroninfångning i mitt arbete, ämnen som återfinns här på jorden och i våra kroppar. Denna uppsats är en djupdykning i Galaxens historia och bekräftar ännu en gång att vi alla faktiskt är stjärndamm.



# Contents

<b>1</b>	<b>Introduction</b>	<b>1</b>
<b>2</b>	<b>Scientific background</b>	<b>5</b>
2.1	Nucleosynthesis of elements with $A > 56$	7
2.1.1	s-process	8
2.1.2	p-process	12
2.1.3	r-process	12
2.1.4	Additional neutron-capture processes	13
2.1.5	Elements in this work	14
2.2	Using giant stars	17
<b>3</b>	<b>Stellar sample</b>	<b>20</b>
<b>4</b>	<b>Methodology</b>	<b>24</b>
4.1	Spectral line synthesis	25
4.1.1	Isotope shift and hyperfine splitting	26
4.1.2	Model assumptions	28
4.2	Stellar parameters	31
4.3	Abundance determination	31
4.3.1	Line data	31
4.3.2	Examined lines	33
4.3.3	Solar values	34
4.4	Thin & thick disk separation	34
4.5	Abundance uncertainties	40
4.5.1	Systematic uncertainties	40
4.5.2	Random uncertainties	40
<b>5</b>	<b>Results &amp; discussion</b>	<b>46</b>
5.1	Data selection	47
5.2	Previous work and the disk populations	47
5.2.1	Weak s-process: Cu	48
5.2.2	First s-process peak: Y, Zr	54
5.2.3	Second s-process peak: La, Ce, Pr, Nd	55
5.2.4	r-process: Eu, Gd	56
5.3	Comparison of the neutron-capture elements	58
5.4	s-process enhanced stars	62



5.5	Age estimation using $[Y/Mg]$ . . . . .	63
5.6	Additional elements . . . . .	64
<b>6</b>	<b>Conclusions</b>	<b>66</b>
6.1	Future outlook . . . . .	67
	<b>References</b>	<b>76</b>
	<b>Appendices</b>	<b>77</b>
	<b>Appendix A Synthetic spectral lines</b>	<b>78</b>
	<b>Appendix B Atomic data for spectral lines</b>	<b>85</b>
	<b>Appendix C Additional abundance plots</b>	<b>88</b>
	<b>Appendix D Conference</b>	<b>91</b>

# List of Figures

1.0.1 Schematic Milky Way Galaxy . . . . .	1
2.0.1 Binding energy per nucleon . . . . .	6
2.0.2 Mass classifications . . . . .	7
2.1.1 Schematic of the s- and r-processes . . . . .	9
2.1.2 Periodic table . . . . .	10
2.1.3 Schematic of a kilonova . . . . .	13
2.2.1 Curve of growth and line profile example . . . . .	19
3.0.1 Photographs of the Nordic Optical Telescope . . . . .	20
3.0.2 Positions of stars in stellar sample: Galactic coordinates . . . . .	22
3.0.3 Positions of stars in stellar sample: $(x,y,z)$ -coordinates . . . . .	23
3.0.4 Distances of stars in stellar sample . . . . .	23
4.2.1 HR-diagram of stellar parameters . . . . .	32
4.3.1 Example of spectral lines . . . . .	33
4.4.1 Separation of disk population in $\alpha$ -elements . . . . .	36
4.4.2 Toomre diagram . . . . .	38
4.4.3 Velocity distributions of stellar populations . . . . .	39
4.4.4 Position distribution of stellar populations . . . . .	39
4.5.1 Monte Carlo uncertainties: Arcturus . . . . .	44
4.5.2 Monte Carlo uncertainties: Rasalas . . . . .	45
5.2.1 [Cu/Mg] against [Mg/H] . . . . .	48
5.2.2 Abundance plot for the stellar populations . . . . .	49
5.2.3 Running mean of abundances . . . . .	50
5.2.4 Comparative plot with <a href="#">Mishenina et al. (2013)</a> . . . . .	51
5.2.5 Comparative plot with <a href="#">Bensby et al. (2014)</a> and <a href="#">Battistini &amp; Bensby (2016)</a> . . . . .	52
5.2.6 Comparative plot with <a href="#">Delgado Mena et al. (2017)</a> . . . . .	53
5.2.7 [Cu/Fe] against [Zr,Ce,Eu/Fe] . . . . .	54
5.2.8 Comparative abundance plot - first s-peak elements . . . . .	55
5.2.9 [Eu/ $\alpha$ ] against [Fe/H] . . . . .	57
5.3.1 [Eu/Ce] against [Fe/H] . . . . .	58
5.3.2 [X/Ce] and [X/Eu] against [Fe/H] for X = Y, Zr, La, Pr, Nd, Gd . . . . .	60
5.3.3 Comparative abundances - first and second s-process peak . . . . .	61
5.5.1 [X/Mg] against the estimated stellar ages from <a href="#">Pinsonneault et al. (2018)</a> . . . . .	64

A.0.1Synthetic spectra: Cu . . . . .	78
A.0.2Synthetic spectra: Y . . . . .	79
A.0.3Synthetic spectra: Zr . . . . .	80
A.0.4Synthetic spectra: La . . . . .	81
A.0.5Synthetic spectra: Ce . . . . .	82
A.0.6Synthetic spectra: Pr . . . . .	83
A.0.7Synthetic spectra: Nd . . . . .	83
A.0.8Synthetic spectra: Eu . . . . .	84
A.0.9Synthetic spectra: Gd . . . . .	84
C.0.1[X/Fe] against [Fe/H] . . . . .	88
C.0.2[X/Mg] against [Mg/H] . . . . .	89
C.0.3Running mean of abundances (Mg) . . . . .	90

# List of Tables

2.1	Main s-process contribution . . . . .	15
3.1	information about observational visits . . . . .	21
3.2	Properties of data . . . . .	21
4.1	Isotope information of the elements in the work . . . . .	27
4.2	Elements with hyperfine splitting . . . . .	28
4.3	Determined solar values . . . . .	34
4.4	Stellar parameter comparison with Gaia benchmark stars . . . . .	40
4.5	Determined uncertainties . . . . .	43
5.1	Properties of data - quality cut . . . . .	47
5.2	s-enriched stars . . . . .	62
B.1	Atomic line data . . . . .	85

# Chapter 1

## Introduction

The Milky Way galaxy is an ideal laboratory for galactic research and can be considered a reference case for spiral galaxies in general (Bland-Hawthorn & Gerhard 2016). The key is the proximity, which enables detailed investigations of Galactic origin and evolution. Modern technology allows for high resolution of spectroscopic data of both close and distant stars in the Galaxy, providing a solid foundation for understanding how barred spiral galaxies form and evolve. Detailed studies of the properties and motions of the stars provide a greater understanding of the Milky Way components. It is customary to talk about four main stellar components, apart from the dark matter halo surrounding the whole galaxy. These components are the bulge, or the bar, the disk – which in turn consists of two sub-components, often referred to as the thin and thick disks – and lastly the stellar halo<sup>1</sup>. A schematic picture of this can be seen in Figure 1.0.1.

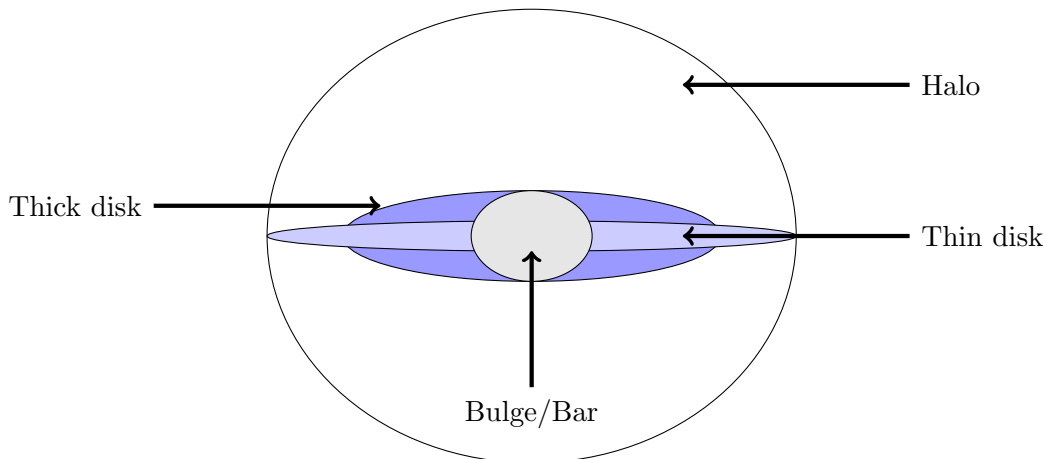


**Figure 1.0.1:** Schematic view of the Milky Way and its components seen edge on, inspired by data in McMillan (2011) and Hayden et al. (2015). Not shown in this figure is that the edge of the thin disk probably flares (Hayden et al. 2015).

---

<sup>1</sup>Throughout this thesis, for readability, the *disk*, *halo* and *the bulge*, or *bar* refers to the Milky Way components, even though they are spelled with lower case letters.

The Milky Way disk is concentrated at the Galactic mid-plane; the disk is often the main feature of spiral galaxies, where the name originates from the spiral structures observed in galaxies with disks. It is of great interest to understand the structure and features of the disk since it contains the majority of the stellar mass in the Galaxy (Bland-Hawthorn & Gerhard 2016). In 1983, Gilmore & Reid discovered that two density profiles are necessary to match the total density distribution of the disk. Following that discovery, several studies have confirmed that the disk consists of two distinct stellar populations often referred to as the thin and thick disk (see e.g. Bensby et al. (2014); Bland-Hawthorn & Gerhard (2016) and references therein).

The classification of the stellar populations in the disk can be done in several ways: by kinematics, age, geometry and chemistry. Even so, the separation of these two components is somewhat debated and the transition between these might be a gradient rather than a clear separation. For instance, the results by Hayden et al. (2015) show that the scale length of the thin disk extends further out than that of the thick disk.

It has been shown that, in general, stars belonging to the thick disk orbit around the Galactic centre at lower velocities (some 40-50 km/s slower), are more metal-poor, older and have a higher abundance of the so called  $\alpha$ -elements at a given metallicity, compared to the stars from the thin disk (see e.g. Bensby et al. (2007, 2014); Adibekyan et al. (2011)). In this work, classification of the disk population is primarily done using the chemical picture, abundance of  $\alpha$ -elements and to some extent kinematics from the second data release from the Gaia project (Gaia DR2) (Gaia Collaboration et al. 2018), see also Section 4.4.

The varying ages of stars enable a look back in the history of the Galaxy; they provide direct samples of the composition of the interstellar medium (ISM) at the time they formed. This is under the assumption that the photosphere remains relatively unchanged during the life of the star, which is the subject of some discussion. Expectations and modelling of the enrichment of the ISM over time tells us that the very oldest stars should only contain hydrogen, helium and lithium, synthesised in the Big Bang, while younger stars should show progressively more abundances of heavy elements. Thus chemical compositions of the stars provides an avenue for exploring the history of the Milky Way. This is known as *Galactic Archaeology*. In this work I aim to shed light on, and provide clues to, the history of the Milky Way by abundance determination of stars. Another way to trace Galactic history is through the stellar motions – kinematics – which I will only touch upon in this work.

In the field of galactic archaeology, several groups of chemical species have been studied already; the  $\alpha$ -elements (e.g. Reddy et al. (2003, 2006); Adibekyan et al. (2012); Bensby et al. (2014); Jönsson et al. (2017a,b) among many others) as well as the so-called iron-peak elements (e.g. Battistini & Bensby (2016); Mikolaitis et al. (2017); Lomaeva et al. (2019) among others). A third group of elements is the *neutron-capture elements*, which are the focus of this work. This group of elements, heavier than iron, provides an alternative timeline for astrophysical phenomena and processes throughout the history of the Galaxy. Moreover, since the neutron-capture elements comprise more than two thirds of the periodic table, the study of these is crucial to an understanding of the full element production throughout the universe.

Chemical abundance measurements for neutron-capture elements in solar neighbourhood stars have been investigated for the past 60 years, beginning with [Baschek \(1959\)](#) and [Aller & Greenstein \(1960\)](#). Over the years the field has developed with more sophisticated analysis and ever larger samples of stars. Results yield the complexity of the neutron-capture elements and their variety of formation channels, making them an important tool in constraining the evolution of the Galaxy and its components.

The neutron-capture elements can be divided into two groups: the slow (s)- and rapid (r)-process elements (discussed more thoroughly in [Section 2.1](#)). In general, the s-process produces the lighter elements after iron, whereas the r-process is the dominating process for the heaviest elements. The production of s-process elements takes place mainly in the interior of asymptotic giant branch (AGB) stars. These stars originate from low to intermediate mass stars ( $0.5\text{-}8 M_{\odot}$ ) ([Herwig 2005](#)) at the end of their life cycle, which results in a complex interior where the more exotic neutron-capture elements can be produced.

AGB stars form from low to intermediate mass stars ( $< 8 M_{\odot}$ ) which have longer lifetimes than heavier mass stars. Thus, there is a time delay for the production of these elements compared to elements syntheses in massive stars. This can be seen in observational data as a gradual increase of s-process elements at a certain metallicity, see for instance [Battistini & Bensby \(2016\)](#); [Delgado Mena et al. \(2017\)](#). This means that any observed s-process-dominated element before this time must be due to at least one additional production channel. A non-negligible proportion of the s-process-dominated elements is likely to originate from the r-process at early times. However, previous observations can not, to a full extent, explain the abundance of these elements at early times, whereas other possibilities of their origin have been proposed. This is elaborated on more in [Section 2.1.4](#).

The theory of the production of s-process elements in stars is better understood than that of the r-process, allowing for a better constraint of the production site. Although it should be noted that rotation of AGB stars is proposed to have a large impact on the production of s-process elements, see [Herwig et al. \(2003\)](#). On the other hand, the production site of the r-process elements has not yet been constrained to specific production sites.

The proposed production sites for r-process elements are various violent events, for instance supernovae and the mergers of heavy bodies in binaries, such as neutron star mergers ([Snedden et al. 2000](#); [Thielemann et al. 2011](#)). However, for a long time, the presence of neutron star mergers in the Universe had not been confirmed, until [Abbott et al. \(2017\)](#) announced the first known neutron star merger, or a *kilonova*, observed by emission of gravitational waves in August 2017. Later on, the electromagnetic counterpart to this merger was also revealed, concluding that r-process elements indeed are produced in these highly energetic, neutron rich, mergers ([Drout et al. 2017](#)). Although, intense discussion and research is still debating to determine whether or not neutron star mergers is the only, or even the dominating, source of r-process elements (see [Côté et al. \(2017, 2018b\)](#); [Siegel et al. \(2018\)](#)). To this day, there are still discrepancies between galactic chemical evolution models and results from observations ([Travaglio et al. 1999](#); [Wanajo 2018](#)).

Since both s- and r-process elements have different production channels than that of  $\alpha$ - and iron peak elements, these can provide an additional time constraint to the Galactic chemical evolution. In order to constrain the yields from different production channels, it is important to have reliable observational abundances to compare with the models. Previous

work on these elements, for example, [Mishenina et al. \(2013\)](#); [Bensby et al. \(2014\)](#); [Battistini & Bensby \(2016\)](#); [Delgado Mena et al. \(2017\)](#); [Guiglion et al. \(2018\)](#), used dwarf stars as probes for investigating the Galactic chemical evolution. As discussed more thoroughly in [Section 2.2](#), there are several advantages of working with dwarf stars. However, they are not as bright as giant stars, limiting the distance at which they can reliably be observed at the same signal-to-noise ratio (S/N) using the same instrumentation.

In the recent review paper on the chemical evolution of the bulge by [McWilliam \(2016\)](#), the necessity of having properly measured abundances for the disk in order to have a reference sample for future bulge measurements is stressed. This is one of the possible future applications of my work. Today, europium (Eu) is the only r-process dominated element (94.0 % of europium is produced in the r-process ([Bisterzo et al. 2014](#))) that has been measured adequately in the bulge, making the r-process branch an unexplored area within this research field ([Van der Swaelmen et al. 2016](#)).

In previous work by [Korn et al. \(2007\)](#); [Lind et al. \(2008\)](#); [Nordlander et al. \(2012\)](#); [Gruyters et al. \(2016\)](#); [Souto et al. \(2019\)](#) and [Liu et al. \(2019\)](#) on the topic of atomic diffusion and mixing in stars, it has been shown that more-evolved stars have systematically higher elemental abundances than dwarf stars, suggesting that abundances measured from dwarf stars are too low. The current hypothesis that provides an explanation is that heavier elements settle into the cores of dwarf stars, depleting the stellar atmosphere making them invisible to us. When the star enters the later stages of its evolution, the convective zones in the stellar interior become larger, once again bringing these elements into the photosphere. These observations strengthen the purpose of having precise abundance measurements from giant stars since these, better than dwarf stars, represent the composition of the gas from which they formed, which is important to measure accurately in order to trace the Galactic evolution.

In this work I have therefore aimed to minimise possible systematic uncertainties when working with giant stars, allowing for future work to probe deeper (for instance the inner and outer disk, the bulge/bar). This also allows detailed abundances of stars in dwarf spheroidal galaxies and ultra faint dwarf galaxies (UFDG) to be obtained. For instance, in [Ji et al. \(2016\)](#) they trace the r-process in early times and at extremely low metallicities, using the UFDG Reticulum II. In a similar way, [Marshall et al. \(2018\)](#) show that the UFDG Tucana II has r-process enrichment, most likely due to early neutron star mergers. For more work within this field, see [Safarzadeh et al. \(2018\)](#); [Cescutti et al. \(2018\)](#); [Duggan et al. \(2018\)](#).

The structure of this thesis is as follows: in [Chapter 2](#) the nucleosynthesis of elements is described, with a focus on the neutron-capture elements. In this chapter I also elaborate upon the use of giant stars in this work and how one can overcome the difficulties that lie in working with these. In [Chapter 3](#) I give a detailed description of the stellar sample used in this work. The methodology, including the abundance determination, assumptions, line list, separation of the disks and uncertainties, is found in [Chapter 4](#). Finally, the results are presented and discussed in [Chapter 5](#). In [Chapter 6](#) I summarise the work, conclusions and findings, and elaborate on possible future extensions.



## Chapter 2

# Scientific background

As a star leaves the main sequence (MS), it enters the final stages of its life cycle. Even though these final stages take place on much shorter timescales than the MS, these stages are significant in many ways. When the stellar core — where fusion occurs — is depleted in hydrogen, the star expands and becomes a red giant, climbing up the red giant branch (RGB) as hydrogen burning takes place in the surrounding hydrogen burning shell. When the core is hot enough to fuse helium in the hydrogen-depleted core, the helium core flash kicks in, moving the star to the horizontal branch (or in the so called red clump for metal-rich stars). When the helium core also is depleted, the outer shell of helium joins the leftover hydrogen burning shell, separated by a (helium) intershell, placing the star on the asymptotic giant branch (AGB), making it an AGB star.

For low- to intermediate-mass stars ( $<8 M_{\odot}$ ), the final stage in the evolution is a planetary nebula and a white dwarf (WD) with a carbon-oxygen core. The nebula is the remnant from the large convective envelope that has been thrown off. Stars heavier than  $10 M_{\odot}$  continue to burn heavier elements in their cores, up to iron (Fe), where fusion of elements stops being exothermic, see Figure 2.0.1. At this stage, the star radiates away its energy without actually releasing energy in the core, which causes the star to heat (stars have negative heat capacity). Due to this increase in temperature, photo-dissociation takes place in the stellar core, until the pressure drops significantly making the star to collapse on itself. The process leads to a supernova, leaving behind either a neutron star or a black hole, depending on the initial stellar mass.

The initial mass is an important parameter since it decides a lot of the post-MS evolution of a star. Therefore some definitions and clarifications of different masses are useful. The definition of low- to intermediate- mass stars is rather vague and debated when it comes to the lower mass limit. In the AGB evolution review by Herwig (2005), the definition of low- to intermediate-mass stars refers to stars with masses of  $\sim 0.5 - 10 M_{\odot}$ , see Figure 2.0.2. In this figure, the resulting AGB- and WD classifications, depending on the initial mass, can be seen. What is relevant to this work is whether or not the AGB star experiences the so-called third dredge-up (TDU) or not. A dredge up is a mechanism when the surface convection zone extends down to the burning shells in the interior of the star. As a result, elements are mixed and products from nucleosynthesis can be brought up to the outer layers of the stellar atmosphere. The third dredge-up occurs in AGB-stars, causing a dredge-up of helium,

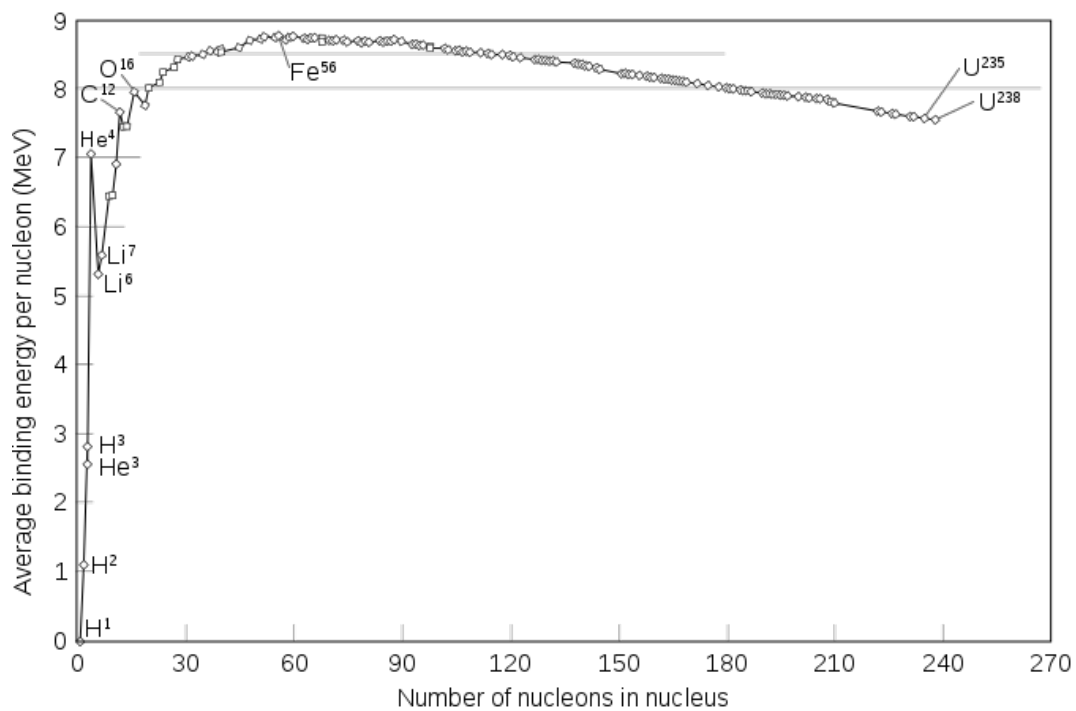


**Figure 2.0.1:** A plot of the binding energy per nucleon. The isotope iron 56 located at the top has the highest binding energy per nucleon and is therefore the heaviest isotope created by fusion in the interior of stars. Source: Wikimedia Commons, [https://commons.wikimedia.org/wiki/File:Binding\\_energy\\_curve\\_-\\_common\\_isotopes.svg](https://commons.wikimedia.org/wiki/File:Binding_energy_curve_-_common_isotopes.svg).

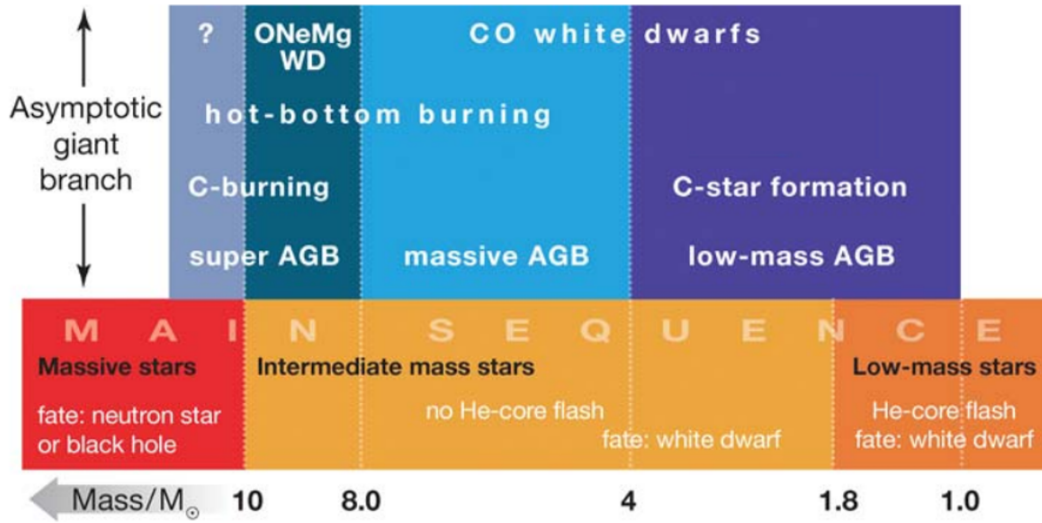


**Figure 2.0.2:** Classification of stars by mass on 1) the MS (lower part) and 2) the AGB (upper part). Approximate limiting masses between different regimes are given at the bottom. It should be noted that these are estimates that depends on assumptions and input of models, as well as on metallicity. The different regimes have been labeled with some characterizing properties. Figure from [Herwig \(2005\)](#).

carbon and heavier elements (s-process elements, described as follows in this chapter) to be brought to the stellar surface. An initial stellar mass of  $1.5 M_{\odot}$  is shown to be a sufficient lower mass limit for TDU to take place, by models from [Lattanzio \(1989\)](#).

The nucleosynthesis that has been covered so far is the one in stars through fusion, leading up to iron. This leaves the question of how the heavier elements above iron form (see [Figure 2.1.2](#) for the periodic table), since the formation of heavier elements through fusion is not energetically possible in the stellar interior?

## 2.1 Nucleosynthesis of elements with $A > 56$

[Burbidge et al. \(1957\)](#) introduced the concept of synthesis of heavier elements through neutron-capture processes. There are two main nuclear physical reactions involved in the neutron-capture process,  $\beta$ -decay and the capture of neutrons by atomic nuclei. As a neutron interacts with an atomic nuclei, a heavier isotope is created, which might or might not be stable. If the resulting nucleus is stable, it can either stay in that state or continue to capture neutrons. However, whilst a stable nucleus exclusively will go through another neutron capture, an unstable nucleus has the possibility to undergo a  $\beta$ -decay as  $n \rightarrow p + e^{-} + \nu$ , which increases the proton number and a new element with  $Z+1$  is created. At this stage, the neutron capture can continue until another unstable isotope is reached and another heavier element is created by the subsequent  $\beta$ -decay.

The neutron-capture process can be divided into two sub-processes separated by the different time scales of  $\beta^-$ -decay and that of the neutron capture. These are the so-called slow- and rapid- process (s- and r-process), where for the s-process the time scale for  $\beta^-$ -decay is shorter than the (slower) timescale for neutron capture, whilst for the r-process the rapid flow of neutrons increases the mass number and isotopic number faster than the  $\beta^-$ -decay. These two processes represent different formation channels, or paths, creating isotopes of heavier elements (see Figure 2.1.1).

In comparison to the  $\beta^-$ -decay, the time scale for neutron capture is not constant, but depends on the neutron density and also the absorption cross section of the isotope. Therefore the environment where these processes takes places differs quite a bit; the s-process requires a neutron density of  $\leq 10^{11} \text{ cm}^{-3}$  (Busso et al. 1999) and the r-process somewhere between  $10^{24} - 10^{28} \text{ cm}^{-3}$  (Kratz et al. 2007). These neutron densities allow constraints to be placed on the environments where these processes take place. The neutron densities for the s- and r-process differ by several orders of magnitude. To fill this gap, an additional neutron-capture process called the intermediate-process (i-process) has been proposed to have a neutron density of  $10^7 - 10^{15} \text{ cm}^{-3}$  (Hampel et al. 2016). This is discussed further in Section 2.1.4.

Previous studies of the origin of elements has shown that the s-process dominates the formation of the lighter elements above mass number  $A \geq 60$  and the r-process the heaviest of the known elements. However, there is not a clean cut between the processes and the elements that are produced by these. Rather, one finds that the elements have a contribution from both processes where, in general, the contribution from the r-process increases towards higher mass numbers, with some exceptions for very stable elements (because of double magic nuclei, found at  $N = 50, 82$  and  $126$ ). This is since some isotopes are accessible through both s- and r-process paths, whilst some can only be reached through one of the processes; stable isotopes can work as a shield toward the s- or the r-process. For a graphic representation of this, see the colour coding in the periodic table, Figure 2.1.2.

### 2.1.1 s-process

The elements produced by the s-process can be divided into three different groups: the light, main and heavy s-process elements. These are defined from the stable nuclei of nucleon number  $N = 50, 82$  and  $126$ , resulting in build up, or peaks of stable isotopes of mass number  $A = 90, 138$  and  $208$ . These are so called magic numbers and are considered to be favourable to stable nuclei. The elements found at these peaks have isotopes with low neutron cross sections, which creates bottlenecks in the production of heavier elements, building an overabundance of these isotopes. The peaks are also often referred to as the first, second and third s-process peaks, and these are the labels used throughout this thesis.

The s-process path goes through more or less all the stable isotopes and ends at  $^{209}\text{Bi}$ . The explanation of this is not that there are no stable isotopes above the mass number 209 (expect  $^{238}\text{U}$  that indeed is effectively stable); the reason why the s-process does not produce heavier elements at this point is due to the low neutron-capture cross section of  $^{209}\text{Pb}$ , that instead decays to  $^{209}\text{Bi}$ , resulting in a blocked loop.

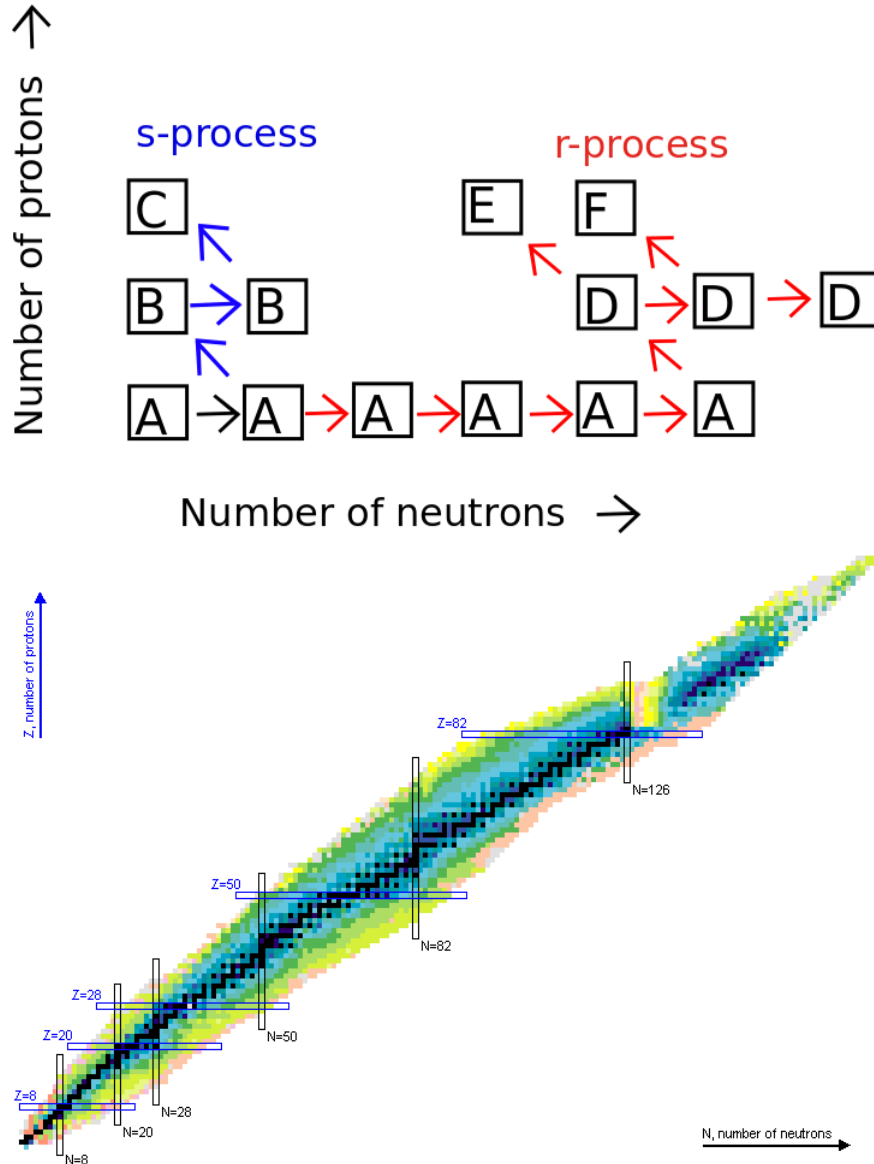


**Figure 2.1.1:** In both figures the y and x-axes increases with proton and neutron number, respectively. Top: Sketch of the s- and r-processes, marked in blue and red, respectively. The seed atom is denoted as A, to which a neutron is added. The resultant isotope can either decay by  $\beta^-$ -decay (blue, s-process), creating an higher Z element B, or continue to build up due to the high neutron flux, (red, r-process) and a subsequent decay, creating the heavier element D. Bottom: Map of isotopes. The black markers shows the valley of stability and the colour indicates the half-lives of the isotopes, going from blue to yellow. The magic numbers of  $N = 8, 20, 28, 50, 82$  and  $126$  are marked, which result in both s- and r-process peaks. Source: National Nuclear Data Center, Brookhaven National Laboratory, based on ENSDF and the Nuclear Wallet Cards, <https://www.nndc.bnl.gov/nudat2>.

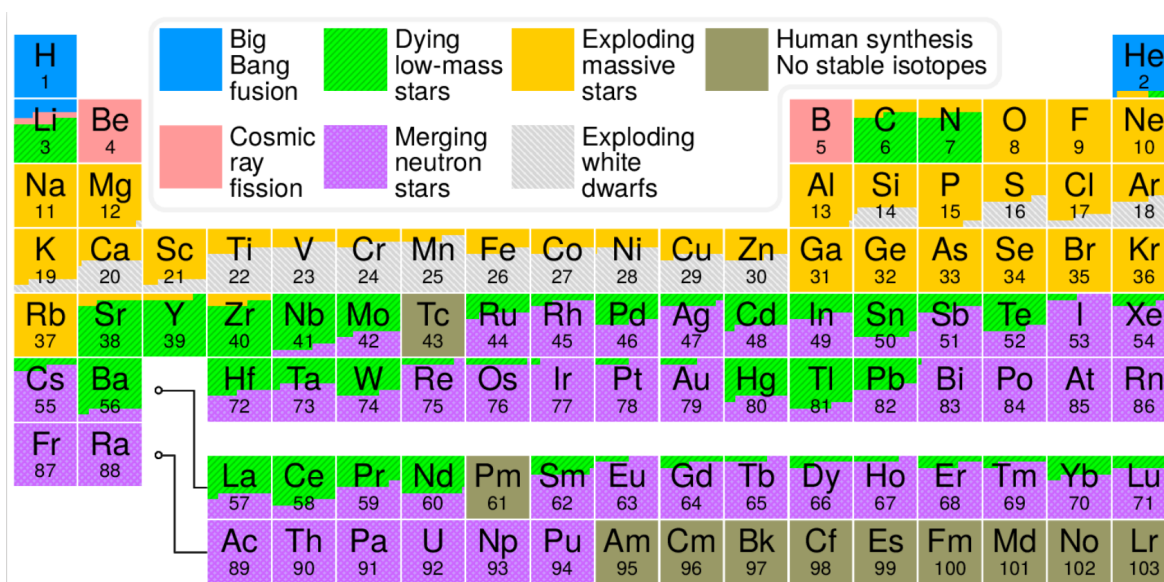


**Figure 2.1.2:** The periodic table with different formation channels indicated by color. The contribution is separated into percentages. The green boxes indicates contribution from dying low-mass stars, i.e the main s-process. The purple boxes, indicated as merging neutron stars, are contributions from the r-process. However, this field is currently studied intensively. For instance, the r-process production site is not constrained to only neutron star mergers. Additionally, fluorine (F) is produced by AGB stars rather than in exploding massive stars (Jönsson et al. 2015). Source: [https://sv.wikipedia.org/wiki/Fil:Nucleosynthesis\\_periodic\\_table.svg](https://sv.wikipedia.org/wiki/Fil:Nucleosynthesis_periodic_table.svg)

The s-process itself can be divided into three different formation channels, the *weak*, *main*<sup>1</sup>, and *strong* s-process. The processes differ somewhat from each other, but all occur in the later stages of the stellar life time. It should be noted however, that they are all due to the same physical process, the s-process, but with different neutron sources.

### Main s-process

The main s-process takes place in the later evolutionary stages of low- to intermediate- mass stars, somewhere between  $1.5 M_{\odot} \leq M \leq 8 M_{\odot}$ , known as low-mass and massive AGB stars (Busso et al. 1999; Herwig 2005). The interior structure of these stars are characterised by a carbon and oxygen core (depleted in hydrogen and helium), a helium shell outside of the core and another shell outside this consisting of hydrogen. These shells are separated by a thin zone, the helium intershell, enriched in both helium and carbon.

The principal neutron source in the main s-process comes from the following reaction<sup>2</sup>



where the source of the carbon comes from the carbon core through the CNO-cycle as



which, as mentioned previously, takes place in-between the burning shells due to hydrogen re-ignition. This causes the so-called  ${}^{13}\text{C}$  pocket to form, and allows very efficient s-process nucleosynthesis to occur. There is a secondary neutron source as well, see the reaction 2.3 below. However, the contribution from this is not as significant as the  ${}^{13}\text{C}$ -source in the low-mass AGB stars but instead in the massive AGB stars. During the AGB-phase of the star, the helium shell experiences instabilities, or thermal pulses (TPs). A TP releases energy which drives convective flow in the whole intershell for a short period of time. During one of these pulses, partial helium burning occurs, producing a large quantity of  ${}^{12}\text{C}$ . The thermal pulse causes mixing of the core and the envelope which transports the resulting products, mainly carbon isotopes and s-process elements, from the interior of the star to the envelope (Lambert 1991). AGB stars are partly known for their strong stellar winds, which is the source of the enrichment of main s-process elements in the interstellar medium (ISM).

### Weak s-process

The weak s-process is conceptually similar to that of the main s-process, but has another primary neutron source. This neutron source originates partly in the helium core burning phase and partly in the subsequent convective carbon burning shell phase, but in massive stars (Couch et al. 1974) instead of AGB stars (a small fraction in massive AGB stars). These stars

<sup>1</sup>Since this process carries the same name as the main/second s-process peak elements, I will only refer to them as second peak s-process elements/isotopes, to lessen the risk of confusion.

<sup>2</sup>For anyone unfamiliar with this notation, it means that the  ${}^{13}\text{C}$  absorbs an  $\alpha$ -particle and the result of the reaction is an  ${}^{16}\text{O}$  atom and a neutron.

reach higher temperatures than the low-mass AGB stars (initial mass of  $> 3 M_{\odot}$ , (Lambert 1991)), allowing the following reaction to take place:



The neutron source,  ${}^{22}\text{Ne}$  originates from pre-existing elements in the CNO-core coming from the gas from which the star was formed. The weak s-process is therefore dependent on the amount of pre-existing  ${}^{22}\text{Ne}$ , of secondary nature. Secondary nature means that the production depends on the pre-existing abundance of another element. It is worthwhile to once more point out that both neutron sources,  ${}^{13}\text{C}$  and  ${}^{22}\text{Ne}$ , take part in the main s-process, depending on the mass of the AGB-star where  ${}^{13}\text{C}$  stand for a majority of the neutron contribution, whereas  ${}^{22}\text{Ne}$  is the dominant neutron source for the weak s-process.

### Strong s-process

The strong s-component, introduced by Clayton & Rassbach (1967), is necessary to explain the third s-process peak, found at lead (Pb). The source of this process is shown to be in low metallicity, low-mass AGB stars (Travaglio et al. 2001). However, no elements from this peak will be analysed in this work.

### 2.1.2 p-process

The heavier AGB stars, namely those with  $M \geq 4 M_{\odot}$  have an episode of hot bottom burning in the early stages of the AGB-phase. When the bottom layer of the envelope is hot enough, the so called proton capture nucleosynthesis (p-process) can take place (Karakas & Lattanzio 2003), which takes place during the second dredge up (SDU). The dredge ups are caused by thermal instabilities in the stellar interior (see, for instance, the review by Lattanzio et al. (1996)). A small fraction of heavy isotopes is produced in the p-process (Burbidge et al. 1957) where these isotopes are distinguished by their high proton content, such as  ${}^{168}\text{Yb}$ ,  ${}^{184}\text{Os}$  and  ${}^{196}\text{Pb}$ . However, no elements produced in this process will be analysed in this work.

### 2.1.3 r-process

Just as the s-process, the r-process has peaks at the magic numbers. These peaks originate from  $\beta$ -decays close to the magic numbers; the  $\beta$ -decay half-life of the isotopes becomes so short that the r-process is halted, creating peaks in the r-process path. These peaks are found at mass number  $A = 80, 130$  and  $195$ . In contrast to the s-process, the r-process is not limited by heavy stable nuclei, but is instead restricted by the nature of the process itself; when the time scale of  $\beta$ -decay of the heavy nuclei becomes shorter than the neutron-capture probability, the r-process is halted. In turn, this means that in extremely neutron dense environments, very heavy isotopes can be created.

The formation sites for r-process elements is not yet fully established but the most likely sites are explosive environments, such as supernovae (SNe). The type of SN is not constrained yet and work has been done on several kinds, such as electron capture SNe (Wanajo et al. 2011),



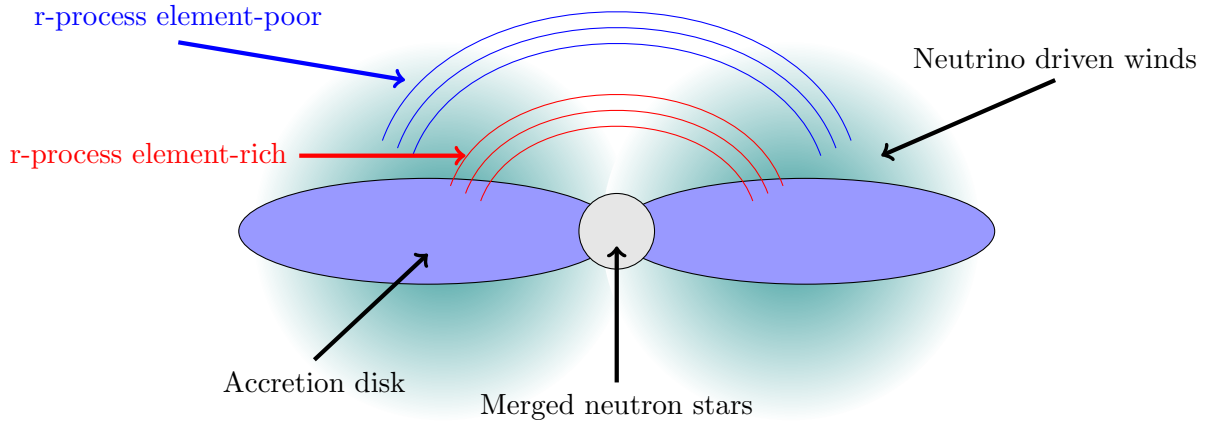


**Figure 2.1.3:** A schematic picture of the components in a kilonova, seen edge on; the innermost part consists of the merged neutron stars that eventually collapses to a black hole; circulating is an accretion disk, and neutrino-driven winds blow away ejecta.

magnetorotational driven SNe (Nishimura et al. 2015) and neutrino winds in core collapse supernovae (Wanajo et al. 2003; Wanajo 2013).

An additional proposed production site for r-process elements is kilonovae through the merger of neutron stars (Snedden et al. 2000; Thielemann et al. 2011; Wanajo 2018). The electromagnetic counterpart of the first ever neutron star merger known to be observed, GW170817 (Abbott et al. 2017), confirmed the production of r-process elements in these events. The mass of the ejecta from the kilonova is estimated to be  $0.03\text{--}0.06 M_{\odot}$  where  $0.01\text{--}0.02 M_{\odot}$  of this comprises elements of  $A < 140$ , found in the blue component of the emitted radiation. The later observed red component is dominated by elements with  $A > 140$  and makes up somewhere between  $0.02\text{--}0.05 M_{\odot}$  of the ejecta mass (see Drout et al. (2017)).

The production of r-process elements is believed to take place in the neutron-rich accretion disk and in the neutrino-driven winds. The closer to the merger, the more dense is the ejecta, favouring r-process element production; a schematic of this can be seen in Figure 2.1.3. However, a higher initial velocity of the neutrino wind can impede elemental production due to scattering of the production material (see for instance Wu et al. (2016); Lippuner et al. (2017)). In calculations, the quantity of r-process elements produced in the ejecta depends heavily on the equation of state adopted (Rosswog et al. 2013, 2014), making it hard to constrain stellar yields in models of kilonovae.

#### 2.1.4 Additional neutron-capture processes

The stellar yields from the s- and r-processes have been shown to be insufficient to produce all of the observed neutron-capture elements. The discrepancies become most apparent at lower metallicities. As a solution, additional neutron-capture processes have been introduced as a possible explanation, the most favoured ones being the Light Element Primary Process (LEPP) and the intermediate-process (i-process).

### Light Element Primary Process

Spectroscopic observations of metal-poor stars show a large enhancement in r-process elements, suggesting that around 10 % of solar Y and Zr is due to the r-process. However, combining the yields from the main s- and r-process is not sufficient to explain the solar observations of light neutron-capture elements. [Travaglio et al. \(2004\)](#) saw that up to 18 % of production contribution was missing in attempting to explain the abundances of Sr, Y and Zr. The residual fraction of solar Sr-Y-Zr is of a primary nature and thus, the Light Element Primary Process (LEPP) was introduced as an additional process to explain the yields for the first s-peak elements.

The production site for this is somewhat debated, however it is deemed most likely to take place in massive stars (and not strictly related to the classical r-process or to the weak s-process). In [Arcones & Montes \(2011\)](#) they find that proton- and neutron-rich winds from SNe can produce the Sr-Y-Zr peak sufficiently well to account for the lost residual fraction in [Travaglio et al. \(2004\)](#). However, in [Cristallo et al. \(2015\)](#) and [Trippella et al. \(2015\)](#) additional solutions are considered based on the s-process; they include stellar rotation and an increase in the size of the  $^{13}\text{C}$ -pocket, respectively, and find that these modifications could explain parts of the missing Sr-Y-Zr peak.

Furthermore, measurements of ultra-faint galaxies suggest that the contribution of s-process by rotating massive stars is important to explain the observed abundances ([Frischknecht et al. 2012, 2016](#); [Cescutti et al. 2013, 2015](#)). More about LEPP can be found in [Travaglio et al. \(2004\)](#); [Montes et al. \(2007\)](#); [Käppeler et al. \(2011\)](#).

### i-process

Halo stars carry the imprint of the early Galaxy, and can be used to probe these times (as dwarf spheroidal galaxies and UFDG). Carbon-enhanced metal-poor (CEMP) stars in the Galactic halo show enrichment in both s- and r-process elements. This is somewhat puzzling since the processes require neutron densities that differ by more than ten orders of magnitude and occur in different environments. Therefore, an intermediate neutron-capture process (the i-process), characterised by neutron densities between those of the s- and r-processes has been introduced to explain the measured abundances in CEMP-stars ([Cowan & Rose 1977](#); [Hempel et al. 2016](#)). The production site for this is still under investigation, where rapid-accreting white dwarfs (WD) are the most favoured suggestion. The process would be very similar to that of the s-process in AGB stars, but in the equivalent helium-burning shell of WDs instead ([Côté et al. 2018a](#); [Denissenkov et al. 2018](#)).

#### 2.1.5 Elements in this work

For dwarf stars, spectral lines for neutron-capture elements that are customary to use and usually produce good results (in the optical), are well known. This is not the case for giant stars, and therefore I have investigated all possible spectral lines for the neutron-capture elements that can be observed in the optical wavelength regime. The elements investigated are **copper (Cu)**, zinc (Zn), strontium (Sr), **yttrium (Y)**, **zirconium (Zr)**, niobium

**Table 2.1:** Contribution by main s-process production of low-mass AGB stars at the formation of the Solar System. The r-process is given as a residual of  $N_r = N_s - N_\odot$ . Data from [Bisterzo et al. \(2014\)](#). Note that copper (Cu) is not included in the table since it is mainly produced by the weak s-process in massive stars.

<b>Element</b>	<b>s-process</b>	<b>r-process</b>
Y	71.9	28.1
Zr	66.3	33.7
La	75.5	24.5
Ce	83.5	16.5
Pr	49.9	50.1
Nd	57.5	42.5
Eu	6.0	94.0
Gd	15.4	84.6

(Nb), molybdenum (Mo), ruthenium (Ru), barium (Ba), **lanthanum (La)**, **cerium (Ce)**, **praseodymium (Pr)**, **neodymium (Nd)**, samarium (Sm), **europium (Eu)**, **gadolinium (Gd)**, and dysprosium (Dy). The 9 elements with abundances of sufficient quality are marked with **bold** text, and are presented in this study. For the other 8 investigated elements the analysis was not of sufficient quality for one reason or another. This is described further in Section 5.6.

The 9 investigated elements range from the weak s-process- to the main s-process- and r-process-dominated elements, giving a broad picture of neutron-capture elements produced from different processes. Having this variety, one can more easily compare and infer how much the different processes takes part in forming that specific element. The contribution of the s- and r-processes to the elements studied, determined theoretically in [Bisterzo et al. \(2014\)](#), can be seen in Table 2.1. The r-process becomes the dominating process for heavier elements, in general, where europium (Eu) is classified as a 'pure' r-process element. Below, the elements analysed in this work are presented one by one.

### Weak s-process: Copper

Copper (Cu) is one of the first neutron-capture elements in the periodic table. The large-scale trend of copper abundance with metallicity was firstly measured by [Snedden et al. \(1991\)](#) where they discuss whether the dominating production channel for copper might be the weak s-process. As noted previously, the weak s-process is of a secondary nature due to the metallicity dependency; the neutron source originates from pre-existing  $^{22}\text{Ne}$  in the stellar interior (see eg. 2.3). In [Romano & Matteucci \(2007\)](#) they compare observations with theoretical yields and conclude that Cu is mostly produced by the weak s-process, although with a non-negligible production possibly by explosive SNe II at low metallicities. Additionally, they report that Cu has a rather negligible contribution of less than 5 % from the main s-process.

### First s-process peak: Yttrium, Zirconium

Yttrium (Y) is the first element in our selection from the first s-process peak. It has been debated whether the peak at Sr-Y-Zr is produced by the weak or the main s-process; [Käppeler et al. \(2011\)](#) conclude that a small fraction of Sr is produced by the weak s-process. In [Travaglio et al. \(2004\)](#) LEPP is introduced as an explanation for the production of the peak, and the work by both [Käppeler et al. \(2011\)](#) and [Bisterzo et al. \(2014\)](#) have similar findings to [Travaglio et al. \(2004\)](#), pointing towards an additional neutron-capture process. In several studies (e.g. [Burris et al. \(2000\)](#) on metal poor giants and [Battistini & Bensby \(2016\)](#) on dwarfs) the measurements of Sr are heavily scattered, making analysis more difficult. However, previous work on yttrium (Y) ([Bensby et al. 2014](#); [Delgado Mena et al. 2017](#)) and zirconium (Zr) ([Delgado Mena et al. 2017](#); [Battistini & Bensby 2016](#)), show rather similar trends to that of main s-process elements at solar metallicities, whereas at lower metallicities the results point to an additional production channel to that of the s- and r-process, possibly LEPP.

### Second peak s-process: Lanthanum, Cerium, Praseodymium, Neodymium

Lanthanum (La), cerium (Ce), praseodymium (Pr) and neodymium (Nd) are part of the second peak of the magic neutron number 82. In both [Battistini & Bensby \(2016\)](#) and [Delgado Mena et al. \(2017\)](#), neither La nor Ce shows any significant trend with metallicity, although a signature of the onset of AGB stars, indicating production from the main s-process, can be seen in the trends as a 'bump'. Abundance estimations of Pr have not been done previous to my work<sup>3</sup>. Nd is presented in [Bland-Hawthorn & Gerhard \(2016\)](#) as having a 50/50 production from s- and r- process, respectively. This is confirmed in results from e.g. [Bisterzo et al. \(2016\)](#) and [Battistini & Bensby \(2016\)](#), where the trend with metallicity is similar to both that of pure s-process elements such as Ba and the pure r-process element Eu.

### r-process: Europium, Gadolinium

Europium (Eu), with a 94.0 % production from the r-process ([Bisterzo et al. 2014](#)), is considered to be a pure r-process element and is therefore often used as a reference in evaluating the relative contribution of the r-process in nucleosynthesis analysis work. Gadolinium (Gd) is, like Pr, an observationally poorly-studied element; recently the first study for a large stellar sample was published by [Guiglion et al. \(2018\)](#), showing that Gd is very similar to Eu, but might have a somewhat different production channel at high metallicities. The r-process elements show declining  $[X/Fe]$  ratios with increasing metallicity, similar to that of  $\alpha$ -elements (the larger the r-process contribution, the steeper the slope). This suggests that the r-process is associated with short-time scale progenitors ([Guiglion et al. 2018](#)).

<sup>3</sup>Only small scale investigations on peculiar stars have been done up til now (see [Ryabchikova et al. \(2001\)](#); [Dolk et al. \(2002\)](#))

## 2.2 Using giant stars

Stars with spectral type of either F, G or K have been favoured within abundance determination studies and for galactic archaeology; these stars preserve their initial chemical composition. Several of the previously mentioned studies, such as [Mishenina et al. \(2013\)](#); [Bensby et al. \(2014\)](#); [Battistini & Bensby \(2016\)](#); [Delgado Mena et al. \(2017\)](#) have conducted spectroscopic surveys of dwarf stars. In this work I instead consider giant stars which have the advantage of being brighter, thus enabling higher S/N measurements at further distances. The method I follow is the one described, and used, in [Jönsson et al. \(2017a,b\)](#) and [Lomaeva et al. \(2019\)](#) where a subset of the analysed spectra have been used for abundance determination of  $\alpha$  and iron peak elements. With these more luminous stars, high resolution spectroscopic measurements can not only be obtained at larger distances, but require less observational time at similar distances to that of a given dwarf star. [Jönsson et al. \(2017a\)](#) and [Lomaeva et al. \(2019\)](#) also include bulge stars in the analysis, showing that abundances of giants in the bulge can be obtained using the method developed. Bulge stars are not included in this work, which instead focuses on obtaining a large sample of local disk stars to act as a reference for other surveys and lays the foundation for future work.

Besides Galactic archaeology in the disks and bulge/bar, other fields benefit from more refined abundance determination. For instance, surveys measuring clusters and their stars, halo stars, ultra-faint galaxies, dwarf spheroidal galaxies, and Andromeda (the closest large galaxy to the Milky Way galaxy, also known as M31). Ultra-faint galaxies often have very few, of the order of ten, observable (giant) stars. These galaxies are, as the name indicates, extremely faint and low mass. Often they have only had a short burst of star formation early on in their history, making them ideal laboratories for studies of low metallicity environments and neutron-capture elements in their cradle. The careful trends presented for giant stars in this thesis are needed as a reference for such investigations.

With this in mind, it becomes clear that using giant stars is favourable when working with Galactic archaeology in order to include more Galactic components in the analysis. However, spectroscopic analysis of giant stars is not without difficulty, for reasons listed and explained below:

- Stars cool down as they expand<sup>4</sup> and enter the red giant branch. The lower effective temperatures of giant stars impede the break up of molecules in the stellar atmosphere, enabling for molecular absorption lines to be seen in the spectra. These lines might cause blending with the lines of interest, which, if not modelled properly, affect the determination of the abundances.

Additionally, blending of molecular lines close by or in the wings of the atomic lines of interest, obstruct the placement of the continuum which makes the determination of the line strength, and in turn the abundance, extremely hard. Since abundances are obtained by measuring the contrast of the line and continuum opacities, a falsely identified continuum will lead to badly determined abundances, even for high quality data.

---

<sup>4</sup>As mentioned previously, the expansion happens at the point where hydrogen burning has depleted the (hydrogen) core by fusion to helium, increasing the molecular weight of the core.

- Due to the lower surface gravities, typical for giant stars, the continuum opacity will be lower, caused by the lower electron pressure. As a result of this, the line strength increases. This might cause the line to become saturated; for abundance determination it is favourable to use weak lines that follow the linear part of the curve of growth. As seen in Figure 2.2.1, saturated lines are less sensitive to the abundance and should not be used in abundance analysis. On the other hand, it should be noted that the low surface gravity of giant stars helps to strengthen otherwise too weak lines in dwarfs. An example of this is the important forbidden [O I] lines, which are more favourably measured in giants for this reason. For a review of this subject see Ch 13 in Gray (2005).
- Most of the spectral lines in the optical region arise due to absorption of the photons by neutral element species. At the lower effective temperatures of red giants, the amount of neutral species increases (in comparison to ionised species), and consequently the strength of the spectral lines increases too.

Considering these challenges, giant stars require a careful analysis to get proper abundances. Therefore, it is of great importance to find lines that

- have good atomic data,
- are unblended or only blended with few lines having well-defined atomic data,
- are of suitable strength.

How the selection is done is described in more detail in Chapter 4.

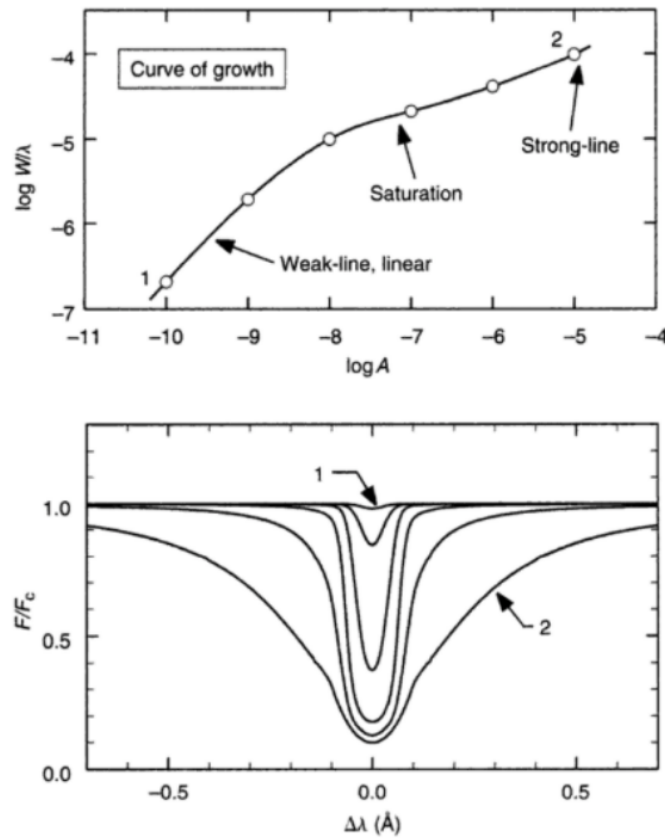


**Figure 2.2.1:** Theoretical behaviour of line profile and equivalent width (the concept of equivalent width is described briefly in Section 4.1) of a spectral line, showing the sensitivity of a line to the abundances for different levels of saturation. Top: The equivalent width  $W$  plotted against the abundance  $A$ . For weak lines the equivalent width is proportional to the abundance, where saturated lines are less sensitive to the abundance. Bottom: The profile of the line, the curves correspond to the dots in the curve of growth to the left. The pictures are from the book by [Gray \(2005\)](#).

## Chapter 3

# Stellar sample

In this chapter a description of the properties of the stellar sample and the instrumentation with which their spectra are collected is provided. The stars are bright and a majority of them are located in the so-called solar neighbourhood, often defined as stars within 1 kpc of the Sun. The spectra are collected with the high-resolution FIBre-fed Echelle Spectrograph (FIES) (Telting et al. 2014) mounted on the Nordic Optical Telescope (NOT) at Observatorio del Roque de los Muchachos, La Palma. Using the same instrument for the whole stellar sample gives the advantage of all spectra having the same resolution and instrument profile, which reduces possible systematic uncertainties in the analysis.

The spectra were collected during four visits to the NOT in May 2015; June 2016; March 2018 and October 2018, where I participated in the last two, doing both preparations and performing the observations (see Figure 3.0.1). The high resolution fibre on FIES provides a resolution of  $R \sim 67000$ . A short summary of the observational visits can be seen in Table 3.1 and properties of the data can be found in Table 3.2. The remaining 186 spectra are from the FIES-archive.



(a) The outside of the NOT dome at sunset.

(b) The NOT with open dome hatch.

**Figure 3.0.1:** Photographs from my first observational visit to the Nordic Optical Telescope (NOT) at Observatorio del Roque de los Muchachos, La Palma, in March 2018.



**Table 3.1:** Information about the observing visits. The number of nights and stars (spectra) is indicated as well as the instrument and conditions at the site. The difference between the old and new FIES is that a new CCD was installed in the autumn of 2016, providing more wavelength coverage. Additionally, FIES was equipped with new fibre bundles in July 2017 that improves the radial velocity stability.

When	Nights	Mode	Instrument	Conditions	Stars
May 2015	5	Service	Old FIES	-	168
June 2016	4	Visitor	Old FIES	Technical problem one night	70
March 2018	6	Visitor	New FIES	Generally bad weather	70
October 2018	6	Visitor	New FIES	Generally bad weather	29

**Table 3.2:** Properties of the data collected and used in this work.

Number of stars	523
Spectrometer	FIES
Telescope	Nordic Optical Telescope (NOT)
Wavelength region [Å]	4100 - 7360 (old), 7600 (new)
Resolution	67000
S/N (min/median/max)	31/102/319
Distance (min/median/max) [pc]	30/217/3295
V-magnitudes (min/median/max)	-0.05/6.95/13.11
Exposure times (min/median/max) [s]	3/413/7200

The magnitudes of the stars in the V-band range from -0.05 to 13.11. The resulting S/N for the stellar spectra are in general high with a mean of 109. The S/N is calculated using the method from [Stoehr et al. \(2008\)](#) where the wavelength region between 6000-6200 Å is used for the determination. This region is chosen since it contains mostly spectral lines of normal strengths and no telluric lines. Additionally, there is a clear continuum in this region, which is needed for the algorithm provided by [Stoehr et al. \(2008\)](#).

The exposure times to get these S/N ratios ranged between only 3 seconds for the brightest stars up to 30 minutes for stars of  $\sim 8-9$  in magnitude (this is the maximum recommended exposure time for FIES). The fainter stars have multiple exposures, adding up to 2 hours (7200 seconds). The mean exposure is 15 minutes.

The spectra were reduced using the FIEStool pipeline. Telluric lines have not been removed from the spectra, instead, a telluric spectrum from the Arcturus atlas ([Hinkle et al. 2000](#)) has been plotted over the appropriately-shifted observed spectra and affected regions have been avoided on a star-by-star basis. Moreover, as described in Chapter 4, I carefully checked lines for the abundance analysis, avoiding lines that suffer from blends with other lines which have atomic data of insufficient quality.

A subset of the stellar sample of 291 stars has been analysed spectroscopically in previous work by [Jönsson et al. \(2017a,b\)](#) and [Lomaeva et al. \(2019\)](#) where they determine the stellar parameters and chemical abundances of the  $\alpha$  and iron-peak elements, respectively. They use the same method as in this work to determine the chemical abundances which resulted in high quality abundances.

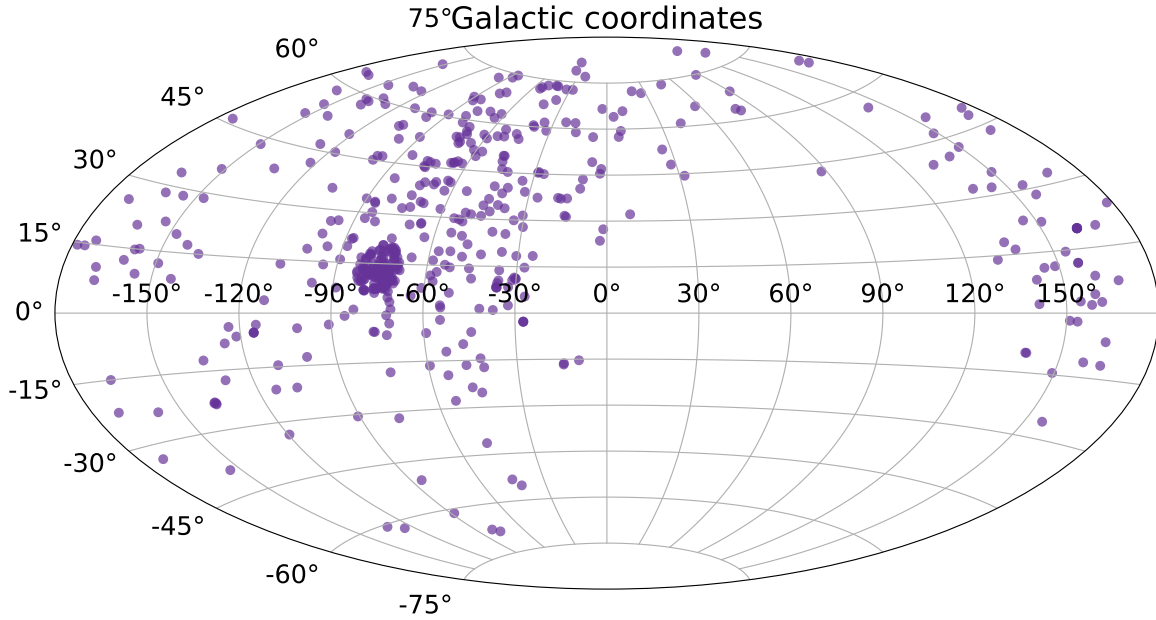


**Figure 3.0.2:** Positions of the stars in the stellar sample using galactic coordinates  $(l, b)$ , derived from Gaia DR2 (Gaia Collaboration et al. 2018) right ascension and declination coordinates.

Using the Gaia catalogue from the second data release, Gaia Collaboration et al. (2018), I took a closer look at the position and distances of the stars in the stellar sample<sup>1</sup>. For this, the Python package `astropy` (Astropy Collaboration et al. 2013) is used to transform between different units and coordinate systems. As seen in Figure 3.0.2, due to the position of NOT, the stellar sample consists of stars mainly from the northern hemisphere. The dense part is the Kepler field, specifically targeted for validation purposes. The positions of the stars in galactic coordinates  $(x, y, z)$  are considered as well, in order to see how the stellar sample is distributed, see Figure 3.0.3.

Additionally, the distances and radial velocities (RV) of the stellar sample can be seen in Figure 3.0.4. A majority of the stars is found within 1 kpc, independent of whether the distance measurements from either Gaia DR2 (Bailer-Jones et al. 2018) or McMillan (2018) are used.

<sup>1</sup>It should be noted that only 493 out of the 523 stars could be found in the Gaia catalogue, primarily due to the lower magnitude limit of Gaia where some of the giant stars in this work are too bright for that limit: the Gaia magnitude is limited to a dim limit of  $G = 21$  and a bright limit of  $G \approx 3$ , where the Gaia G band has a mean wavelength of 673 nm (Jordi et al. 2010)

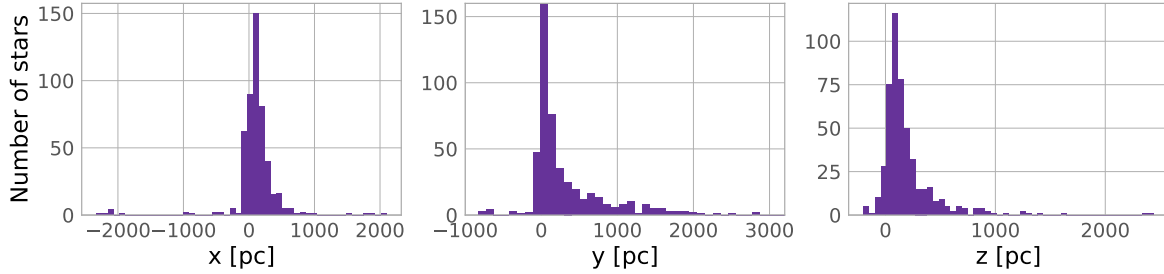


**Figure 3.0.3:** Positions of the stars in  $(x,y,z)$ -coordinates. Left: the x-position is normalised to the Sun, at a position of 8 kpc [Malkin \(2012\)](#),  $x > 0$  is in the direction toward the galactic center. Middle: the y-position, the positive direction is *behind* the Sun. Right: the z-position, positive is *upwards* in the disk.

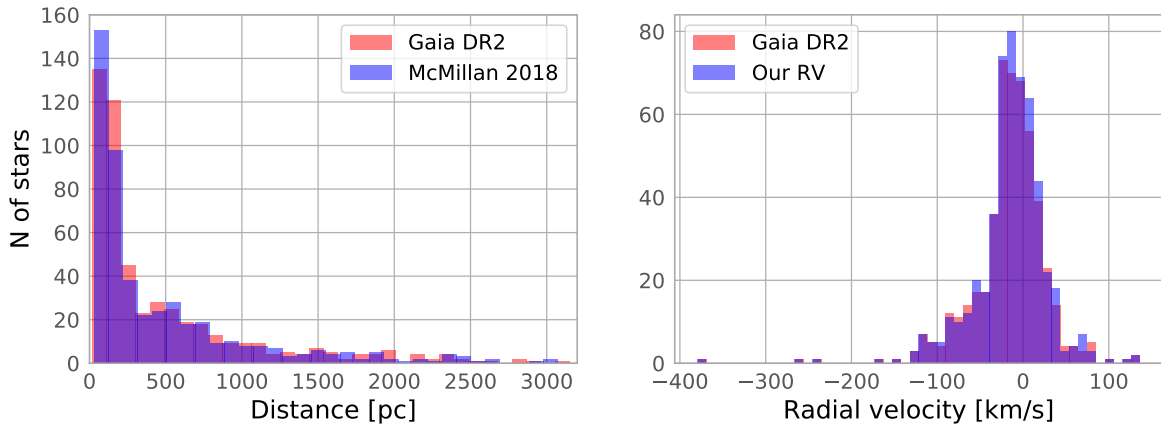


**Figure 3.0.4:** Left: Histogram of the distances of the stars in the stellar sample, comparing the distances from Gaia DR2, namely the distances from [Bailer-Jones et al. \(2018\)](#), to derived distances from [McMillan \(2018\)](#). Right: The radial velocities (RV) of the stars, comparing the RV derived from my FIES spectra and the ones given in Gaia DR2.

# Chapter 4

## Methodology

The abundances of stars are measured by considering the intensities of the spectral lines. The quality of the spectra is set by the signal-to-noise ratio (S/N) and the spectral resolution, which in turn is set from the resolution of the spectrograph. The resolving power  $R$  is defined as the smallest difference in wavelengths  $\Delta\lambda$  that can be distinguished at a given wavelength of  $\lambda$ ,

$$R = \frac{\lambda}{\Delta\lambda}. \quad (4.1)$$

Considering this, a higher resolution results in more resolved lines in the spectra, and in turn, in likely more precise and accurate values. In this work the spectra have high resolution ( $\sim 67000$ ), which is suitable for the goals of this work. However, a higher resolution requires more observing time than that for lower resolution, and in order to make use of the high resolution spectra, a high signal to noise (S/N) is also required.

Throughout this work the usual convention of identifying overall metallicity with the stellar iron-to-hydrogen ( $[\text{Fe}/\text{H}]$ ) is used. This follows the standard notation of comparing the number density  $N$  for a given element ( $X$  or  $Y$ ) of the star to that in the Sun, as

$$[X/Y] = \log_{10} \left( \frac{N_X}{N_Y} \right)_{\text{star}} - \log_{10} \left( \frac{N_X}{N_Y} \right)_{\odot}. \quad (4.2)$$

Additionally, all other elements are scaled to the measured Solar abundance of that specific element. In this work I use the measured solar abundances from [Grevesse et al. \(2015\)](#).

In this chapter the method used to determine the stellar abundance - synthetic spectra, and the tool, Spectroscopy Made Easy - is introduced. Together with this, the chapter also covers the assumptions made when modelling stellar spectra, how the stellar parameters and abundances are determined and how the selection of atomic lines is carried out. The separation of the disk population is described with an investigation of the kinematics of the stars in the stellar sample. Concluding for the methodology chapter, the systematic and random uncertainties are investigated.

## 4.1 Spectral line synthesis

In this work, abundances are determined by comparing synthetic spectra to the observed spectra. However, synthetic spectra are not the only way of determining abundances: it can also be done by measuring the equivalent width (EW)<sup>1</sup> of spectral lines. However, in this work, the EW-method is considered not to be the most suitable method. Firstly, due to the lower temperatures of the giant stars, their spectra are more likely to be contaminated by molecular lines, increasing the risk of blends with the atomic lines of interest. These blends have to be modelled, which is possible using synthesised spectra. Additionally, a majority of the elements in this work have odd atomic numbers (i.e. 29, 39, 57, 59, and 63 for Cu, Y, La, Pr, and Eu respectively), which means that they are susceptible to *hyperfine splitting* (hfs), described more in detail in Section 4.1.1, EW-measurements can not take hfs into account.

The synthetic spectra are produced using the tool *Spectroscopy Made Easy - SME* (Valenti & Piskunov 1996; Piskunov & Valenti 2017). To do this, SME needs certain input parameters, as described below:

- An observed stellar spectrum.
- A model atmosphere (how this is constructed is described in more detail in Section 4.1.2). SME uses a grid of MARCS model atmospheres (Gustafsson et al. 2008). These are spherically symmetric, 1D hydrostatic, LTE models. Using a spherically symmetric model is necessary when analysing giant stars, due to their large photospheres, and is thus suitable for this type of analysis (Heiter & Eriksson 2006).
- Stellar parameters, how these affect the model atmosphere and how these are determined for the stars in the stellar sample is described in Section 4.1.2 and Section 4.2, respectively. Additionally, not described in the above-mentioned sections, are the radial velocity ( $v_{\text{rad}}$ ) and the macro- and microturbulence ( $v_{\text{mac}}$  and  $v_{\text{mic}}$ ). Lastly there is the elemental abundance,  $[X/\text{Fe}]$ , which is the only parameter that is not fixed during the analysis in this work.
- Atomic and molecular line data. A more detailed description of these is given in Section 4.3.1. These are the element name, the transition wavelength, ionisation state, lower state excitation energy, oscillator strength ( $\log gf$ ) and damping parameters (radiative, Stark, van der Waals). The data for the lines used in this work can be found in Appendix B.
- Intervals defining
  - A segment of the spectrum within which the spectral line of interest lies. In this work the segments are  $\sim 5\text{-}10 \text{ \AA}$  wide
  - A line mask defining the edges of the atomic spectral line. In this work these masks are  $\sim 0.1 \text{ \AA}$  wide

---

<sup>1</sup>The EW of a spectral line is obtained by measuring the area drawn by the line, when plotted as the intensity versus wavelength. The area is represented as a rectangle with a height equal to that of the normalised continuum emission, and finding the equivalent width such that the area of the rectangle is equal to the area of the spectral line.

- Masks defining continuum sections within the chosen segment.

These segments and masks are manually defined after visual inspection of the spectra to pick out usable atomic lines (i.e lines that are not too blended nor too weak/strong). At least three (3) continuum points, with at least one on each side of the spectral line of interest, have to be defined for (a chance of) a good spectral fit. This is done for all stars simultaneously, decreasing the workload and the time that would have been spent defining individual continuum masks for every star. The main difficulty with this is to find continuum points such that they fit in the spectra of both metal-poor/-rich stars and cool/slightly warmer stars, as described in Section 2.2. The placement of the continuum is an important source of uncertainty, and much careful effort has been put into this aspect of the analysis.

Using these given parameters, SME calculates abundances using the observed stellar spectrum to constrain the synthetic spectrum. The fit is done by a weighted  $\chi^2$ -minimisation (Valenti & Piskunov 1996). The synthesised spectra and the observed spectra for Arcturus<sup>2</sup>, for all lines and elements used in this work, can be seen in Appendix A.

#### 4.1.1 Isotope shift and hyperfine splitting

Shifting and splitting of the energy levels can, if not handled and modelled properly, cause erroneous abundances. Where the splitting is very small it can be neglected. *Small* is a relative quantity that depends on the resolution of the spectra; the higher the resolution, the more features will be resolved and have to be considered. Given the high resolution of the spectra in this work both hyperfine and isotopic splitting is considered as described below.

##### Isotope shift

Isotope shifts are the result of different neutron number in the nuclei of the element introducing a change in both mass and volume. Due to this, the atomic energy levels will shift slightly. The explanation for the shift is that the electrons becomes less tightly bound to the nucleus since it experiences a smaller charge per volume. This introduces a broadening of the atomic spectral line, which might have to be considered if the star has more than one isotope present in its atmosphere. For lighter elements, the shift is dominated by the shift in mass by additional neutrons, whilst the mass difference becomes relatively smaller for more massive nuclei. Therefore, the isotope shift of heavier elements (the ones considered in this work) is dominated by the volume/size change of the nucleus caused by different neutron numbers.

For some elements the abundance can be dominated by one of the isotopes, whilst the remaining isotopes can often be ignored in the analysis, since their contribution to the spectral line is negligible. However, as seen in Table 4.1, some of the elements analysed in this work have a non-negligible contribution of several isotopes that has to be taken into account when doing

<sup>2</sup>Arcturus is a typical giant star, described more in the Uncertainties Section 4.5

the analysis. Unfortunately, SME does not include a way to model different isotopes. Therefore the energy shifts of these elements have been added manually by scaling the  $\log gf$ -value of the elements, using the proportion of each isotope in question. This is done as

$$\begin{aligned}\log_{10}(gf) &= x \\ f &= \frac{10^x}{g} \\ f_{\text{scaled}} &= F \frac{10^x}{g} \\ \log_{10}(gf_{\text{scaled}}) &= \log(F \cdot 10^x) = x + \log_{10}(F)\end{aligned}\tag{4.3}$$

where  $F$  is the percentage contribution of a specific isotope. I used the solar isotopic ratios listed in column 3 of Table 4.1.

**Table 4.1:** Isotope information of the elements included in this work. Column 2 gives the baryonic number of the stable isotopes that contribute to at least 1 % to the Solar System abundance, which is the ones included in this work. Column 3 gives the corresponding relative isotopic abundances to the stable isotopes, with references in the last fourth column.

Element(Z)	Baryon number	Rel. abundance ( $F$ )	Reference
Cu(29)	63:65	69:31	<a href="#">Shields et al. (1965)</a>
Y(39)	89	100	<a href="#">Collins et al. (1957)</a>
Zr(40)	90:91:92:94:96	51:11:17:17:3	<a href="#">Nomura et al. (1983)</a>
La(57)	139	100	<a href="#">de Laeter &amp; Bukilic (2005)</a>
Ce(58)	140:142	88:11	<a href="#">Chang et al. (1995)</a>
Pr(59)	141	100	<a href="#">Collins et al. (1957)</a>
Nd(60)	142:143:144:145:146:148:150	27:12:24:8:17:6:6	<a href="#">Zhao et al. (2005)</a>
Eu(63)	151:153	48:52	<a href="#">Chang et al. (1994)</a>
Gd(64)	154:155:156:157:158:160	2:15:20:16:25:22	<a href="#">Eugster et al. (1970)</a>

## Hyperfine splitting

Hyperfine splitting (hfs) occurs for elements with odd atomic numbers, which in this work is Cu, Y, La, Pr, Eu. In Table 4.2, the spectral lines where hyperfine splitting is included in the line list can be seen. It is a feature arising from the odd (and hence unpaired) number of nucleons in the nucleus, resulting in nucleon-electron spin interactions. These interactions will split the atomic energy levels into multiple levels, creating several lines in the spectrum, increasing the line width.

From Table B.1, the width of the lines due to hfs can be calculated simply by calculating the separation between the first and last hyperfine component. Using the relation between the resolution and the wavelength, eq. (4.1), it is possible to calculate the details that can be resolved in the spectra, allowing the sizes of these to be compared, as shown in Table 4.2. As can be seen, several of the lines have hfs larger than, or comparable to, that of the calculated resolution, justifying the decision to include hfs in this work.

**Table 4.2:** The lines with included hfs in the data. Column 2 gives the wavelength without hfs. Column 3 gives the actual hfs in the data and column 4 the theoretically calculated resolution in the spectra. Note that 1) there is no available data for hfs for Y and that 2) there is only data available for two out of the four spectral lines used for abundance determination of La.

Element	Line [ $\text{\AA}$ ]	$\Delta\text{hfs}$ [ $\text{\AA}$ ]	$\Delta\lambda$ [ $\text{\AA}$ ]
Cu	5782.108	0.139	0.086
La	5303.530	0.032	0.079
La	6390.479	0.044	0.095
Pr	5219.035	0.122	0.078
Pr	5259.677	0.124	0.079
Pr	5322.741	0.137	0.079
Eu	6645.103	0.092	0.099

The result of ignoring hfs for spectral analysis, due to the increased width of the spectral line, can be an overestimation of the measured abundance (Prochaska & McWilliam 2000). See also Thorsbro et al. (2018) on the importance of hfs for the determination of abundances using strong lines.

### 4.1.2 Model assumptions

To synthesise a stellar spectrum, one needs to make certain assumptions. In this section I will briefly go through these and the method to determine the chemical abundances.

Firstly one needs to model the environment where the spectrum is created. The absorption lines originate in the outer part of the photosphere at different depths, depending on the optical depth. Consequently, it is essential to have a clear understanding of the physics of the gas/plasma in the photosphere where the lines are created. The model atmosphere describes the temperature and pressure distributions in the star, as a function of optical depth. The model atmosphere is generated from the stellar parameters, which are:

- Effective temperature  $T_{\text{eff}}$ , linked to the luminosity of the star.
- Surface gravity  $\log g$ , which determines the gas pressure in the atmosphere.
- Metallicity as traced by the iron over hydrogen abundance  $[\text{Fe}/\text{H}]$  (see eq. 4.2), associated with the elemental mixture and in turn the location of the peak for emitted radiation<sup>3</sup>,
- Microturbulence  $v_{\text{mic}}$ , the small scale motions in the stellar atmosphere, where the extent of the turbulence is smaller than the mean free path of the photons. In practice, it is a line-fitting parameter (Rutten 2003), although it should be noted that it is an important parameter for the overall physical shape of the photosphere.

As for a lot of modelling, modelling stellar atmospheres is simplified using several assumptions. This reduces the computational time and decreases the risk for redundant complexity. Below,

<sup>3</sup>For example, metals are efficient at absorbing UV-light, making metal-rich stars appear redder.



the four most frequently used assumptions in modelling atmospheres are described,

- **Hydrostatic equilibrium:** This assumption prescribes that the motions of the gas in the stellar atmosphere stay constant over time, which is rather well fulfilled. Additionally, the assumption prevents the star from collapsing on itself: the outward pressure gradient is cancelled by the inward gravitational force. Within this assumption, there is negligible mass loss from the star.
- **Local Thermodynamic Equilibrium - LTE:** Local Thermodynamic Equilibrium, often abbreviated to LTE, assumes thermodynamic equilibrium at a local temperature in the stellar atmosphere. As a result, one can apply the following general physics principles, facilitating the modelling:
  - **The Maxwellian distribution** describes the velocity of electrons and ions.
  - **The Boltzmann distribution** describes the excitation equilibrium.
  - **The Saha equation** describes the ionisation equilibrium. The Saha equation relates the ionisation state of a gas in thermal equilibrium to the temperature and pressure.
  - **Collisional versus radiative processes:** Collision is assumed to dominate, implying that an excited state has a larger probability of collisional de-excitation than radiative de-excitation.

These constraints allow the Planck function to be used to describe the ratio between the emission and absorption, or, the source function; the source function is purely dependent on the temperature, locally.

- **Homogeneous or non-homogeneous atmosphere:** In this work the one dimensional homogeneous case is used to describe the atmosphere.
- **Plane parallel or spherical geometry:** For giant stars the assumption of spherical symmetry is necessary. For dwarfs, one instead assumes the more simplified one-dimensional atmosphere as *plane parallel*.

### Consequences of the assumptions

Since there are many assumptions made in modelling stellar atmospheres, there are naturally exceptions to these. Firstly, the one dimensional atmosphere does not include convection, as a non-homogeneous, 3D model does. In turn, 1D models have to parameterise small scale motions using the microturbulence, which is not necessary in the 3D case. However, models of 3D stellar atmospheres are still being developed due to their complexity and are to a large extent not available yet. Additionally, the computational time is a very significant limitation to overcome using 3D models.

Secondly, the assumption of LTE does not always hold for some spectral lines. In general, the line strength can differ from LTE due to changes in the line source function, linked to the line opacity which affects the line formation depth. Often the lines that are not formed in LTE conditions, only affect the line formation of that specific line and not the model atmospheric

structure as such. Thus, the model atmospheres can be safely calculated in LTE. However, when synthesising spectral lines, caution should be taken.

In the outermost atmospheric layer of stars, the gas density is significantly lower than in the interior, causing radiative processes to be comparable to, or even dominant, over collisional processes. This results in deviations from the LTE assumption and the concept of non-LTE (NLTE) becomes more applicable. In NLTE one assumes that the velocity of the particles follows the Maxwellian distribution, but the radiative transfer equation is solved properly using the exact source function instead of assuming that it can be described by the Planck function.

Thus, the atomic level populations have to be calculated using the equations of statistical equilibrium which account for the influence of the radiation and collisions on the level populations. Naturally, these calculations are computationally more challenging than the LTE calculations, and require detailed atomic data of the atomic levels, which mostly do not exist for heavier elements. It should be noted that NLTE calculations with less precise atomic data can often be misleading (Asplund 2005). Because of this, the LTE assumption is still widely used in stellar spectroscopy. However, the effects of deviations from the LTE assumption should be checked if possible.

Additionally, giant stars have lower mass densities than that of dwarf stars and consequently lower collision rates in the atmospheres. However, giant stars have lower temperatures which decrease the radiation field<sup>4</sup>. Due to this the question about NLTE effects in giants is non-trivial.

For the elements used in this work, NLTE investigations are not available for giant stars, although some information about this can be found in the literature

- Shi et al. (2014) found that for the solar Cu-lines, the departures from LTE are small where the mean NLTE abundance correction is roughly  $\sim 0.01$  dex. However, in the very recent work by Xu et al. (2019) they analyse 129 giant stars in the bulge and find that the NLTE effects for Cu show a clear dependence on metallicity, with gradually increase of abundances with decreasing metallicity. They report that their results indicate that the NLTE effects of Cu are important both for metal-poor and for supersolar stars and conclude that LTE results underestimate Cu abundances.
- Velichko et al. (2010) found that NLTE effects of Zr depend weakly on temperature where they calculated corrections for Zr I lines (only Zr I has been analysed in this work) to reach 0.33 dex for solar-type models.
- In Mashonkina & Gehren (2000) an analysis of cool dwarf stars has been done, where they found a small NLTE correction of +0.03 dex for Eu.

---

<sup>4</sup>It has been shown that higher temperatures increase the radiation field meaning that it can dominate over collisional processes in the de-excitation of atoms (Lind et al. 2012).

## 4.2 Stellar parameters

To construct the atmospheric model for a star, one needs to determine the global stellar parameters that define the star. There are several ways to extract these from both photometric measurements and spectra. In this work the stellar parameters are determined by having them as free parameters in SME together with the abundances of elements that are large electron donors (Mg, Si). This means that  $T_{\text{eff}}$ ,  $\log g$ ,  $[\text{Fe}/\text{H}]$ ,  $v_{\text{mic}}$ ,  $v_{\text{mac}}$ ,  $[\text{Mg}/\text{Fe}]$ ,  $[\text{Si}/\text{Fe}]$ , and  $[\text{Ti}/\text{Fe}]$  were free parameters with line masks covering Fe I, Fe II, Ti I, Ti II, Mg I, and Si I lines. All flux information in the line masks was then used to constrain the stellar parameters by SME using  $\chi^2$  minimisation. However, some spectral lines are more sensitive to certain stellar parameters than others, and in practice, this means that some lines/combination of lines are driving the determination of a certain parameter. This is described in the points below:

- $T_{\text{eff}}$ : The temperature is determined by abundance measurements of 14 Fe I lines, where the different lines ought to give the same abundance. NLTE corrections from [Lind et al. \(2012\)](#) are used for the Fe I.
- $\log g$ : The surface gravity is determined from the ionisation balance of the Fe I lines and 6 Fe II lines. The determined abundance should be the same, independent on the ionisation stage. Surface gravity can also be determined using strong lines since the wings of these lines are pressure sensitive. Wings from two (2) strong Fe I lines have been used in this work. Other I/II pairs can be used to determine the surface gravity, but then this abundance has to be set as a free parameter too. In this work Ti I/II is used as well.
- $[\text{Fe}/\text{H}]$ : Using the determined iron abundances from the  $T_{\text{eff}}$  and  $\log g$  determination, one gets the metallicity  $[\text{Fe}/\text{H}]$ .
- $v_{\text{mic}}$ : The microturbulence is determined by demanding an equal abundance using both weak and strong lines. The reason for this is due to the high sensitivity of saturated lines with line broadening, associated with small-scale motions, which is not the case for weak lines.

The determined stellar parameters (temperature  $T_{\text{eff}}$ ,  $\log g$  and  $[\text{Fe}/\text{H}]$ ) are plotted in [Figure 4.2.1](#). From this we see that the stars follow the plotted isochrones from [Marigo et al. \(2017\)](#), additionally they follow the expected metallicity gradient, which is reassuring.

## 4.3 Abundance determination

### 4.3.1 Line data

As discussed in the beginning of this chapter, [Section 4.1](#), a synthetic spectrum is modelled to fit the observed spectrum using stellar and atomic parameters. The atomic parameters, the wavelength, excitation energy and  $\log gf$ , have to be both precise and accurate to get precise and accurate abundances. Within this, as previously discussed, the broadening of atomic lines has to be considered also. In this work the atomic data from Gaia ESO line list version 6 ([Heiter et al. in prep.](#)) is used.

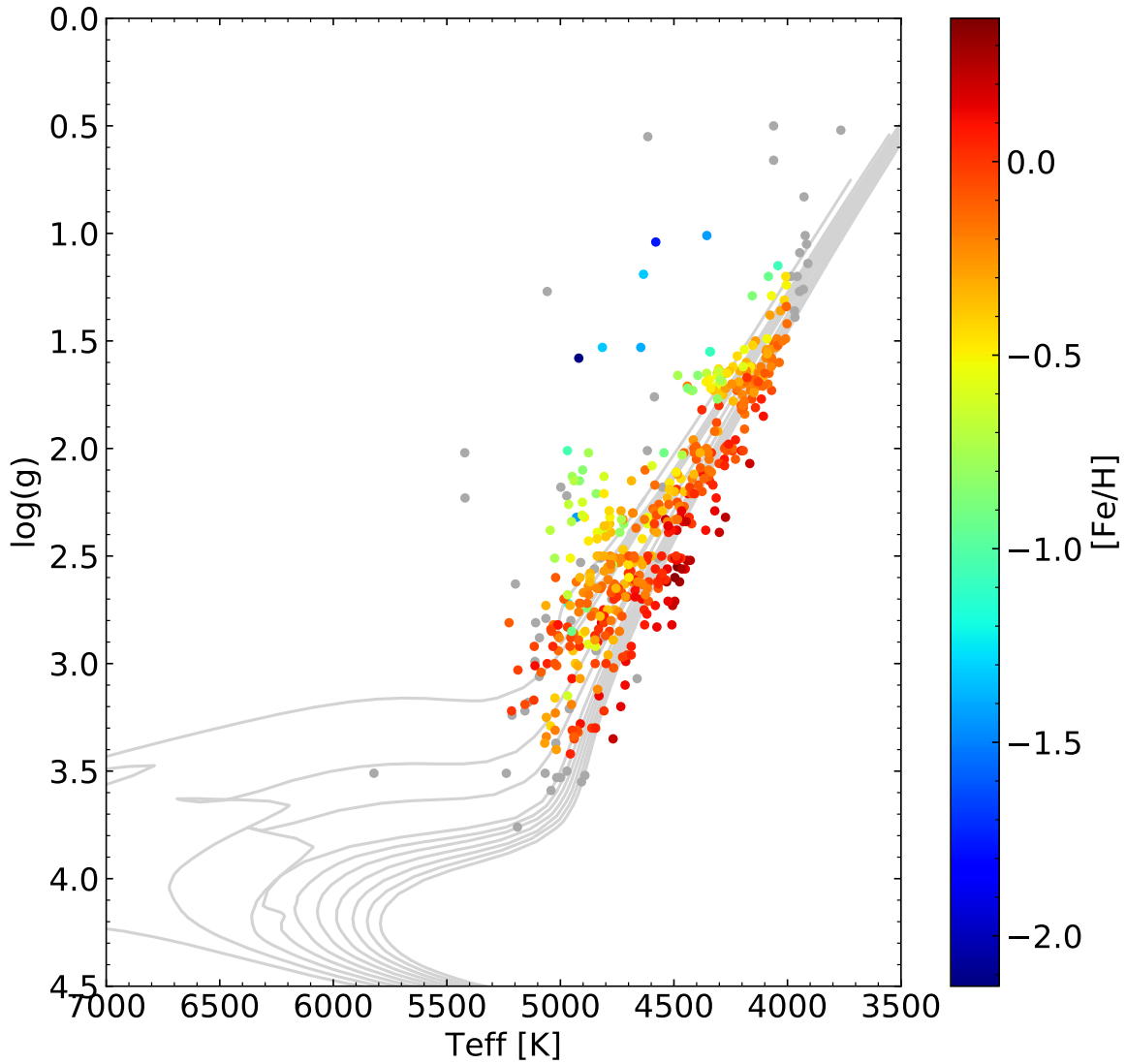


**Figure 4.2.1:** HR-diagram showing the stellar parameters  $\log g$  towards  $T_{\text{eff}}$  with a colour gradient of the metallicity,  $[\text{Fe}/\text{H}]$ . The whole sample of 523 stars is shown. The grey dots are stars that are cut out from the analysis in post processing, described in Section 5.1. The solid grey lines are isochrones of  $[\text{Fe}/\text{H}] = 0$  and ages 1-10 Gyr from [Marigo et al. \(2017\)](#).

### 4.3.2 Examined lines

Lines from the elements are investigated manually and chosen such that these are

- Of suitable strength,
- Not blended with a stronger line
- Not blended with too many lines.

This has been done by simply looking at the spectra and judging from experience which lines can be used in the analysis. An example of a line that is usable and a non-usable line can be seen in Figure 4.3.1 below. Optimally, no blends at all should occur for the line of interest, but this is seldom the case for the neutron-capture element lines considered in this work (in the optical region). On the other hand, very weak lines that can be affected by the spectral noise have not been used in the analysis either. The final choice of lines can be seen in Appendix B and the modelled synthetic spectra for Arcturus can be seen in Appendix A.

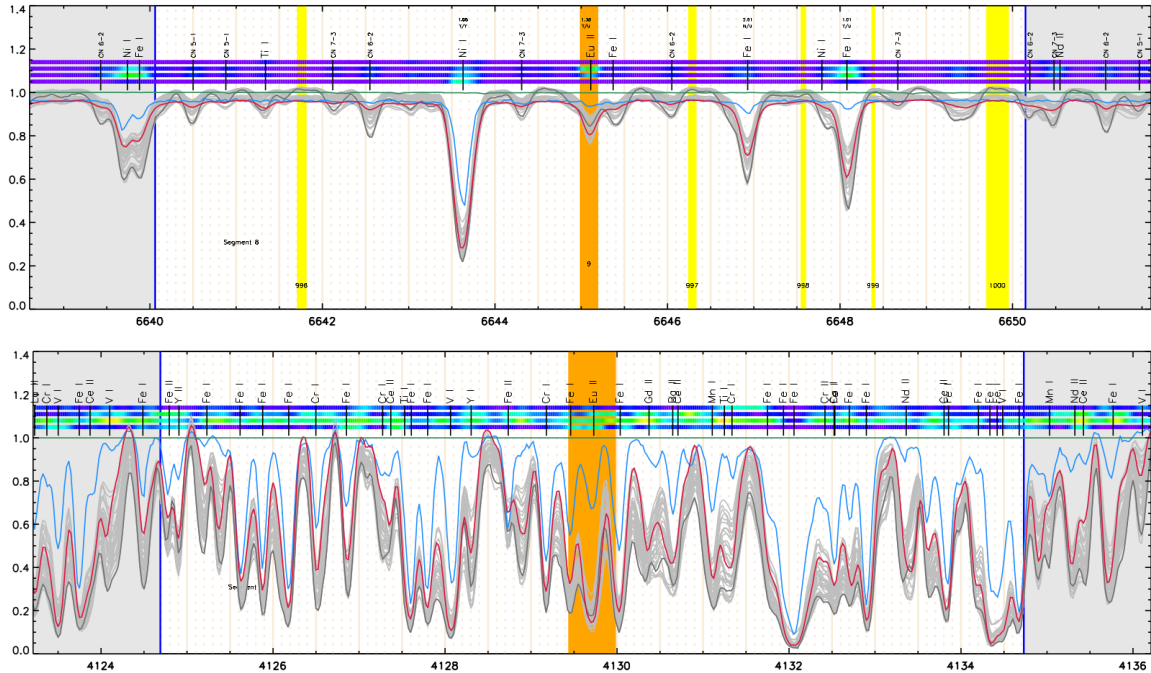


**Figure 4.3.1:** Example figures of a usable(top) and non-usable(bottom) spectral line. The y-axis shows the normalised flux and the x-axis the wavelength. The line of interest is highlighted in orange, whilst the continuum (if any) is marked with yellow. The vertical blue lines marks the segment. A subset of the roughly normalised stellar spectra is plotted in light grey, whilst dark grey is Rasalas/ $\mu$ Leo and the red is Arcturus/ $\alpha$ Boo. The blue is the Solar spectra. In the top figure the europium line used for abundance determination in this work is highlighted. In the bottom another europium line is highlighted. This line is heavily blended with other lines in a region with little continuum, making it difficult to use for abundance determination.

### 4.3.3 Solar values

To scale stellar abundances with respect to the solar value, SME uses solar abundances from [Grevesse et al. \(2007\)](#). I wanted to use the most recent solar values when determining the abundances in this work, and therefore the results have been re-scaled using the solar abundances of [Grevesse et al. \(2015\)](#).

Additionally, the solar values for the elements in this work are determined using three solar spectra obtained by FIES observations of the asteroid Vesta. The mean of the determined abundance from the three spectra is calculated to get a solar value, see [Table 4.3](#). For 5 out of the 9 elements the spectral lines are extremely weak in the Sun and therefore could not be used. A non-zero solar value can indicate systematic uncertainties. As mentioned in [Section 4.5](#), it is difficult to determine wherein these uncertainties lie, however the values for both Cu and Y are somewhat concerning.

**Table 4.3:** The determined solar value using the chosen spectral lines in this work. The value are normalised using [Grevesse et al. \(2015\)](#). Elements marked with '-' do not have visible lines in the solar spectra.

Element	[Cu/Fe]	[Y/Fe]	[Zr/Fe]	[La/Fe]	[Ce/Fe]
Solar	-0.12	-0.19	-	0.04	-
Element	[Pr/Fe]	[Nd/Fe]	[Eu/Fe]	[Gd/Fe]	
Solar	-	-	-0.07	-	

## 4.4 Thin & thick disk separation

As already mentioned in the Introduction, the Galactic disk has been shown by [Gilmore & Reid \(1983\)](#) to require two components in fitting the density distribution observed in the Solar neighbourhood. This result points towards the disk consisting of two stellar populations, often referred to as the *thin* and the *thick* disk, due to the scale heights of these. The thin disk has a scale-height of  $\sim 300$  pc, whereas the thick disk extends to somewhere around 1 kpc ([Bland-Hawthorn & Gerhard 2016](#)). A clean cut, or a gradient, between these two populations is yet to be found and may not exist. In this section I will elaborate more on the disk populations and describe how the separation of the disks is treated in this work.

By further investigations of these two disks, it has become clear that the classification of these also can be done in other ways: by kinematics, age and chemistry. For the kinematic picture, it has been shown that, in general, stars belonging to the thick disk rotate around the Galaxy centre at lower rotational velocities (about 40-50 km/s slower) although they have higher total velocities. Therefore the separation of the disks can be done considering the velocities, where stars above a given stellar velocity, often taken to be 70 km/s ([Nissen 2004](#)), are considered to be thick disk stars.

The higher total velocities of thick disk stars can be explained by considering the ages of the stars: the thick disk stars are in general older than the thin disk stars. This means that they will have more time to be scattered and gain higher total velocities ([Bensby et al. 2014](#)). The given age separation is stated to be around 8 Gyr, where thick disk stars are older,  $> 8$  Gyr,

and vice versa. However, it is hard to determine the ages of giant stars since the age estimation often is done by using isochrones, which blend together for the RGB (where the stars in my stellar sample are found, see the isochrones in Figure 4.2.1). Age estimation can also be done using evolutionary models to reach the initial mass of the star (Ness et al. 2016). This method requires the *present* stellar mass which can be measured by either asteroseismology (Lagarde et al. 2015) or by abundance determination of carbon and nitrogen (see Martig et al. (2016)).

Considering the chemical picture, the thick disk stars have been shown to extend to lower metallicities than the thin disk stars as well as having higher abundance of the  $\alpha$ -elements, at a given metallicity, (see e.g. Adibekyan et al. (2011)). This has led to another set of names for the disks, the high- and low- $\alpha$  disks which is described in Bensby et al. (2007) where the [Ti/Fe] abundance is used to separate the two disks. Additionally, Bensby et al. (2014) found that stars older than 8 Gyr, are  $\alpha$ -element rich, compared with the low- $\alpha$  disk which contains more young stars.

An additional idea to explain the two populations in the disk is an inner and an outer disk hypothesis. In Hayden et al. (2015) a rather detailed picture of this classification is given. They note that the abundance pattern for the inner Galaxy can be described by only one disk sequence, starting at low metallicities and high  $[\alpha/\text{Fe}]$ -abundances and ends at approximately solar  $[\alpha/\text{Fe}]$  and at metallicities of -0.5. The most metal-rich stars in this sequence are found at Solar abundances. On the other hand, the outer disk seems to lack high- $[\alpha/\text{Fe}]$  stars and is primarily composed of solar- $[\alpha/\text{Fe}]$  stars. Additionally, this outer disk seems to flare at the edges (Hayden et al. 2015). This suggests that what we locally observe as the thin disk might be an outer disk and the thick one might be an inner disk (Haywood et al. 2019).

In this work, the disk separation is done using (primarily) the chemical classification of the disks. This is done using the abundance of the  $\alpha$ -element magnesium, which shows a clear gap at subsolar metallicities in my data. Additionally, some stars are separated using kinematics from the second data release from Gaia (Gaia DR2) (Gaia Collaboration et al. 2018), where the separation using abundances became impossible. I chose to call the disks thin and thick throughout the remainder of this work, however, it is important to note, strengthened by the background presented to this subject, that the results and following discussion on these might differ somewhat depending on how the classification is done.

Furthermore, the lowest metallicity stars,  $[\text{Fe}/\text{H}] \lesssim -1.2$  are classified as halo stars. The halo stars are in general chemically similar to those of the metal-poor thick disk stars, but are older and have higher total velocities. Moreover they have much greater scale heights and are found outside the disk.

The  $\alpha$ -element abundances in the stars were determined by my supervisor, Henrik Jönsson, using the same method as described previously in this chapter. The separation of the thin and thick disk was made by me, primarily by using the magnesium abundance, indicated in the top plot in Figure 4.4.1. The result for magnesium and four additional  $\alpha$ -elements, oxygen (O); silicon (Si); calcium (Ca) and titanium (Ti), can be seen in Figure 4.4.1. As seen in this figure, the high- $\alpha$  disk is clearly separable from that of the low- $\alpha$  disk, whereas the halo stars are more or less a flat extension of the thick disk. This is due to the production of Fe and  $\alpha$ -elements, primarily coming from SNe II at lower metallicities, until SNe Ia stars begin to enrich the ISM with Fe, but not  $\alpha$ , and the trend decreases.

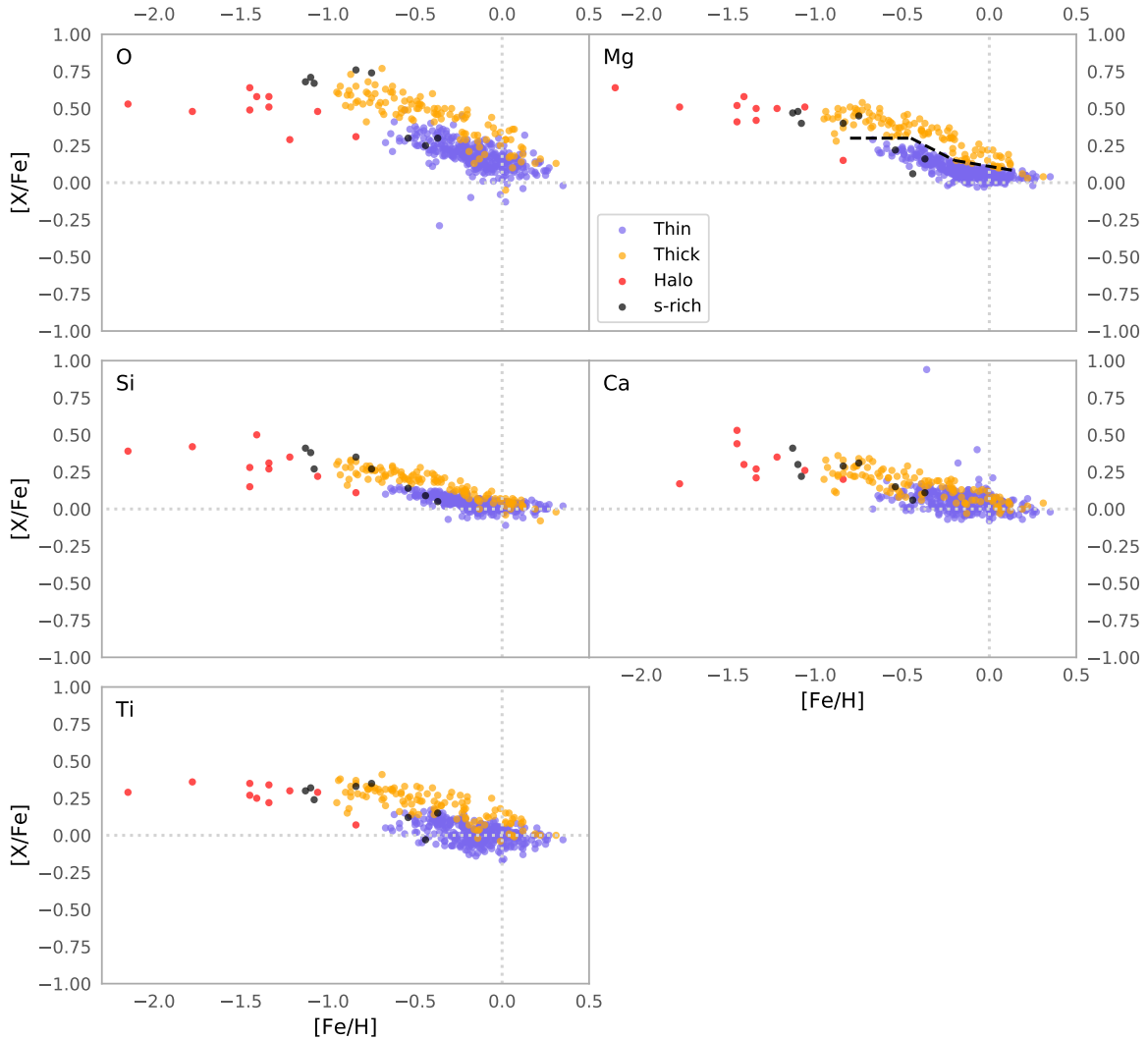


**Figure 4.4.1:** Separation of disk populations in  $\alpha$ -elements,  $[O, Mg, Si, Ca, Ti/Fe]$  for the stellar sample. At metallicities between  $-0.9$  to  $0.15$ , the separation is done using the magnesium abundance, indicated by black dashed line (top right plot). Description of how the higher- and lower metallicity stars are classified using kinematics can be found in the text. Red are halo stars, yellow thick disk, blue thin disk and black s-process rich. The s-process enriched stars was selected from the abundance trends of the s-process elements, which can be seen in the result section, see for instance Figure 5.2.2.



However, at both low and high metallicities it is hard to put a limit on which stars that are either disk or halo stars, or belongs to the thin or the thick disk, respectively. Both the thick disk and halo stars have been shown to have systematically lower rotational velocities ( $V$ ) whilst having a larger total velocity ( $V_{\text{tot}}$ ), eq. (4.4), than the thin disk stars. This can be used to separate the stars that can not be classified via the magnesium abundance at high metallicities, whilst the lower rotational velocities of halo stars can be used to separate them from the thick disk stars at the low metallicity end.

$$V_{\text{tot}} = \sqrt{U^2 + V^2 + W^2}, \quad (4.4)$$

To calculate the space velocities ( $U, V, W$ ) I use kinematics (proper motions, positions) from Gaia DR2 [Gaia Collaboration et al. \(2018\)](#), radial velocities from my own measurements and distances from [McMillan \(2018\)](#). To show the velocities, I plot a Toomre diagram, see Figure 4.4.2, which is a representation of the combined vertical and radial kinetic energies versus the rotational energy. In [Nissen \(2004\)](#), a star with a total velocity less than 50 km/s is judged to most probably be thin disk star whereas stars with total velocity between 70 to 200 km/s are most probably thick disk stars and stars with higher total velocities than 200 km/s are most probably halo stars. For the highest metallicity stars in Figure 4.4.1, where the Mg abundance can not be used to separate the thin and the thick disk,  $V_{\text{tot}}$  is used.

The total velocities of the stars can be seen in the Gaussian distributions in the lower right histogram in Figure 4.4.3. The distributions cross at  $V_{\text{tot}} = 70.2$  km/s: the high metallicity stars found with a total velocity lower than this are classified as thin disk stars, and the ones with higher total velocity as thick disk stars. Additionally, in Figure 4.4.3, the distribution of the velocities can be seen, where both the thick disk and halo stars have a systematically lower rotational velocity  $V$  and higher total velocity  $V_{\text{tot}}$  than the thin disk stars.

The resulting positions and distances of the stars can be seen in Figure 4.4.4. From this figure one can see that the halo stars extend to higher scale heights ( $z$ ) and distances than the thin and thick disk stars. Additionally, the thick disk stars have a higher scale height than the thin disk stars. Here it is clear that the chemical separation places some thin disk stars at scale heights higher than 300 pc, which is necessary to keep in mind.

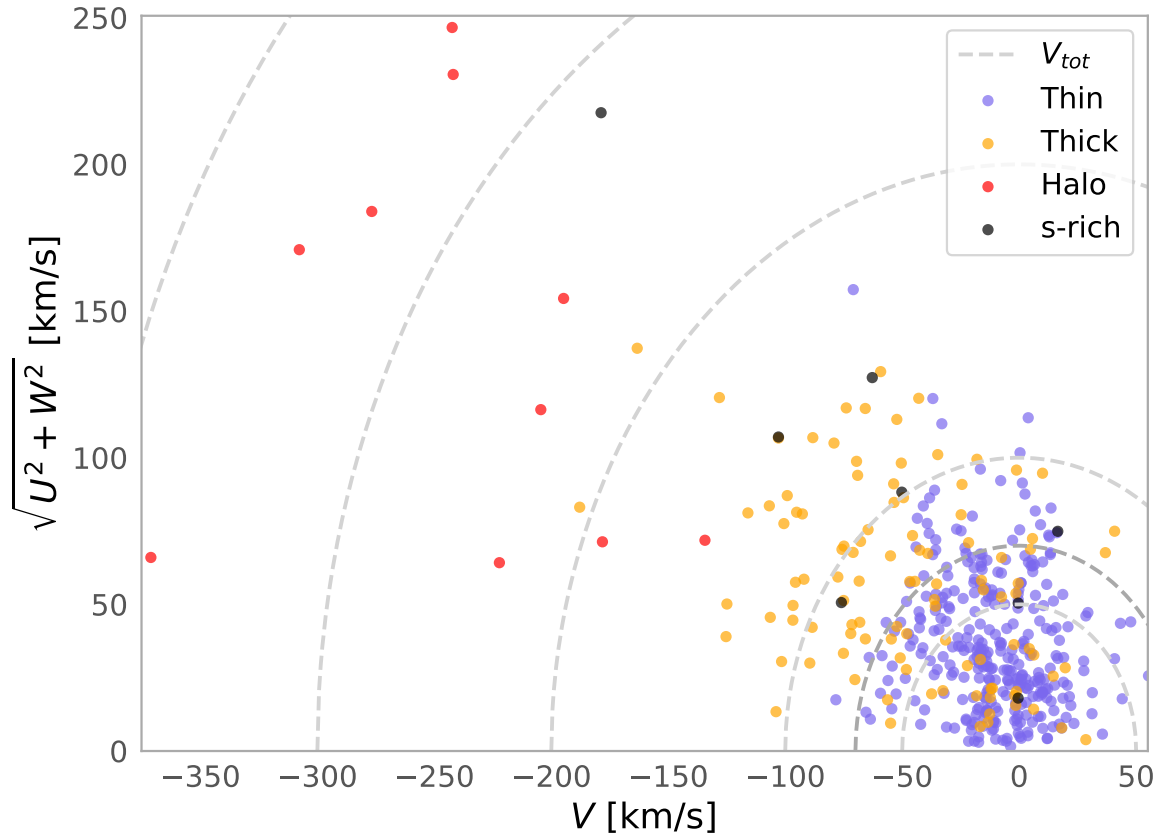


**Figure 4.4.2:** Toomre diagram of the stars in my sample. The grey dashed lines indicate a total velocity, eq. (4.4) of 50, 70, 100, 200, 300 and 400 km/s. In Nissen (2004) stars with  $V_{\text{tot}} < 50$  km/s are most probably thin (blue) disk stars, stars with  $70 < V_{\text{tot}} < 200$  km/s are most probably thick (orange) disk stars and  $V_{\text{tot}} > 200$  km/s are most probably halo (red) stars. Similarly I find that 70 km/s is the border between stars being most probable thin or thick disk stars, described in the text.

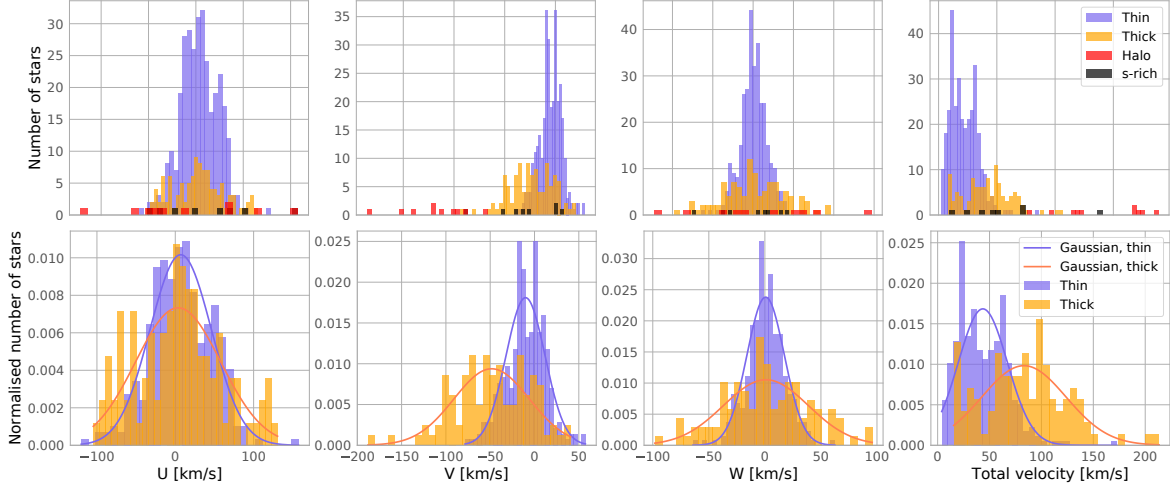


**Figure 4.4.3:** The velocity distributions of the different stellar populations. The upper row shows the number of stars, whilst the bottom row shows the normalised number of stars. Note that the normalised plot does not include the halo (red) or the s-enriched (black) stars. The crossing of the Gaussian distributions in the right-most histogram ( $V_{\text{tot}}$ ) is used to separate the high metallicity stars into the thin (blue) or thick (orange) disk. See Figure 5.2.2 for how the s-process rich stars were selected.

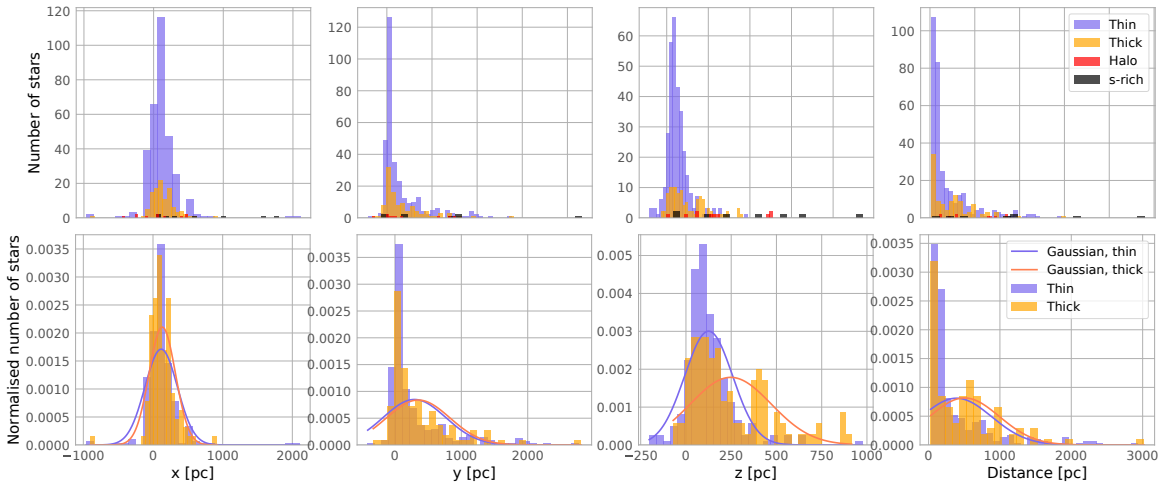


**Figure 4.4.4:** Same as Figure 4.4.3, instead showing the positional distributions of the different stellar populations.

## 4.5 Abundance uncertainties

### 4.5.1 Systematic uncertainties

Systematic errors, generally originate from incorrectly determined stellar parameters, model atmosphere assumptions and atomic data. This makes the errors hard to estimate. To get a sense of the systematic uncertainties, one often uses a reference star. For spectroscopic works using dwarfs, the Sun is a good example of a reference star to normalise with. For samples with giant stars, the Sun is not a suitable reference and there are no giant stars that are as extensively investigated and well-known as the Sun. However, Arcturus, or  $\alpha$ -Boo, a red K-giant with an estimated age of 7 Gyr, is a fairly well-studied star (Ramírez & Allende Prieto 2011). Arcturus has been analysed extensively due to its brightness, being the fourth brightest in the night sky, and could thus work as a reference of a typical giant star. Additionally, Rasalas, or  $\mu$ -Leo is a well-studied K giant star which can be used as a reference too<sup>5</sup>. Arcturus is a low metallicity star with  $[\text{Fe}/\text{H}] = -0.55$  whilst Rasalas has a higher metallicity of  $[\text{Fe}/\text{H}] = 0.27$ , see Table 4.4.

As it is important to have an accurate estimation of the stellar parameters, the ones determined in this work are compared with stellar parameters for two of the stars in my stellar sample available in the Gaia benchmark sample presented by Jofré et al. (2015), being Arcturus and Rasalas. The comparison can be seen in Table 4.4. The stellar parameters in this work are within the uncertainties for the Gaia benchmark parameters, except for the microturbulence of Arcturus that is off by almost 0.2 dex. However, this amount will hardly affect the model atmospheric structure, in addition to that I use weak lines in this work, where  $v_{\text{mic}}$  has a very small influence on my abundances. The otherwise excellent agreement for these two references thus suggest that there are no clear systematic uncertainties in the stellar parameters.

**Table 4.4:** Stellar parameters of overlapping Gaia benchmark stars. Top row: the results presented in Jofré et al. (2015); Bottom row: the stellar parameters used in this work.

Stellar name/HIP	$T_{\text{eff}}$ [K]	$\log g$ [dex]	$[\text{Fe}/\text{H}]$ [dex]	$v_{\text{mic}}$ [km/s]
$\alpha$ Boo/HIP 69673	$4286 \pm 35$	$1.64 \pm 0.09$	$-0.57 \pm 0.08$	$1.58 \pm 0.12$
This work	4308	1.66	-0.55	1.77
$\mu$ Leo/HIP 48455	$4474 \pm 60$	$2.51 \pm 0.11$	$0.20 \pm 0.15$	$1.28 \pm 0.26$
This work	4494	2.51	0.27	1.53

### 4.5.2 Random uncertainties

SME calculates uncertainties to the determined abundances, however this uncertainty is solely based on the noise in the spectra and is thus unrealistically small and not representative of *true* uncertainties. Instead, estimates on how random uncertainties in the stellar parameters affect the determined abundance is computed in this section. Since the spectra of the stellar

<sup>5</sup>It should be noted that  $\mu$ -Leo is the host of a 2.4 Jupiter mass giant planet (Lee et al. 2014), which might cause it to be depleted in some (refractory) elements, see Meléndez et al. (2009). This is on a very small scale of 0.05 dex however.

sample originate from the same instrument (FIES), the risk of possible differential systematic uncertainties from instrumental artifacts and/or reduction is minimised. All spectra are analysed using the same line and continuum masks, and additionally the same atomic data, which minimises the random uncertainties. Therefore, the random uncertainties are considered to primarily be found in the (random) uncertainties of the stellar parameters.

### ”Standard” method

Often, general abundance uncertainties are assessed by analysing the spectrum of a representative star with offset stellar parameters. I chose two typical reference giant stars from the stellar sample; Arcturus (also known as  $\alpha$ -Boo, HIP 69673) and Rasalas (also known as  $\mu$ -Leo, HIP 48455). I altered the stellar parameters of these two stars, following the routine in Jönsson et al. (2017a):  $T_{\text{eff}} \pm 50$  K,  $\log g \pm 0.15$  dex,  $[\text{Fe}/\text{H}] \pm 0.05$  dex and  $v_{\text{mic}} \pm 0.1$  km/s and measured the resulting determined abundance for the neutron-capture elements. As is customarily done, ignoring the correlations which are difficult to evaluate, the effect on the random uncertainties can be calculated, taking into account the stellar parameters, as

$$\sigma_{A_{\text{parameters}}} = \sqrt{|\delta A_{T_{\text{eff}}}|^2 + |\delta A_{\log g}|^2 + |\delta A_{[\text{Fe}/\text{H}]}|^2 + |\delta A_{v_{\text{mic}}}|^2}. \quad (4.5)$$

The result for both stars can be seen in Table 4.5. Note that for non-symmetrical abundance changes for the same stellar parameter the mean value was used in the squared sums. From these results one sees that all elements, other than Zr, are sensitive to changes in the surface gravity,  $\log g$ . On the other hand, Zr is much more sensitive to changes both in effective temperature and metallicity. The mean of the  $\sigma_{A_{\text{parameters}}}$  for Arcturus and Rasalas is then set as the uncertainty ‘Mean  $\sigma_{A_{\text{parameters}}}$ ’, which gives uncertainties between 0.06 (Y) and 0.10 (Zr). In general, Rasalas has larger uncertainties than Arcturus, something that also can be seen for the Gaia benchmark stars, Table 4.4.

Since this method neglects the fact that stellar parameters are correlated in a complex manner, the uncertainties calculated this way are likely to be overestimated. Therefore, they should be taken as an upper limit of the uncertainties. However, due to the complexity of the correlation between stellar parameters, uncertainties are often estimated in this way, as if they were uncorrelated.

### Monte Carlo method

Another, more general, approach to estimate the random uncertainties due to changes in the stellar parameters, is to analyse the same standard spectra several times using parameters that all vary within a given distribution. I chose to use a Gaussian distribution to generate the uncertainties, using the same range as in the previous section, i.e 50 K standard deviation in  $T_{\text{eff}}$ , 0.15 dex in  $\log g$ , 0.05 dex in  $[\text{Fe}/\text{H}]$  and 0.1 km/s in  $v_{\text{mic}}$ . The uncertainties were added to the initial stellar parameters of Arcturus and Rasalas (seen in Table 4.4), meaning that all four stellar parameters were changed simultaneously. This is in contrast to the method above, where the uncertainties were applied one-by-one. Similar to the sample size, a total of 500 abundance measurements were carried out using the Arcturus and Rasalas spectrum with modified stellar parameters.

The resulting standard deviation in the determined abundance for the 500 Monte Carlo runs was calculated and can be seen in the last columns of Table 4.5. The mean of the  $\sigma_{\text{AMC}}$  for Arcturus and Rasalas is calculated and set as the uncertainty  $\sigma_{\text{AMC, mean}}$ . The resulting abundances<sup>6</sup> and probability density functions of these can be seen in Figure 4.5.1 for Arcturus and 4.5.2 for Rasalas.

I conclude that, changing the stellar parameters one at a time (standard method) does not differ significantly from changing them simultaneously, using normal distributed uncertainties (Monte Carlo method). Therefore, the uncertainties calculated using the Monte Carlo method are the ones used in the analysis and displayed as the typical error for all stars in the plots.

### Line-by-line method

To estimate other sources of error one can also calculate the line-by-line dispersion, using either a typical reference star or for all stars. Doing this, one can get a measurement of the uncertainties that can arise from the continuum placement, S/N ratio, uncertainties in atomic data ( $\log gf$ -values), unknown line blends and problems with the modelled stellar atmosphere, i.e a combination of random and systematic uncertainties. However, this method requires that the abundance is determined with more than one line, which is not the case for almost half of the elements in this work (Cu, Nd, Eu, Gd) and this method is therefore not explored in this work.

---

<sup>6</sup>The abundances  $A(X)$  are calculated using eq. 4.2 where  $A(X) = \log_{10} (N_X/N_Y)_{\text{star}} + 12$ , following the notation in Asplund et al. (2009)

**Table 4.5:** This table shows the uncertainties in the determined abundances of the typical giant stars Arcturus and Rasalas. The results from the standard method is shown at the top beginning with Arcturus and Rasalas follows. The uncertainties are induced by an uncertainty in one of the stellar parameters, indicated in the left column, one at a time. The  $\sigma_{A_{\text{parameters}}}$  are calculated as in eq. (4.5), showing the combined uncertainty. The mean from these is indicated as 'Mean  $\sigma_{A_{\text{parameters}}}$ '. The results from the Monte Carlo method and the calculated mean from these are seen in the last three rows.

Uncertainty	$\delta A(\text{Cu})$ [dex]	$\delta A(\text{Y})$ [dex]	$\delta A(\text{Zr})$ [dex]	$\delta A(\text{La})$ [dex]	$\delta A(\text{Ce})$ [dex]	$\delta A(\text{Pr})$ [dex]	$\delta A(\text{Nd})$ [dex]	$\delta A(\text{Eu})$ [dex]	$\delta A(\text{Gd})$ [dex]
$\delta T_{\text{eff}} = +50 \text{ K}$	0.00	0.00	+0.09	+0.01	+0.02	0.00	+0.03	-0.02	+0.01
$\delta T_{\text{eff}} = -50 \text{ K}$	-0.01	0.00	-0.1	0.00	-0.02	-0.01	0.00	+0.01	0.00
$\delta \log g = +0.15 \text{ dex}$	+0.05	+0.06	+0.01	+0.05	+0.09	+0.06	+0.06	+0.06	+0.07
$\delta \log g = -0.15 \text{ dex}$	-0.04	-0.04	-0.01	-0.05	-0.03	-0.05	-0.04	-0.06	-0.04
$\delta [\text{Fe}/\text{H}] = +0.05 \text{ dex}$	+0.02	+0.02	+0.05	+0.03	+0.05	+0.03	+0.05	+0.02	+0.03
$\delta [\text{Fe}/\text{H}] = -0.05 \text{ dex}$	-0.03	-0.02	-0.06	-0.03	-0.01	-0.03	-0.02	-0.03	-0.02
$\delta v_{\text{mic}} = +0.1 \text{ km/s}$	-0.03	0.00	-0.01	0.00	-0.02	0.00	0.00	0.00	0.00
$\delta v_{\text{mic}} = -0.1 \text{ km/s}$	+0.02	0.00	+0.01	+0.01	+0.02	0.00	+0.01	0.00	0.00
$\sigma_{\text{parameters}}$ [dex]	0.06	0.05	0.11	0.06	0.11	0.07	0.06	0.07	0.06
$\delta T_{\text{eff}} = +50 \text{ K}$	+0.01	+0.01	+0.07	+0.01	+0.02	0.00	+0.02	0.00	0.00
$\delta T_{\text{eff}} = -50 \text{ K}$	0.00	+0.01	-0.10	-0.01	+0.03	-0.01	-0.01	+0.02	-0.01
$\delta \log g = +0.15 \text{ dex}$	+0.06	+0.06	0.00	+0.07	+0.09	+0.06	+0.07	+0.08	+0.06
$\delta \log g = -0.15 \text{ dex}$	-0.08	-0.07	-0.04	-0.09	-0.06	-0.08	-0.07	-0.08	-0.08
$\delta [\text{Fe}/\text{H}] = +0.05 \text{ dex}$	-0.04	-0.02	-0.07	-0.04	-0.01	-0.04	-0.03	-0.03	-0.03
$\delta [\text{Fe}/\text{H}] = -0.05 \text{ dex}$	+0.04	+0.04	+0.04	+0.03	+0.06	+0.03	+0.04	+0.05	+0.02
$\delta v_{\text{mic}} = +0.1 \text{ km/s}$	-0.04	0.00	-0.04	-0.01	+0.02	0.00	0.00	+0.01	-0.01
$\delta v_{\text{mic}} = -0.1 \text{ km/s}$	+0.04	+0.02	+0.01	+0.01	+0.03	0.00	+0.01	+0.01	0.00
$\sigma_{A_{\text{parameters}}}$ [dex]	0.09	0.07	0.11	0.09	0.09	0.08	0.08	0.09	0.7
Mean $\sigma_{A_{\text{parameters}}}$ [dex]	0.08	0.06	0.11	0.08	0.10	0.08	0.07	0.08	0.07
$\sigma_{A_{\text{MC}}}(\alpha\text{- Boo})$ [dex]	0.06	0.06	0.12	0.06	0.06	0.06	0.07	0.06	0.06
$\sigma_{A_{\text{MC}}}(\mu\text{- Leo})$ [dex]	0.09	0.07	0.11	0.08	0.08	0.07	0.08	0.08	0.07
Mean $\sigma_{A_{\text{MC}}}$ [dex]	<b>0.08</b>	<b>0.07</b>	<b>0.12</b>	<b>0.07</b>	<b>0.07</b>	<b>0.07</b>	<b>0.08</b>	<b>0.07</b>	<b>0.07</b>

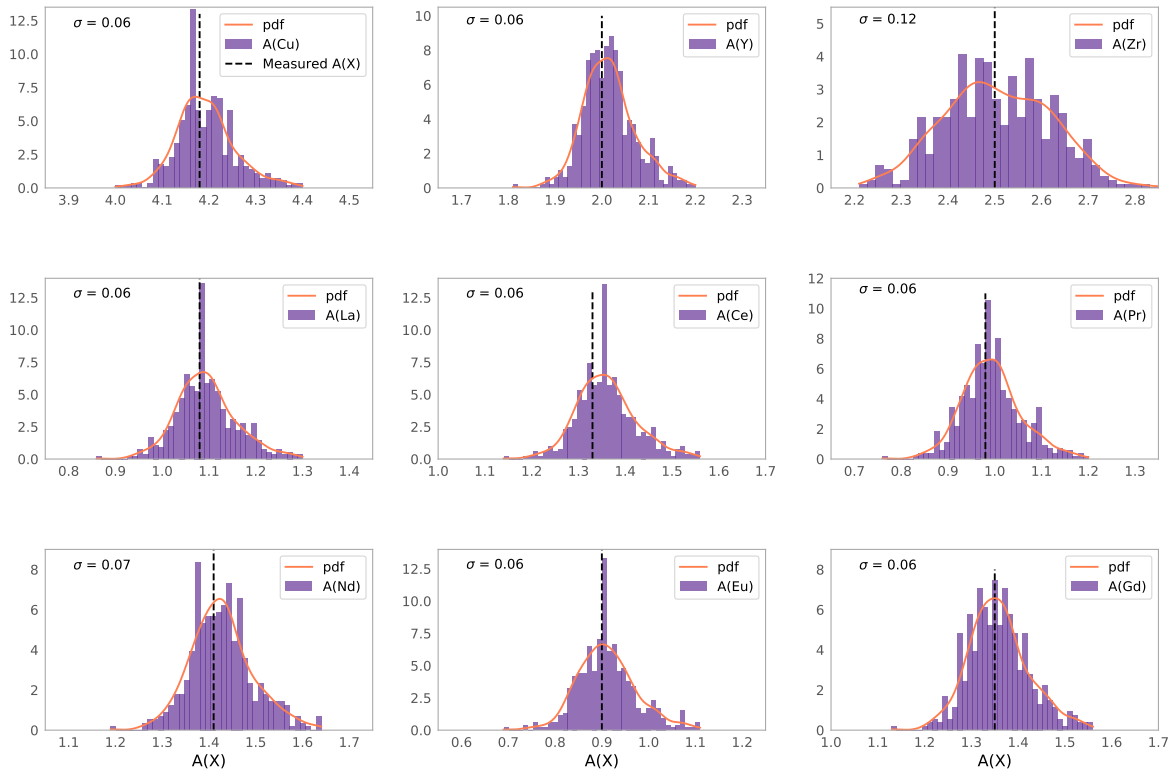


**Figure 4.5.1:** The abundance distribution of the Monte Carlo calculations of Arcturus ( $\alpha$ -Boo). A probability density function (orange) is fitted to the distributions (purple) and the standard deviation is noted in the upper left corner of every element. The measured abundance from the unaltered stellar parameters is marked with a dashed black line.



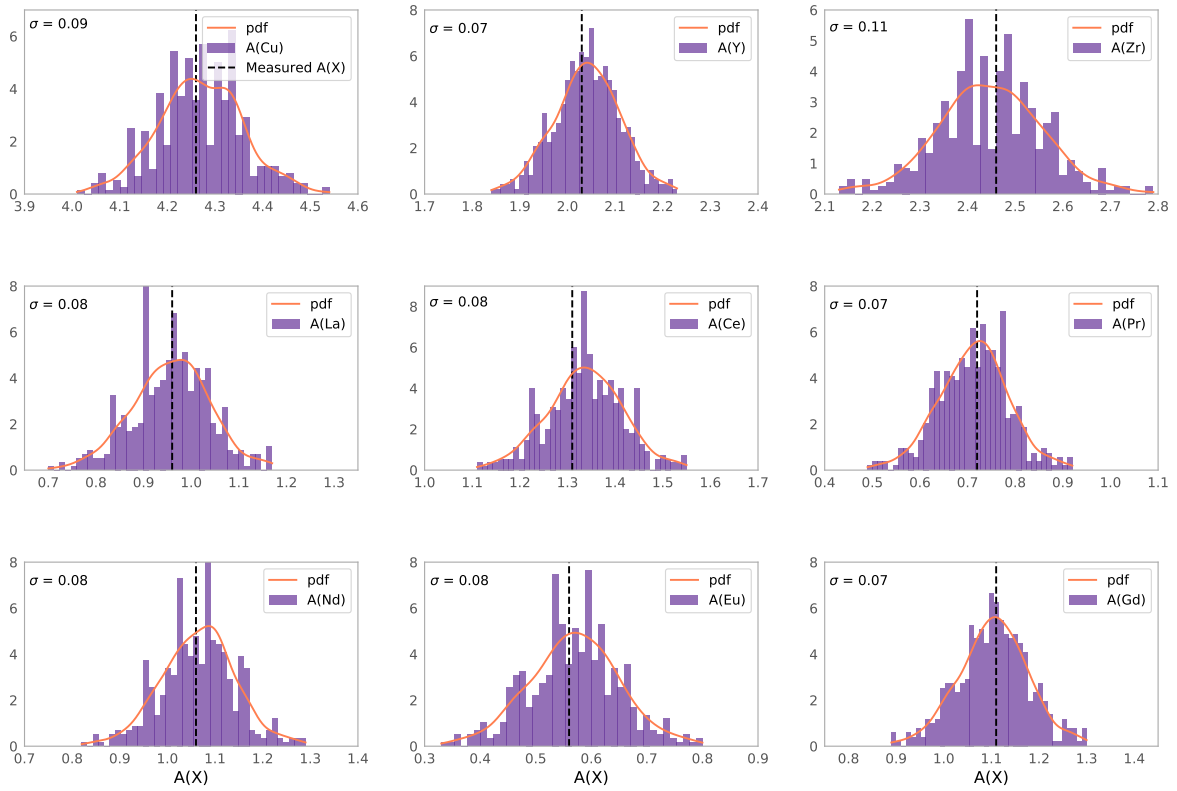


Figure 4.5.2: Same as Figure 4.5.1 but for Rasalas ( $\mu$ -Leo) instead.

## Chapter 5

# Results & discussion

In this chapter I go through the results of the abundance determination. Firstly, in Section 5.2, the results are compared with surveys done of dwarf stars, namely [Mishenina et al. \(2013\)](#), [Bensby et al. \(2014\)](#), [Battistini & Bensby \(2016\)](#) and [Delgado Mena et al. \(2017\)](#) for validation of the abundances determined in this work. In short, I judge that the work presented in this work is consistent with previous work on dwarfs and can therefore conclude that I have managed to overcome the challenges with analysing giant stars.

In general, the abundances have been plotted as a function of metallicity,  $[X/Fe]$ , against  $[Fe/H]$ , to see the evolution of the elements with iron as reference. Additionally, the ratio with magnesium,  $[X/Mg]$ , has been plotted over the  $[Mg/H]$ -ratio. Magnesium is enriched in the Galaxy by SNe II only, whilst iron is enriched by both SNe II and SNe Ia. Therefore, the magnesium abundance in stars can work as a better proxy for time. However, these plots show similar results to that of the iron-plots, which are more customary to use, and can therefore be seen in Appendix C.

The stellar sample has been divided into the stellar populations defined and described in Section 4.4. For the thin and thick disk stellar populations the running mean has been calculated with a  $1\sigma$  scatter deviation. A more in-depth comparison of the neutron-capture elements with each other is found in Section 5.3. From those elements with a dominating contribution from the main s-process, Y to Nd, some s-process-enriched stars can be seen clearly, marked with black in Figure 5.2.2. These are elaborated on more in Section 5.4. In Section 5.5 I investigate the age- $[Y/Mg]$  relation reported in previous studies. To conclude the chapter I also comment briefly on the elements where abundance determination was not possible, seen in Section 5.6.

## 5.1 Data selection

From the stellar sample of 523 stars, quality cuts have been made in all plots. The first cut is based on discarding stars that are not giant stars as well as spectra and stellar parameters that are not of sufficient quality, such that

$$\begin{aligned} S/N &\geq 50 \\ T_{\text{eff}} &\geq 4000 \text{ K} \\ \log g &\leq 3.5 \\ 1 &\leq v_{\text{mic}} \leq 2 \text{ km/s} \\ 3 &\leq v_{\text{mac}} \leq 7 \text{ km/s} \end{aligned}$$

which is applied to all elements. This leaves 465 stars. Secondly, all synthetic spectra, each line of each element for each star, in total 12029, have been checked manually by eye to ensure the goodness of fit with the observed stellar spectra. If the fit is not sufficiently good, the star has been cut out of the final sample, meaning that each element has its own subset of the stellar sample. Some examples for lines that have been cut away are lines that disappear at lower metallicities, or where blends have not been modelled properly. In general, the synthetic spectra modelled the observed spectra well and the elements have somewhere between 444(Zr)-463(Cu) stars in their subsets.

The properties of the data can be seen in Table 5.1, where, in general, the cut sample is very similar to that of the uncut sample, see Table 3.2. The stars are on average closer with a mean distance of 457 kpc, compared to the mean distance of 503 kpc for the uncut sample. The abundance trends including all stars can be seen in Appendix C.

**Table 5.1:** Properties of the data after applying the first quality cut. The properties for the uncut sample is seen in Table 3.2.

S/N (min/median/max)	50/103/306
Distance (min/median/max) [pc]	30/200/3295
V-magnitudes (min/median/max)	-0.05/6.90/12.96
Exposure times (min/median/max) [s]	3/400/7200

## 5.2 Previous work and the disk populations

As mentioned in Chapter 2, the stellar mass and metallicity are factors that contribute to, and affect, the s- and r-process production. Due to this, the enrichment of the ISM and the abundance of neutron-capture elements vary with time in the Galaxy. Since it is suggested from theory that the (main) s-process production takes place in AGB stars, which have a time delay in the Galaxy, it should also be seen in my observations. For the weak s-process, the production in massive stars differs from that in the AGB stars, partly because of the lack of time delay, but also due to the secondary process resulting in a metallicity dependent yield. As for the r-process, the production sites are not yet constrained but the neutron-rich

environment required points at energetic and/or transit events, such as different types of SNe II and/or neutron star mergers.

### 5.2.1 Weak s-process: Cu

Considering the constantly increasing Cu abundance when compared to the abundance of Mg, see Figure 5.2.1, it becomes clear that Cu is produced by a metallicity-dependent yield (remember that Mg is enriched in the Galaxy by SNe II and can be used as a good proxy for time).

Additionally, considering the separation of the stellar populations in the [Cu/Fe] trend, Figure 5.2.2, it becomes clear that the thick disk and halo stars diminish monotonically at lower metallicities. This matches the theory of Cu being produced both by the (secondary) weak s-process as well as production from explosive nucleosynthesis in SNe II. The trend is increasing with increasing metallicities due to the secondary nature of the weak s-process, being metallicity-dependent.

The thick disk stars have on average higher Cu abundances than the thin disk stars. The onset of SNe Ia that produces a majority of Fe, which in these results seems to kick in at around [Fe/H]  $\sim$  -0.6, can be seen in both disks. The abundance for the thick disk stars flattens out whilst the thin disk abundances increase in spread. At solar metallicities the metallicity-dependent yield takes over and the trend increases again. These results are very similar to those of Delgado Mena et al. (2017), see Figure 5.2.6.

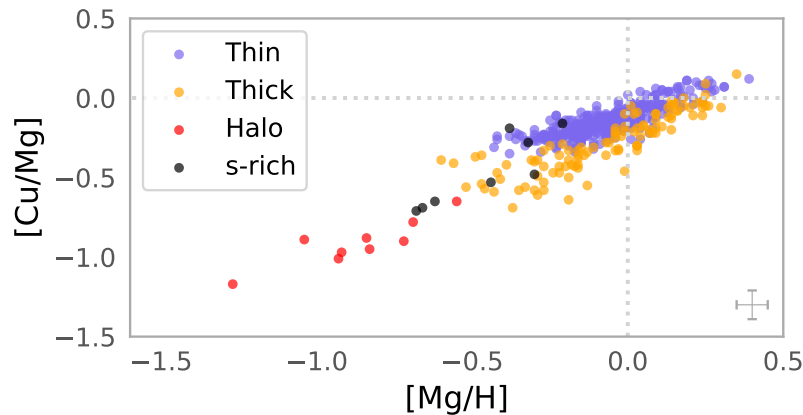


**Figure 5.2.1:** [Cu/Mg] plotted versus the abundance of magnesium, [Mg/H], for the stellar populations, colours the same as for previous plot. The dashed grey lines indicate the solar value at (0,0) and can be seen throughout almost all plots in the thesis. The typical uncertainty is indicated in the the lower right corner the plot, where the uncertainty in [Mg/H] is assumed to be 0.05, from Jönsson et al. (2017a).

A correlation between Cu and the main s-process-dominated element Ba was first found by Castro et al. (1999). In their work, they used a small sample of metal-rich stars and the results indicated an anticorrelation between Cu and Ba. Ba is in the second s-process peak, produced by the main s-process in AGB stars. An anticorrelation between these elements

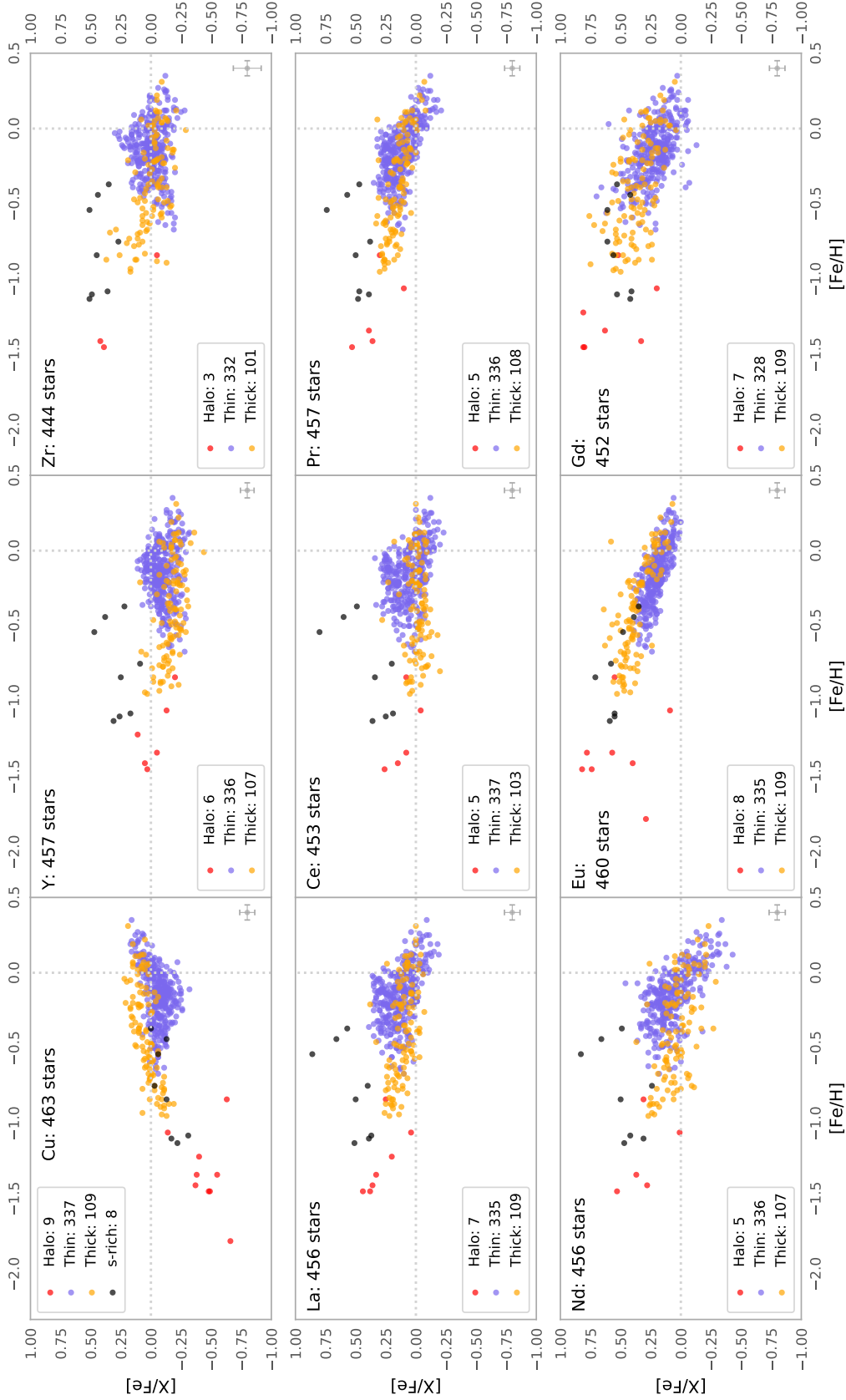


**Figure 5.2.2:** Determined abundances,  $[X/Fe]$ , plotted against the metallicity  $[Fe/H]$  for the different stellar classifications, as described in Section 4.4. The number of stars for each element and each stellar population is indicated in each plot, where the number of s-enriched stars is the same for all elements. The typical uncertainty is indicated in the lower right corner of every plot.

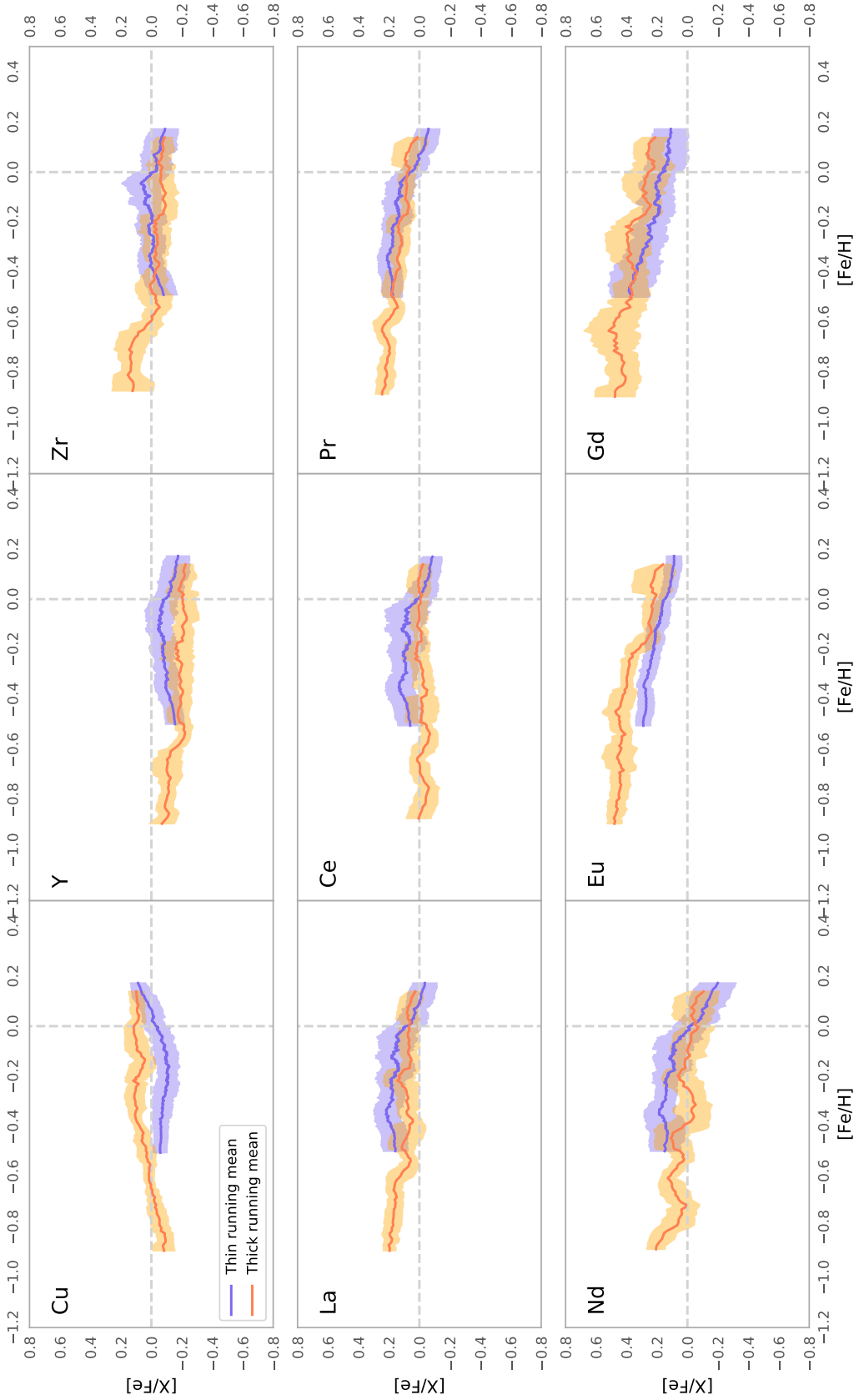


**Figure 5.2.3:** The running mean of the thin and thick disk trends as well as a  $1\sigma$  deviation. The width of the moving running mean boxes is set to be 10 % of the stellar sample.

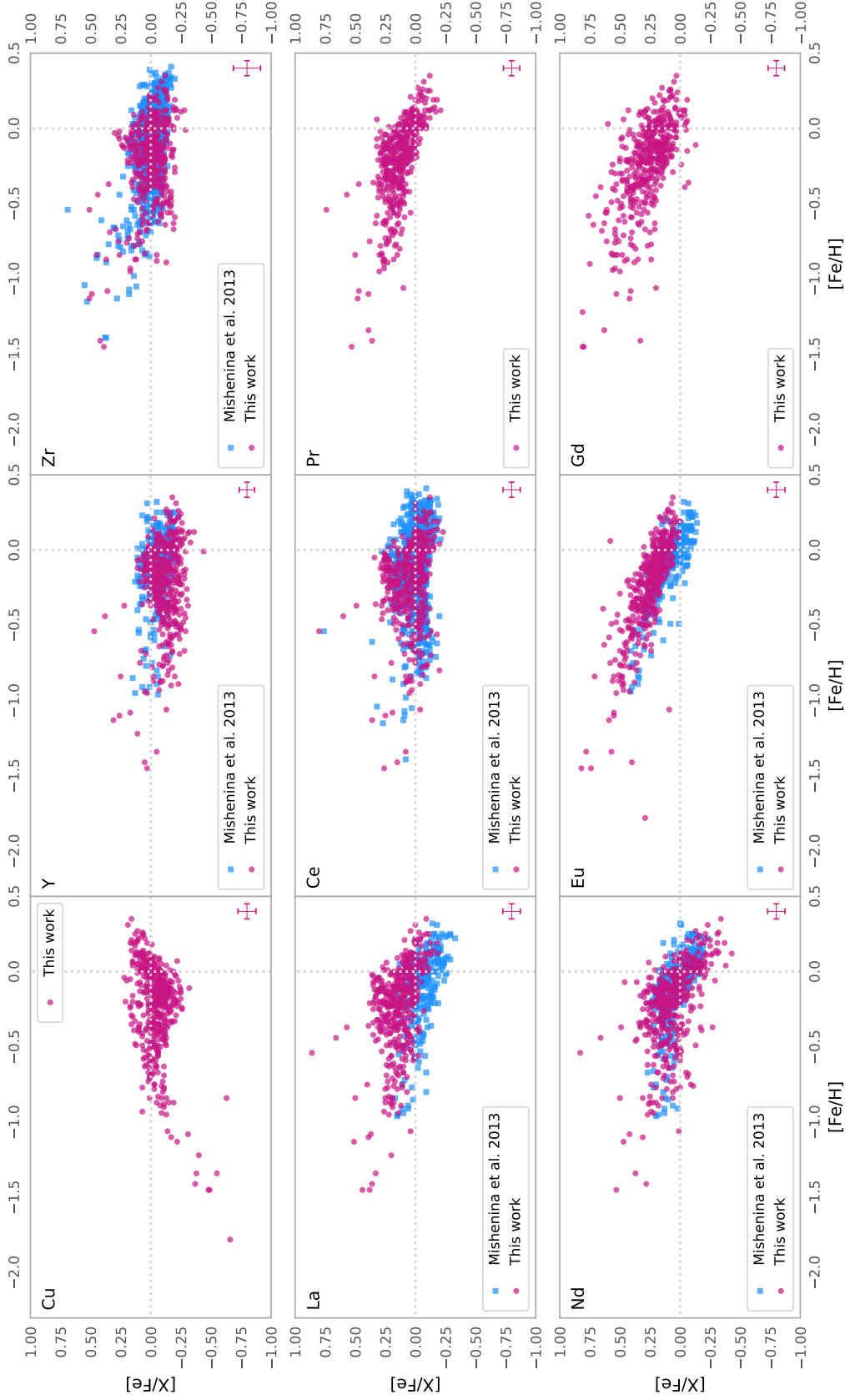


**Figure 5.2.4:** Determined abundances in this work over iron  $[X/Fe]$ , versus the metallicity  $[Fe/H]$ , compared with determined abundances in previous studies on dwarf stars by [Mishenina et al. \(2013\)](#). The typical uncertainty in this work is denoted in the lower right corner of the plots, see Section 4.5.

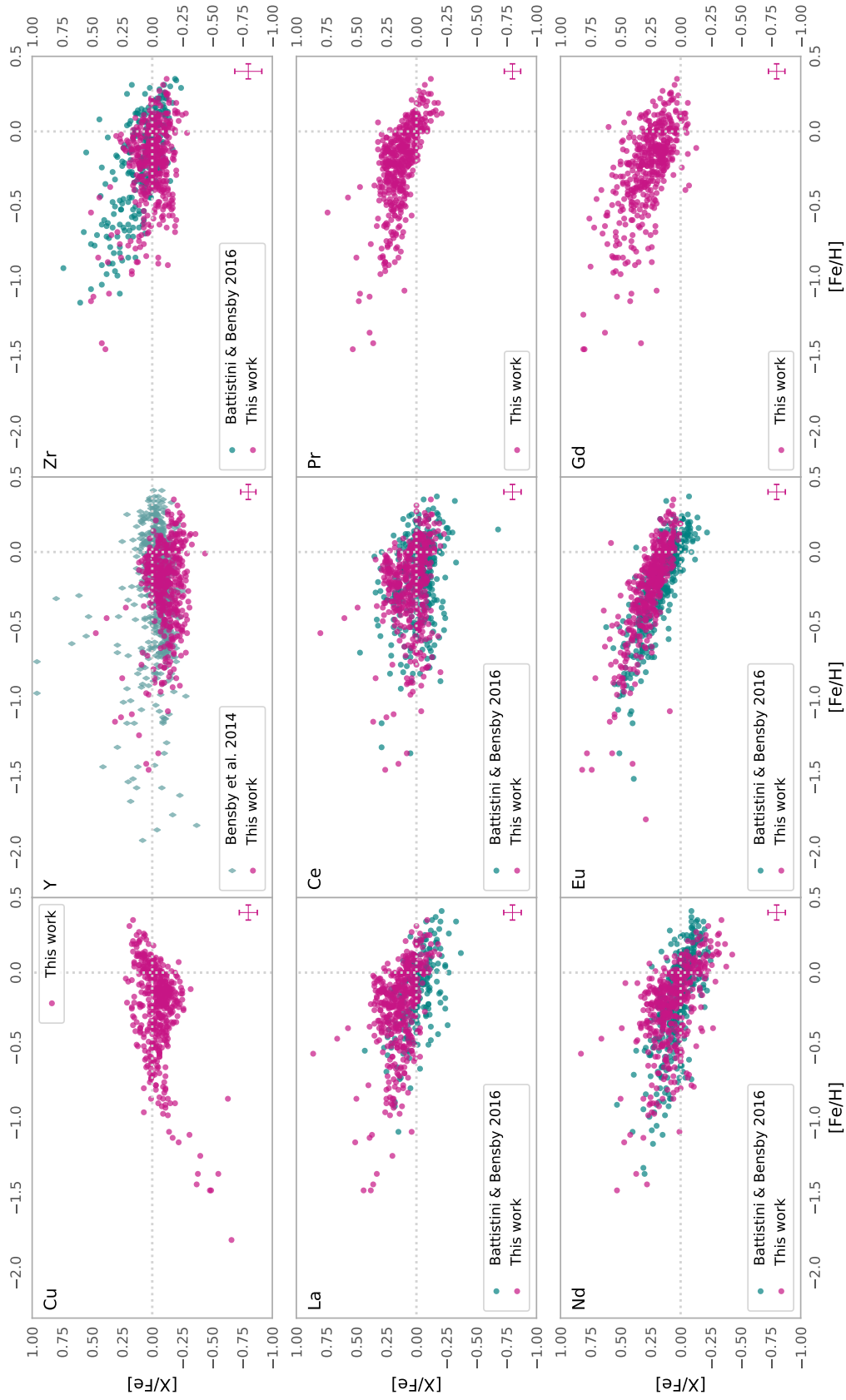


**Figure 5.2.5:** Same as 5.2.4 but with Bensby et al. (2014) (for [Y/Fe]) and Battistini & Bensby (2016) as comparison samples.



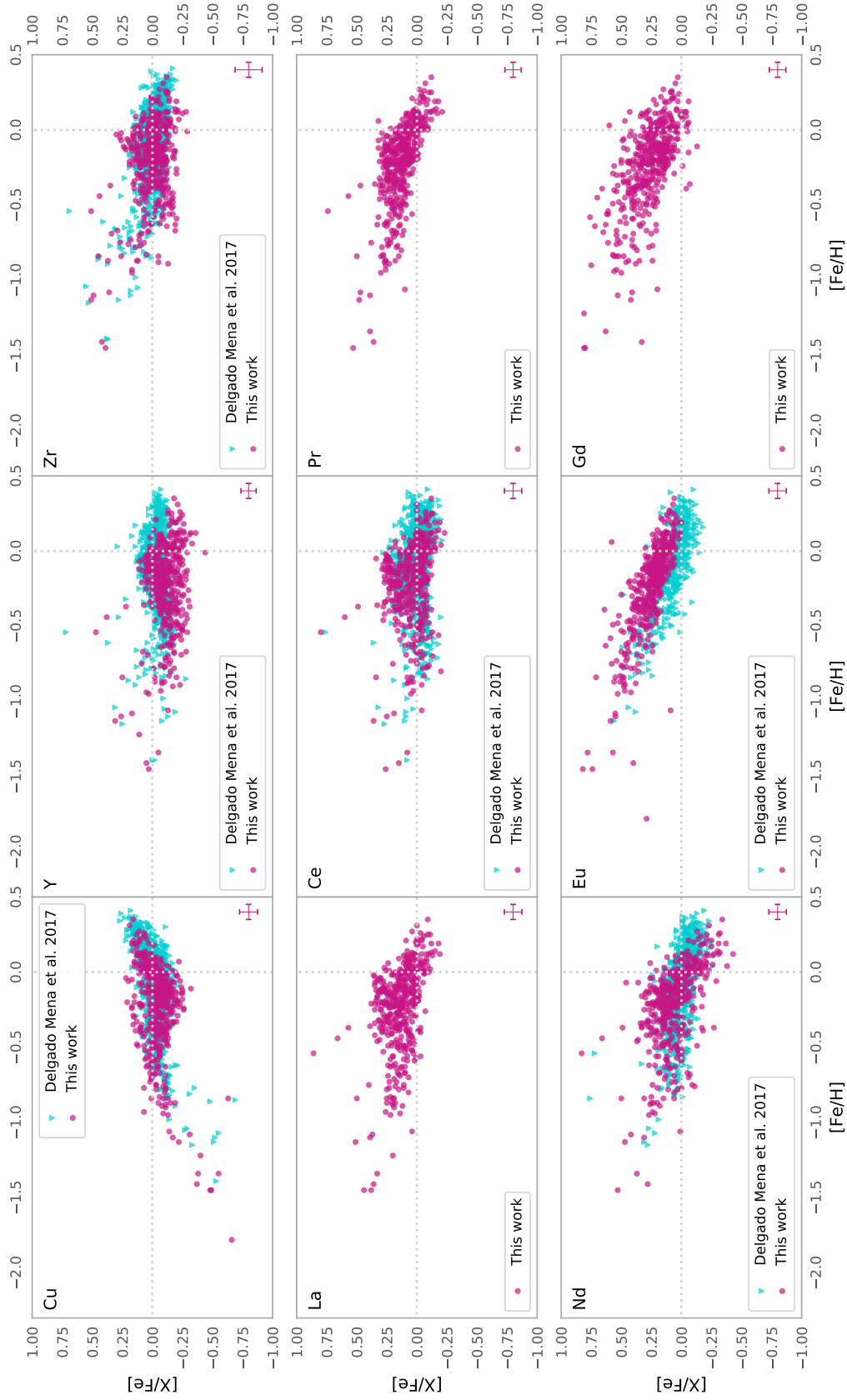
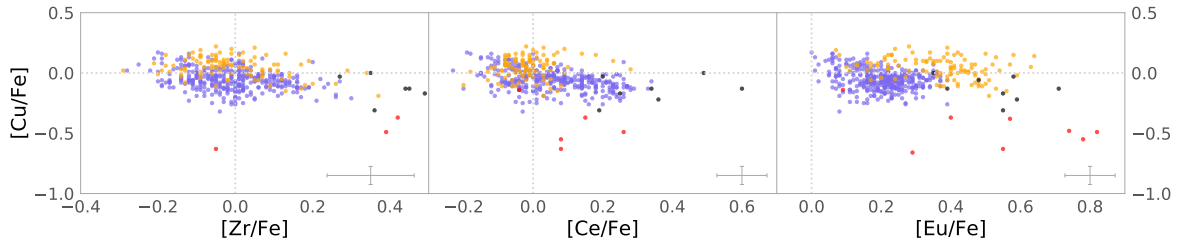


Figure 5.2.6: Same as 5.2.4 but with Delgado Mena et al. (2017) as comparison sample.

could possibly be explained by Cu acting as seed for main s-process neutron-capture elements in AGB stars. In Figure 5.2.7, I investigate whether this can be seen in the data in this work, where the  $[\text{Cu}/\text{Fe}]$  abundance is plotted against the abundances of  $[\text{Zr}/\text{Fe}]$ ,  $[\text{Ce}/\text{Fe}]$  and  $[\text{Eu}/\text{Fe}]$ . For the main s-elements there seems to be a weak anticorrelation in the thin disk, however the scatter is rather large. This indicates that Cu could work as a seed for other neutron capture elements, but since the scatter and typical uncertainty is rather large it is hard to say to what extent. These findings are similar to those in [Delgado Mena et al. \(2017\)](#).



**Figure 5.2.7:**  $[\text{Cu}/\text{Fe}]$  plotted versus the abundance of the neutron-capture elements from the different peaks. From left to right: the first s-peak element Zr, the second peak element Ce and lastly, the r-process element Eu. The typical uncertainty is indicated in the the lower right corner of every plot.

### 5.2.2 First s-process peak: Y, Zr

Y and Zr are part of the first s-process peak and are believed to be produced mainly by the main s-process in AGB stars. As seen in my results, they have rather flat abundance trends for all metallicities. The scatter is increased at metallicities of  $[\text{Fe}/\text{H}] \sim -0.3$  for the thin disk stars, reaching slightly higher abundances and indicating the onset of AGB stars producing more main s-process elements. The increase in scatter can most likely be explained by the mass range of AGB stars, which 1) enables stars to produce s-process elements at different metallicities (times) as well as 2) different amounts of production of the first/second s-process peak for different mass AGB stars. This is elaborated more in Section 5.3 where possible discrepancies between the first and second s-process peak elements are investigated.

The abundances of  $[\text{Y}/\text{Fe}]$  are slightly subsolar at solar metallicities and decrease at supersolar metallicities for both disks, which is not really observed in neither [Mishenina et al. \(2013\)](#), [Bensby et al. \(2014\)](#) nor [Delgado Mena et al. \(2017\)](#). Recall from Section 4.3.3 that the solar Y abundance determined using the same method, lines and atomic data (Section 4.3) was rather low at  $[\text{Y}/\text{Fe}] = -0.19$ , which could suggest that the yttrium abundance is possibly being systematically too low. A flattening trend could indicate main s-production from AGB stars being as efficient at producing s-process elements as SNe Ia are at producing Fe, whilst a decrease points towards iron-production being more efficient.

Zr, which has a lower contribution from main s-production than Y, 66.3 % and 71.9 %, respectively, ([Bisterzo et al. 2014](#)), has a steeper increase in thick disk stellar abundances at lower metallicities. This is observed, together with a decrease in abundances at supersolar metallicities, by [Battistini & Bensby \(2016\)](#) and [Delgado Mena et al. \(2017\)](#) as well, but

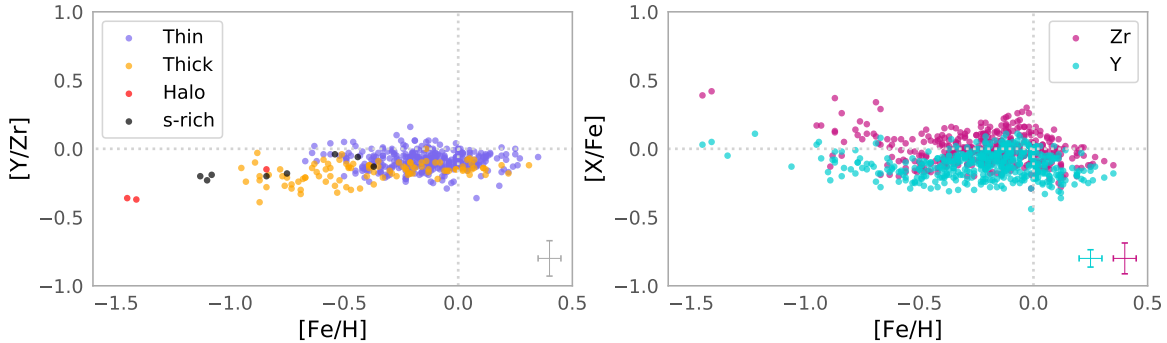


**Figure 5.2.8:** Left:  $[Y/Zr]$  plotted over  $[Fe/H]$ . Right:  $[Y/Fe]$  and  $[Zr/Fe]$  plotted over  $[Fe/H]$ , i.e same as figure 5.2.2 but instead plotted on top of each other, without the stellar population division. The typical uncertainty is indicated in the the lower right corner of both plots.

not in Mishenina et al. (2013). Considering the right plot in Figure 5.2.8 where the  $[Y/Fe]$  and  $[Zr/Fe]$  abundances are plotted versus metallicity, it becomes clear that they have very similar shapes but  $[Y/Fe]$  is systematically lower (subsolar at solar metallicities), especially at lower metallicities which can be seen in the left plot in the same figure. This could be due to systematic uncertainties or suggest different production channels for these elements; possibly the additional 5.6 % production from the r-process in Zr emerges more clearly at lower metallicities where the r-process dominates the production of heavy elements. This is further elaborated on in Section 5.3.

### 5.2.3 Second s-process peak: La, Ce, Pr, Nd

For all the main s-process elements (Y to Nd) the thin disk trend of abundances goes up at  $[Fe/H] \sim -0.3$ , creating a slight curved shape. This is most likely due to the onset of AGB stars, increasing the abundance of main s-process-dominated elements in the Galaxy. This is however only seen in the thin disk stars, pointing at different onset  $[Fe/H]$  abundances for AGB stars in the disks. This is clearest for the second s-process peak elements (La, Ce), especially for  $[Ce/Fe]$  which has the highest main s-process contribution of the elements in this work ( $> 80\%$ , Bisterzo et al. (2014)).

My result for  $[La/Fe]$  is rather similar to that of Battistini & Bensby (2016), decreasing abundances with increasing metallicities, where the decrease becomes steeper at solar metallicities, see Figure 5.2.5. However, my abundances are in general higher; theirs are solar at a metallicity of  $[Fe/H] \sim -0.5$ , whereas mine are clearly supersolar at these metallicities. The results from Mishenina et al. (2013) are slightly subsolar in comparison to both mine and the Battistini & Bensby (2016) results throughout all metallicities, however they only extend down to  $[Fe/H] \sim -1.0$  (similar as Battistini & Bensby (2016)), leaving the question of an increasing or a flat trend at lower metallicities uncertain. Additionally, the increase of abundances at  $[Fe/H] \sim -0.3$  can not be seen in either Mishenina et al. (2013) or Battistini & Bensby (2016).

Ce, with a main s-process production of  $> 80\%$ , has a somewhat flatter  $[\text{Ce}/\text{Fe}]$  trend than the other second s-process peak element (see Table 2.1 for production contributions) at all metallicities. However, it is not tracing out a flat solar trend completely, instead, the trend of the thin disk has a banana shape, going from lower abundances to higher, and then lower again, with increasing metallicity. Above solar metallicities the abundances of Ce decreases in the thin disk, whilst staying flat in the thick disk. The decrease is however not as steep as for La (or Pr and Nd) which have higher contributions from the r-process. In general, my results agree well with previous results by Delgado Mena et al. (2017) whereas Battistini & Bensby (2016) have a larger scatter, not showing a higher abundance at  $[\text{Fe}/\text{H}] \sim -0.3$ , and Mishenina et al. (2013) have solar abundances for low metallicities.

$[\text{Pr}/\text{Fe}]$  and  $[\text{Nd}/\text{Fe}]$  show similar trends, with 49.9 % and 57.5 % production from the main s-process, respectively.  $[\text{Pr}/\text{Fe}]$ , with a tighter trend than  $[\text{Nd}/\text{Fe}]$ , does not decrease as rapidly with increasing metallicity as  $[\text{Nd}/\text{Fe}]$ . Additionally, the increase in abundance at  $[\text{Fe}/\text{H}] \sim -0.3$  is not as prominent, compared to the other main s-process dominated elements. This is due to a higher contribution from the r-process (50.1 %), whereas Nd has a stronger contribution from the main s-process in the trend. There have only been small scale abundance determinations of Pr in previous works leaving this element without a comparison sample. As for Nd, the trend in general is similar to that of Mishenina et al. (2013); Battistini & Bensby (2016); Delgado Mena et al. (2017), however, above solar metallicities, both the trends from Battistini & Bensby (2016) and Delgado Mena et al. (2017) seem to flatten out, which is neither the case for my trend nor that of Mishenina et al. (2013).

#### 5.2.4 r-process: Eu, Gd

As mentioned previously in this work, the production site for the r-process elements is not yet constrained to one or several specific sites, but have several possibilities. The r-process requires a high neutron density, pointing at explosive and/or "transient" events, such as SNe II and/or neutron star mergers as the most probable production sites.

The  $[\text{Eu}/\text{Fe}]$  trend with metallicity is constantly declining towards higher metallicities, with a possible flattening at low,  $[\text{Fe}/\text{H}] < -1.0$ , metallicities. Eu has a calculated 94 % production from the r-process. Gd has a 84.6 % production from the r-process and the  $[\text{Gd}/\text{Fe}]$  trend with metallicity is very similar to that of  $[\text{Eu}/\text{Fe}]$ . The constant declining trend with metallicity for these two elements indicates that the r-process has a continuous enrichment in the Galaxy, similar to that of the  $\alpha$ -elements. The  $[\text{Eu}/\text{Fe}]$  trend is tighter than that of  $[\text{Gd}/\text{Fe}]$ , however both of them are supersolar at solar metallicities. Both Battistini & Bensby (2016) and Guiglion et al. (2018) show supersolar abundances at solar metallicities for Eu, which is not seen in Delgado Mena et al. (2017). This could point at the Sun being deficient in r-process elements, compared to solar neighborhood stars. However, due to the discrepancies between data samples, more data is needed for such conclusions to be drawn.

It is rather difficult to compare my results for Gd with previous work since these are sparse. The first trend with a large sample was published last year by the AMBRE project (Guiglion et al. 2018), using primarily dwarf stars from the ESO-archive (high-resolution FEROS, HARPS, and UVES spectra). However, it should be noted that they use industrially-determined parameters and abundances from an automatic pipeline, GAUGUIN (Guiglion

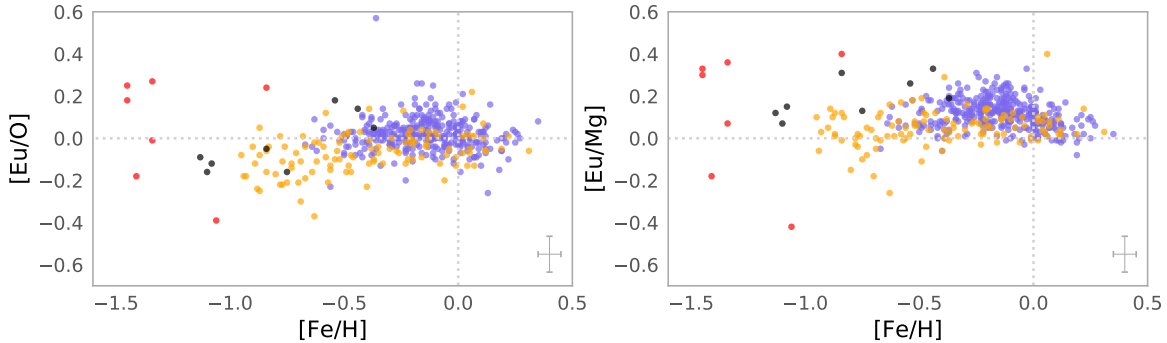


**Figure 5.2.9:**  $[\text{Eu}/\alpha]$  plotted against  $[\text{Fe}/\text{H}]$  for the stellar populations, colours the same as for previous plots, for instance 5.2.1. Left:  $[\text{Eu}/\text{O}]$ . Right:  $[\text{Eu}/\text{Mg}]$ . The typical uncertainty is indicated in the lower right corner of both plots.

et al. 2016), which might not be as accurate as the work done here or the other comparison samples. For their results, see Figure 5 in Guiglion et al. (2018).

In general, the thick disk has higher abundances in  $[\text{Eu}/\text{Fe}]$  than that of the thin disk, which is similar to the trends seen in  $\alpha$ -elements. This is also observed in Delgado Mena et al. (2017) and Guiglion et al. (2018). The separation however is not as clear for  $[\text{Gd}/\text{Fe}]$  due to the larger scatter. Given the assumption that r-process elements are created in a process with a rather continuous enrichment in the Galaxy (such as massive stars), the decrease in abundances,  $[r/\text{Fe}]$ , is given after SNe Ia start enriching the disks. Due to the, in general, older ages of thick disk stars, this would explain why they have higher  $[\text{Eu}/\text{Fe}]$  values on average, than the thin disk stars. In general, the higher the r-process contribution an element has, the higher are the thick disk abundances. However, it is worthwhile to keep in mind that the separation is done using high- and low- $\alpha$  abundances (same for the comparison samples), which might affect the results.

Considering the right plot in Figure 5.2.9, where  $[\text{Eu}/\text{Mg}]$  is plotted versus the metallicity, the mostly flat trend points at Eu possibly having a non-negligible contribution from progenitors of similar timescales as that of progenitors producing Mg. At  $[\text{Fe}/\text{H}] \sim -0.3$  the production of Eu in AGB stars (6 %) emerges in the thin disk. It has been shown by Travaglio et al. (1999) that SNe progenitors with masses of 8-10  $M_{\odot}$  best reproduce the r-process enrichment in the Galaxy. Additionally, they also showed that more massive SNe progenitors, of  $> 15 M_{\odot}$ , contributed to the oxygen production in the Galaxy at earlier times (since 15  $M_{\odot}$  stars evolve faster than 8-10  $M_{\odot}$ ). Therefore, the production of magnesium would have a later onset in the Galaxy, compared to oxygen, producing higher  $[\text{O}/\text{Mg}]$  values at lower metallicities. In the left-hand plot of Figure 5.2.9 the  $[\text{Eu}/\text{O}]$  is therefore plotted, showing a somewhat decreasing trend with decreasing metallicity in the thick disk, but not very distinct.

To conclude from these comparisons, the analyses and abundances determined in this work show very similar results to that of the work previously done on dwarf stars, and can be judged to be as reliable and accurate.

### 5.3 Comparison of the neutron-capture elements

One way to understand and disentangle the contributions of the s- and r-process in the production of heavier elements is to compare the abundances with each other. An extension of this is to compare with other, perhaps more known elements, such as the  $\alpha$  elements.

It is common to use barium (Ba) as a 'pure' s-process element to compare other heavy elements with. However, Ba is not analysed in this work, instead, Ce will be used for this comparative discussion since it is the neutron-capture element in this work with the highest contribution from the main s-process of 83.5 %, see Table 2.1. This is comparable to Ba which has an 85.2 % production from the main s-process (Bisterzo et al. 2014). On the contrary, Eu is created primarily in the r-process, 94.0 %. Given this, cerium and europium are excellent for comparison to other neutron-capture elements, where the production sites, or the contribution from the different processes, are not as certain.

Firstly, the [Eu/Ce] abundance is plotted against the metallicity, Figure 5.3.1. In this plot, a so-called pure r-process line is added, using the values from Bisterzo et al. (2014), in their Table 1. The value of the pure r-process line is calculated by subtracting the predicted s-process abundance from the Solar System total values or, in other words, treating the r-process as a residual, the same as for Table 2.1. Therefore, the pure r-process line is the value of the r-process contribution in both elements, such that  $[\text{r-process}(\text{Eu})/\text{r-process}(\text{Ce})]$ . A flat trend in this plot indicates a similar production rate of the elements, whereas a decrease/increase indicates discrepancies.

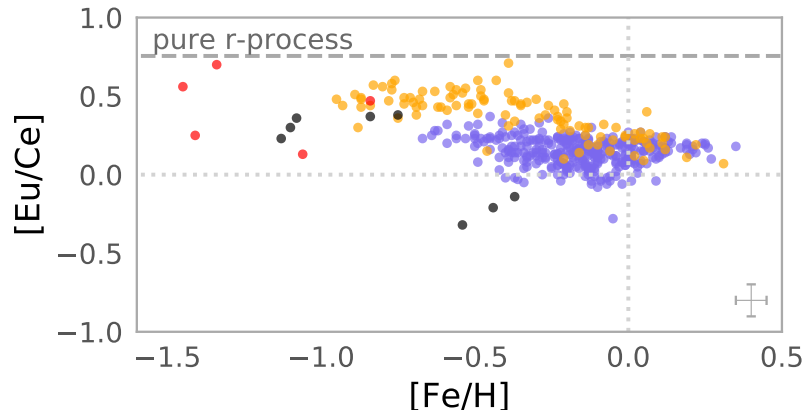


**Figure 5.3.1:** [Eu/Ce] plotted against [Fe/H] for the stellar populations. As seen in Table 2.1, Eu has a 94.0 % contribution from the r-process, whereas Ce is only 16.5 %. The colours are the same as previously, see Figure 5.2.1. The pure r-process line is derived using values from Bisterzo et al. (2014). The typical uncertainty is indicated in the the lower right corner of the plot.

From Figure 5.3.1 it becomes clear that the r-process dominates the production of neutron-capture elements at lower metallicities, also producing the s-process dominated elements, like Ce. This points at r-process occurring on fast time scales, whereas AGB stars, originating from low to intermediate mass stars, have a time delay in the Galaxy. As AGB stars start to

enrich the ISM, the Ce abundance increases, and [Eu/Ce] ratio decreases.

Using the knowledge from plot 5.3.1, the abundance ratios of Y, Zr, La, Pr, Nd and Gd with Ce and Eu are plotted against the metallicity in Figure 5.3.2. In the first column the [X/Ce] abundance is plotted, where a steeper slope points at an element with more production from the r-process, see for instance [Pr/Ce] and [Gd/Ce]. This is most likely explained by the production of Ce in AGB stars at sub-solar metallicities, increasing the Ce-abundance whilst r-process elements also are produced to a greater, relative, extent at lower metallicities, creating the decreasing trend. In comparison, the [La/Ce] abundance is nearly flat, indicating that these have a very similar production history. In these plots it also becomes clear that Nd and Gd only have one spectral line in the abundance determination, making the results for these elements more scattered.

Interestingly, the trends of the first s-peak elements, [Y/Ce] and [Zr/Ce], do not trace a completely flat trend, except at solar metallicities. Compared to the [Eu/Ce] abundance, [Zr/Ce] has a less steep increase for lower metallicities, most likely due to the higher s-process component in Zr compared with Eu. However, the abundances for the thick disk stars at lower metallicities are very high and close to the r-process line, which might be difficult to explain with the given r-process contribution to these elements and could point at a different production channel between the first and second s-peak elements at lower metallicities. This strengthens the idea of a Light Element Primary Production (LEPP) mechanism as proposed in Travaglio et al. (2004). Similar findings are observed, and similar conclusions are drawn, in Battistini & Bensby (2016).

In the second column the [X/Eu] abundance is plotted instead in order to get the r-process contribution for the elements. Similarly as for the first column, a flat trend indicates similar production of the elements, whereas a decrease/increase indicates a dissimilar production. For instance, the almost 25 % of r-process production in La becomes more clear here than in the [La/Ce]-plot, since La is compared to an r-process element instead that is more 'pure' than Ce. [Gd/Eu] shows a flat, though scattered, trend suggesting similar production channels. This differs somewhat from the findings in Guiglion et al. (2018) where they found somewhat decreasing [Gd/Eu]-trend, especially at supersolar metallicities, pointing at different production channels for the two elements.

### First- and second s-process peak elements

In Figure 5.3.3 the ratio of the second peak s-elements (for these I use a mean of the La, Ce, Nd-abundances), and the first peak (Zr)<sup>1</sup> elements are plotted versus the metallicity.

From findings by Bisterzo et al. (2017), the importance that the size of the <sup>13</sup>C-pocket has to the s-process production is shown. The neutrons in the AGB stars come from the reaction in eq. (2.1), where the amount of <sup>13</sup>C sets the amount of neutrons. In the third dredge up, first peak elements are created first and as the neutron exposure increases, the second peak elements are also created. In more massive AGB stars, > 4 M<sub>⊙</sub>, the second reaction, eq. (2.3), takes place due to higher temperatures and higher amounts of primary <sup>22</sup>Ne. This

<sup>1</sup>Because of the much lower abundances of Y in Figure 5.2.8 which can not be excluded from being due to systematic uncertainties, I have chosen to include only Zr in this plot, which also matches the findings from Delgado Mena et al. (2017). Using a mean of Y+Zr gives similar, although higher, results.

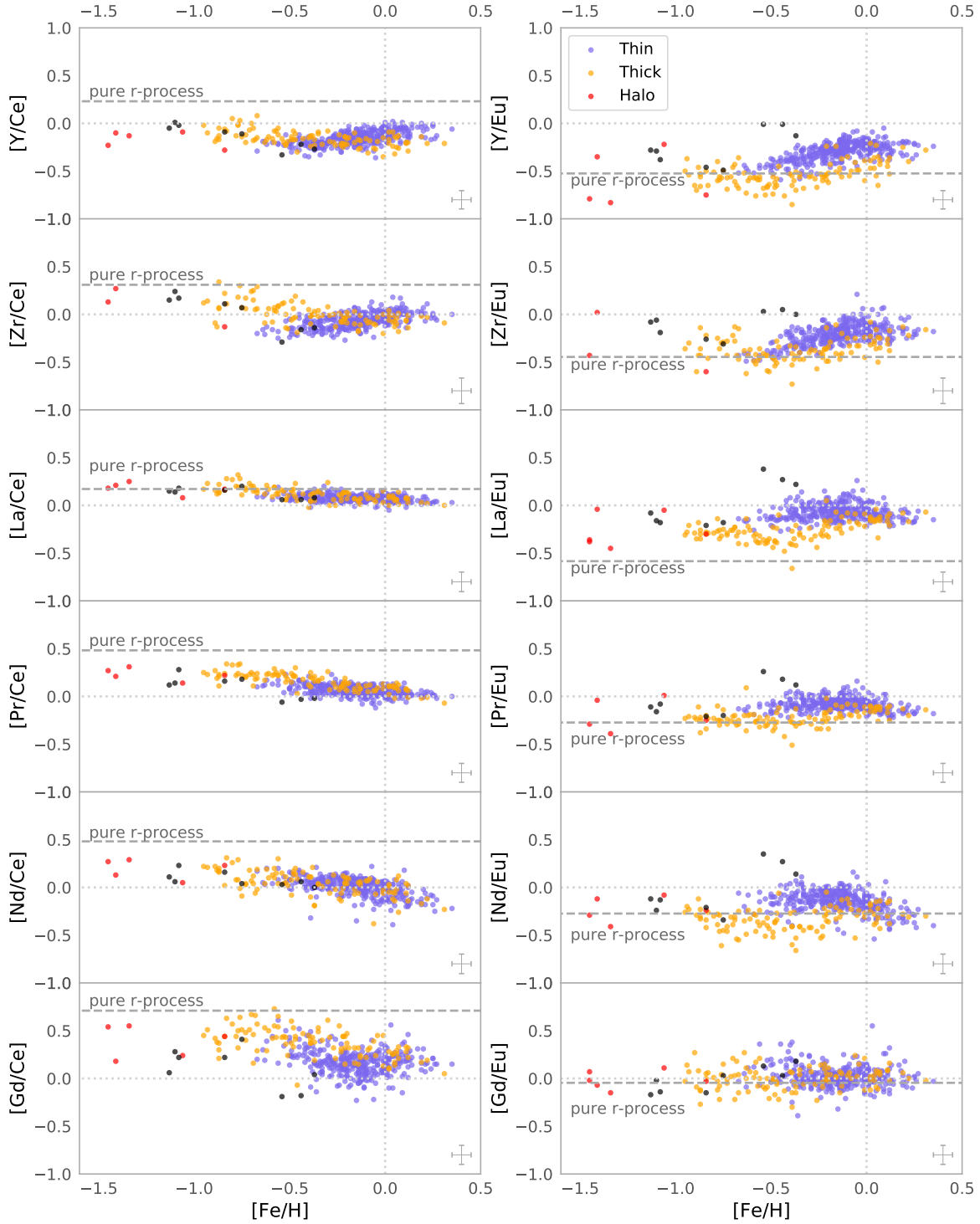


**Figure 5.3.2:**  $[X/Ce]$  (left column) and  $[X/Eu]$  (right column) plotted against the metallicity for  $X = Y, Zr, La, Pr, Nd, Gd$  (starting from top row to bottom). The pure r-process line is plotted in the  $[X/Ce]$ -plots just as in Figure 5.3.1, derived using values from [Bisterzo et al. \(2014\)](#). The typical uncertainty is indicated in the the lower right corner of every plot.



increases the neutron density, in addition to shrinking the  $^{13}\text{C}$ -pocket. Moreover, the neutron exposure of the reaction  $^{22}\text{Ne}$  is lower than that of  $^{13}\text{C}$ , resulting in a smaller quantity of s-elements to be expected, especially the heavier ones. Therefore, one could draw the conclusion that heavier AGB stars produce relatively fewer second peak elements than low-mass AGB stars.

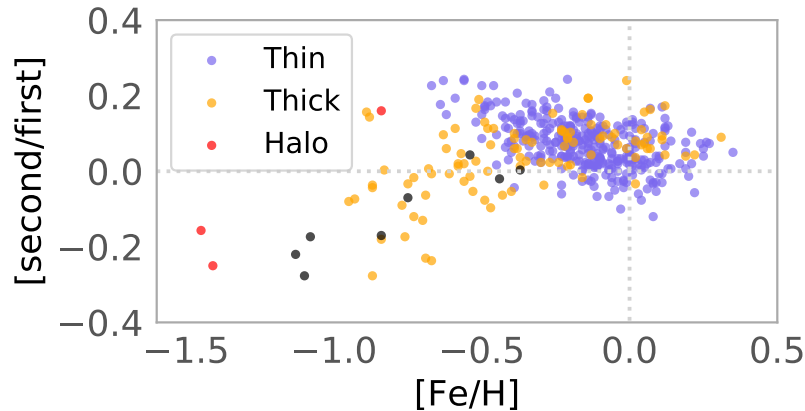


**Figure 5.3.3:** The ratio of the second peak- (La, Ce, Nd) and the first peak (Zr) elements are plotted towards the metallicity for the stellar populations. Colours are as in previous plots, see eg. 5.2.1.

Below solar metallicities, the thin disk stars show an enrichment of second peak as compared to first peak elements (Figure 5.3.3). This can be explained by the stellar yields from [Karakas & Lugaro \(2016\)](#) and previous discussion, where low-mass AGB stars have a higher relative production of second peak elements compared to first peak element. Therefore, assuming an IMF with more low mass stars than higher mass stars, the amount of low-mass AGB stars have produced an overabundance of heavy s-elements in the thin disk. It can also be explained by considering the number of neutrons to the available  $^{56}\text{Fe}$ -seeds: at lower metallicities, the higher neutron density (compared with that of  $^{56}\text{Fe}$ -seeds) enables the build up of second peak elements ([Busso et al. 1999](#)). Consequently, at higher metallicities, the relative neutron density goes down and first peak element abundance increases to that of the second peak abundance.

For the thick disk, the trend is quite the opposite with larger amounts of first peak to second peak at low metallicities. This is again explained by the low-mass AGB stars which has not yet enriched the ISM at the time of the formation of the older thick disk stars, resulting in low [second-s/first-s] abundances. However, this points at (low-mass) AGB stars not being the only important contributor to s-element production in the thick disk, where the first peak elements must be produced elsewhere, such as LEPP ([Travaglio et al. 2004](#)). However, by including weak-s production from fast-rotating metal-poor stars, the abundance of the first peak elements can be increased ([Frischknecht et al. 2012, 2016](#)).

At supersolar metallicities, the first peak elements seem to increase in both disks. This could be explained by the contribution of metal-rich AGB stars, producing a higher amount of first peak elements ([Karakas & Lugaro 2016](#)).

## 5.4 s-process enhanced stars

Due to the high accuracy results presented in this work, it is possible to pick out individual, *peculiar* stars from the abundance trends. In Figure 5.2.2 it is clear that some stars are enriched in s-process elements, namely the elements with a dominating production from AGB stars (main s-process): Y, La, Zr, Ce, Pr and Nd. These stars are marked with black in all plots. These stars do not show any enrichment in either  $\alpha$ -elements (Figure 4.4.1) or the weak s-process-dominated element Cu. Additionally, a rather r-process-enriched star that stands out most in [Eu/Fe], but also for [Pr,Nd,Gd/Fe], can be seen at [Fe/H]  $\sim$  0.1.

Even though the stars do not stand out in the  $\alpha$ -elements, the enriched stars have a small enrichment seen in the r-process-dominated elements Eu and Gd too, however it is not as clear as for the s-process elements. The enrichment is still present when the abundance with the respect to magnesium is considered, Figure C.0.2, where it also is more prominent that the iron- and magnesium poor(er) stars belong to the thick disk/halo and the iron and magnesium richer stars are thin disk stars.

The explanation of the enrichment of these stars is not trivial. The stars in the stellar sample are chosen, and determined in the stellar parameter determination to be on the red giant branch and not AGB stars, meaning that the enrichment in the photosphere is not directly produced in the star itself. One possible explanation is that the star is a stellar companion to a former AGB star; as an AGB star blows away its envelope, a stellar companion can accrete the said envelope and obtain an enriched photosphere.

The names and metallicities of the s-enriched stars can be seen in Table 5.2. All 8 s-rich stars are observed within the APOGEE survey (Majewski et al. 2017). 4 of these stars have been observed more than once by APOGEE and hence a radial velocity scatter is provided. If the velocity scatter is large it would point at a multi-system, however the velocity scatters are rather small, leaving the explanation of the s-enriched stars unknown.

**Table 5.2:** The names, metallicities and velocity scatter of the measured s-enriched stars in the stellar sample.

2MASS name	[Fe/H] [dex]	Velocity scatter [km/s]
J17215666+4301408	-1.13	0.27
J18523459+4046480	-1.10	-
J16113361+2436523	-1.08	0.07
J14231899+0540079	-0.84	0.01
J15160507+4322192	-0.75	-
J12051252+0843587	-0.54	0.04
J19435663+4947000	-0.44	-
J19175551+4946243	-0.37	-

## 5.5 Age estimation using $[Y/Mg]$

Since a non-negligible number of stars in my stellar sample is found in the Kepler field, the catalogue from [Pinsonneault et al. \(2018\)](#) can be used to find age estimates for some of my stars. These ages are calculated using asteroseismologic data in combination with APOGEE DR14 stellar parameters ([Holtzman et al. 2018](#); [Jönsson et al. 2018](#)). The oscillation frequencies of stars are closely related to the properties of the stellar interior properties, through the sound speed which is related to the density. Since these properties are linked to the mass and evolutionary state, ages and masses can be determined for a star by comparing the oscillation spectrum with predictions of stellar evolution models. Ages for 62 of the Kepler stars in my stellar sample are available in [Pinsonneault et al. \(2018\)](#).

$[Y/Mg]$  has been shown by [Nissen \(2016\)](#) to work as an age estimator in solar twins. Following that discovery, [Slumstrup et al. \(2017\)](#) found the age estimator to hold for evolved, solar metallicity stars too, using measurements on four open clusters with close to solar metallicities. Additionally, in previous work by [Titarenko et al. \(2019\)](#) they found the relation to hold for turn-off sub-giant stars. These findings, together with the work presented here, increases the possibilities to 1) estimate the age of giant stars, which is difficult (elaborated on in [Section 4.4](#)), and 2) estimate the ages of stars found far outside the solar neighbourhood, since giant stars can be observed at larger distances.

The way  $[Y/Mg]$  can be used as an age estimator is explained by the increase of  $[Mg/Fe]$  with stellar age, due to enrichment by SNe II for Mg compared with that of SNe Ia for Fe. On the other hand,  $[Y/Fe]$  has been observed to decrease with increasing stellar age, due to AGB stars not yet being important for the production of yttrium at early times. The slope of  $[Y/Fe]$  is therefore steep as a function of age, which is the opposite to that of  $[Mg/Fe]$ . In [Feltzing et al. \(2017\)](#) they found that the decreasing trend indeed holds, but disappears at  $[Fe/H] \lesssim -0.5$  where the trend is flat and has no dependence on age.

In [Nissen \(2016\)](#) the following relationship with age for solar twins was found,

$$[Y/Mg] = 0.170(\pm 0.009) - 0.0371(\pm 0.0013) \cdot \text{Age [Gyr]}. \quad (5.1)$$

I also investigated that relation, see [Figure 5.5.1](#). Similar to [Feltzing et al. \(2017\)](#) and [Slumstrup et al. \(2017\)](#), I find that the relation indeed holds for evolved stars at solar metallicities and that the relation does not hold for low-metallicity stars. By including stars of metallicities  $-0.3 < [Fe/H] < 0.3$ , I get the following relation for  $[Y/Mg]$  with age

$$[Y/Mg] = -0.070 - 0.0372 \cdot \text{Age [Gyr]} \quad (5.2)$$

which has a very similar slope to that of [Nissen \(2016\)](#) but is systematically lower.

Additionally, I look at the trend with  $[Zr/Mg]$  over age, since it should produce similar results to that of  $[Y/Mg]$ , seen in the lower row of [Figure 5.5.1](#). The  $[Zr/Mg]$  is, as expected, higher than the  $[Y/Fe]$  ratio, producing a trend with a fit of

$$[Y/Mg] = -0.002 - 0.0314 \cdot \text{Age [Gyr]} \quad (5.3)$$

for  $-0.3 < [\text{Fe}/\text{H}] < 0.3$  metallicities. I would conclude that there is a relationship but I am cautious to use this method due to the uncertainties in the determined ages, which has not been determined by me.

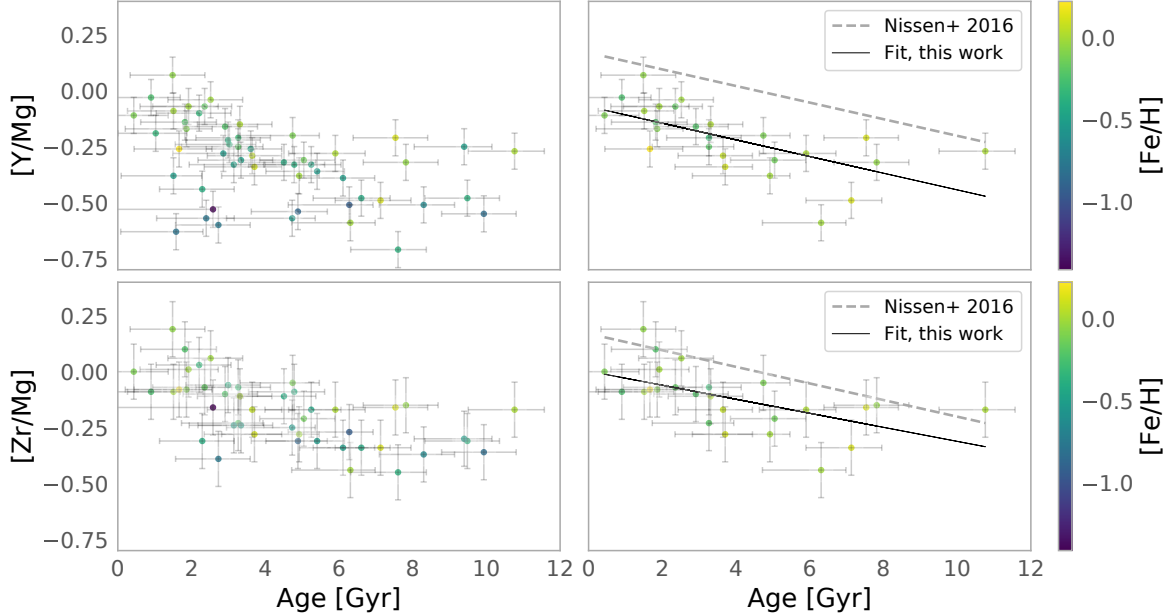


**Figure 5.5.1:**  $[\text{X}/\text{Mg}]$  abundance plotted against the estimated stellar ages, with age uncertainties determined in [Pinsonneault et al. \(2018\)](#). The points are colour coded with  $[\text{Fe}/\text{H}]$ , as indicated in the colourbar to the right. The left plots include all available stars whilst the right plot shows only metallicities  $-0.3 < [\text{Fe}/\text{H}] < 0.3$ . The linear fit to the data is plotted (black, solid line) as well as the fit measured in [Nissen \(2016\)](#) (grey, dashed). The uppermost plots show  $[\text{Y}/\text{Mg}]$  whilst the lower shows  $[\text{Zr}/\text{Mg}]$ .

## 5.6 Additional elements

In this section I will briefly note why it was not possible to make abundance determinations of Zn, Sr, Nb, Mo, Ru, Ba, Sm and Dy, also investigated in this project.

**Zinc:** For Zn there were only five possible lines. All of these are very blended, and the most promising one is blended with the auto-ionising calcium (Ca) line at  $6361.74 \text{ \AA}$ . The trend was heavily scattered and is therefore not included in the analysis of this project.

**Strontium:** For Sr there were 11 possible lines. Only one line seemed possible to use. However it turned out to unfortunately be blended with molecular lines that are both temperature dependent and are not modelled well, which causes a large scatter in the abundances.

**Niobium:** For Nb there were 20 possible lines. Several of these are very blended in the giant stars spectra, or are too weak to be usable. Only one line was not too weak nor too blended, but had inaccurate atomic data, resulting in an overestimated abundance.

**Molybdenum:** For Mo there were 23 possible lines. Several of these are very blended in the spectra, or are too weak to be usable. Three lines were not too weak nor too blended, but had inaccurate atomic data, resulting in too scattered and over-/underestimated abundances.

**Ruthenium:** For Ru there were 20 possible lines, several of these are very blended in the spectra, or are too weak to be usable. Three lines were not too weak nor too blended, whereas one of these had no close-by continuum points. Additionally, these three lines had inaccurate atomic data, resulting in too scattered and over-/underestimated abundances.

**Barium:** For Ba there were 11 possible lines. In the spectra, several of these lines are too blended to be modelled properly. Additionally, several of these gave overestimated abundances, pointing at underestimated  $\log gf$  values. Only one line resulted in a not too scattered, tight trend. However, this is a very strong line which is saturated in many stars and thus dependent on the microturbulence. The [Ba/Fe] trend with metallicity was systematically supersolar, and was therefore not used in the analysis.

**Samarium:** For Sm there were 60 possible lines. Several of these are very blended in the giant stars spectra, or are too weak to be usable. The lines without, or with few, blends had inaccurate atomic data, resulting in too scattered and over-/underestimated abundances.

**Dysprosium:** For Dy there were 7 possible lines. All of these are very blended in the giant stars spectra, except for one which is too weak to be usable.

# Chapter 6

## Conclusions

The aim of this work has been to put observational constraints on the Galactic chemical evolution of neutron-capture elements and provide a reference sample of giant stars by identifying and minimising possible systematic uncertainties when working with giant stars.

In this work the abundances of 9 neutron-capture elements have been determined in a local disk sample of 523 giant stars. The stars are relatively homogeneously spread in the solar neighbourhood, with a majority of the stars within 1.5 kpc distance from the Sun. The spectra of the giant stars were obtained using the high resolution spectrograph FIES at the Nordic Optical Telescope, La Palma. The careful analysis of the high resolution spectra by synthesising spectra in SME resulted in high quality abundances, comparable with previous work done using dwarf stars.

Thanks to the high resolution spectra, both isotopic shift and hyperfine splitting have been taken into account (when these have been available for the atomic data) when producing the synthetic spectra. A grid of spherically symmetric, 1D hydrostatic, LTE MARCS model atmospheres has been used. NLTE corrections have not been applied to the LTE abundances since these are not available for giant stars for the elements in this work. The calculation of possible NLTE corrections lies outside the scope of this work.

The stars in the sample have been divided into stellar populations based on their  $\alpha$ -abundance and to some extent their kinematics, referred to as thin and thick disk. In general I find that the thin disk stars are enriched in s-process elements, whilst the thick disk stars are enriched in r-process elements. This is similar to previous findings in, for example, [Battistini & Bensby \(2016\)](#) and [Delgado Mena et al. \(2017\)](#). I find that the weak s-process-dominated element copper has a metallicity-dependent yield which matches the theory for this process. The time delay of AGB stars becomes very clear in the s-process-dominated elements by an increase in the  $[s/Fe]$  abundance kicking in at  $[Fe/H] \sim -0.3$ . I find some discrepancies between the first and the second s-process peak trends with metallicity, indicating different production channels. This is most prominent at low metallicity, supporting the findings in [Travaglio et al. \(2004\)](#) of a Light Element Primary Production.

The trend with metallicity of the r-process-dominated elements Eu and Gd resembles that of  $\alpha$ -elements. In the abundance trends it becomes clear that this trend is stronger the higher the contribution from the r-process is in producing the elements. I can not put a constraint

on the precise production site for the r-process elements, but I can say that 1) it does not have a time delay in the Galaxy, such as, for example, AGB stars or SNe Ia would require and 2) it is constant with metallicity and 3) therefore must have high stellar mass progenitors.

For the first time, abundances of Pr have been presented for a large stellar sample. I found 3 Pr spectral lines in the optical wavelength regime which all produce similar abundances in giant stars, which increases the precision of the measured abundances. Additionally, abundances for Gd for a large stellar sample are presented for the second time, where the first can be found in [Guiglion et al. \(2018\)](#). Pr has a 50/50 s-/r-process production whilst Gd is an r-process element, which can be used by Galactic chemical evolution modellers to better constrain the evolution of the Galaxy, and the production of these elements.

I find 8 s-process element enriched stars in the stellar sample, whose enrichment is yet to be explained. This is an indication of the high quality abundances in this work, since it allows outliers in the data to be found, in addition to tracing the disk populations. With this, I conclude that the aims of the work have been met and the results produced can be used in future work within abundance determination and Galactic archaeology.

## 6.1 Future outlook

To complement, or continue, this work there are several things one can consider. Firstly, a comparison of the abundances determined in this work with those of theoretical Galactic chemical evolution models should be made. The accuracy in the presented work would allow such models to be constrained, which is important to be able to understand both the evolution of the Galaxy and the formation of its components, as well as the processes that take part in producing specific elements. I have been in contact with Dr. Chiaki Kobayashi (see for instance [Kobayashi et al. \(2006\)](#)) after conversations at the *Chemical Evolution and Nucleosynthesis Across the Galaxy*, conference (see Appendix D) who is very interested in comparing her chemical models with my work.

As an extension to this, it would be of great benefit to actually fulfill what this work has laid the foundation for: to probe deeper. The Nordic Optical Telescope with its 2.5 meter mirror has let us observe the solar neighbourhood. By using a telescope with a larger mirror and a high resolution spectrograph, both the inner and other parts of the disk could be measured and analysed. Since my results show quite clear discrepancies between the thin and the thick disk (the chemical separation, that is) the neutron-capture elements could be used to understand the disk population(s) better.

Some suggestions for telescopes that could be used for this is the Gran Telescopio Canarias (10.4 meter) which has the instrument HORus (The High Optical Resolution Spectrograph), in optical high resolution spectrograph covering the visible wavelength range with a spectral resolution of  $R \sim 25000$ . But that resolution is significantly lower than that of the present work. The HIRES spectrograph with a resolution between 25,000 and 85,000 (at the Keck telescope, 8.1 meter) might be more appropriate. Additionally, for the northern hemisphere, the Pepsi instrument ( $R$  up to 270 000) mounted at the Large Binocular Telescope could also be appropriate.

For observations of the inner disk and the bulge/bar, a telescope located in the southern hemisphere would be best, and for this the Very Large Telescope (VLT) with UVES is suitable. However, in order to observe the bulge/bar through the covering gas and dust, observations are preferably carried out in the infrared, and low extinction windows will have to be used. In addition to solely do these kinds of observations, it would be beneficial to obtain high resolution infrared spectra of the stellar sample in this work and compare the resulting abundances from analysis of those spectra. This is necessary to see if there are any discrepancies in abundances determined from optical or infrared data, which should be taken into account.

With more observation time, the present reference sample could be extended to include more metal-poor stars, which would be beneficial to understand the early times of the Galaxy better. However, a majority of the metal-poor stars in this sample could not be analysed for several of the neutron-capture elements, due to the lines not being visible. To attack this problem, stars at the uppermost end of the giant branch would have to be chosen. These have lower effective temperatures and lower surface gravities, which results in stronger lines.

Another thing to continue with is the origin of the elements. Firstly, it would be interesting to see which elements are produced by the weak s-process. In [Lomaeva et al. \(2019\)](#) their abundances of Co and Ni ( $Z = 27$  and  $Z = 28$ , respectively) are increasing at supersolar metallicities, indicating a metallicity-dependent yield and perhaps a contribution from the weak s-process. Abundance measurements of the neutron-capture elements Zn, Ge, Rb and Sr would give a better insight into this, as well as allowing better constraints to be put on the production of the first s-process peak. However, I put effort into analysing Zn and Sr in this work, without good results, and measurements of these elements in the optical range might be too cumbersome to overcome.

In the infrared wavelength regime, visible lines of five neutron-capture elements look promising for abundance determination. These elements are Cu, Ge, Ce, Nd and Yb, where Ge and Yb would be of great interest to complement the elements analysed in this work. Additionally, since infrared observations are extremely important for being able to observe the Galactic centre, it is favourable to have accurate abundances in this regime too. As a part of this, it is necessary to constrain whether or not abundances in the visual and in the infrared give similar results. To have accurate abundances for both Cu, Ce and Nd in this work allows for a comparison with future work done in the infrared on these elements.

As for the r-process elements the question regarding SNe II and/or neutron star mergers as the production sources is still left unanswered. One approach to this is to measure the abundance of ultra-heavy r-process elements, such as the actinides ( $Z = 89-103$ ). Most of these are unstable and decay radioactively. Therefore, they can be used as clocks that give the time interval from nucleosynthesis to the detection of them here at Earth. Neutron star mergers are believed to be much less frequent in the Galaxy than SNe II, possibly  $\sim 1000$  times less frequent ([Chruslinska et al. 2018](#)). The ratios of the heavy r-process isotopes, each with its own specific half-life, enables the determination of whether the heaviest r-process nuclei are produced in SNe II or in neutron star mergers ([Binns et al. 2019](#)). However, since I measure the abundance of stars that are rather old (in comparison to the radioactive decay of these isotopes), there will not be anything of these isotopes, and one would have to pinpoint, for example, the resulting ISM or gamma ray burst of a neutron star merger to measure the elements. This is clearly outside the scope of this work.



Other examples of heavy r-process elements that can be measured (in the optical) are Yb, lines at 5556.48 Å and 5588.47 Å, and Tm, line at 5034.22 Å. In this work I considered Eu and Gd. To have other r-process elements to compare with would constrain the production of these elements, similarly to how the first and second s-process peak elements have been used in this work.

# Bibliography

- Abbott, B. P., Abbott, R., Abbott, T. D., et al. 2017, *Phys. Rev. Lett.*, 119, 161101
- Adibekyan, V. Z., Santos, N. C., Sousa, S. G., & Israelian, G. 2011, *A&A*, 535, L11
- Adibekyan, V. Z., Sousa, S. G., Santos, N. C., et al. 2012, *A&A*, 545, A32
- Aller, L. H. & Greenstein, J. L. 1960, *The Astrophysical Journal Supplement Series*, 5, 139
- Arcones, A. & Montes, F. 2011, *ApJ*, 731, 5
- Asplund, M. 2005, *Annual Review of Astronomy and Astrophysics*, 43, 481
- Asplund, M., Grevesse, N., Sauval, A. J., & Scott, P. 2009, *Annual Review of Astronomy and Astrophysics*, 47, 481
- Astropy Collaboration, Robitaille, T. P., Tollerud, E. J., et al. 2013, *A&A*, 558, A33
- Bailer-Jones, C. A. L., Rybizki, J., Fouesneau, M., Mantelet, G., & Andrae, R. 2018, *AJ*, 156, 58
- Baschek, B. 1959, *Zeitschrift für Astrophysik*, 48, 95
- Battistini, C. & Bensby, T. 2016, *A&A*, 586, A49
- Bensby, T., Feltzing, S., & Oey, M. S. 2014, *A&A*, 562, A71
- Bensby, T., Zenn, A. R., Oey, M. S., & Feltzing, S. 2007, *ApJ*, 663, L13
- Biémont, É., Blagoev, K., Engström, L., et al. 2011, *MNRAS*, 414, 3350, (BBEHL)
- Biemont, E., Grevesse, N., Hannaford, P., & Lowe, R. M. 1981, *ApJ*, 248, 867, (BGHL)
- Binns, W. R., Israel, M. H., Rauch, B. F., et al. 2019, arXiv e-prints, arXiv:1903.12228
- Bisterzo, S., Travaglio, C., Gallino, R., Wiescher, M., & Käppeler, F. 2014, *ApJ*, 787, 10
- Bisterzo, S., Travaglio, C., Wiescher, M., et al. 2016, in *Journal of Physics Conference Series*, Vol. 665, 012023
- Bisterzo, S., Travaglio, C., Wiescher, M., Käppeler, F., & Gallino, R. 2017, *ApJ*, 835, 97
- Bland-Hawthorn, J. & Gerhard, O. 2016, *Annual Review of Astronomy and Astrophysics*, 54, 529

- Burbidge, E. M., Burbidge, G. R., Fowler, W. A., & Hoyle, F. 1957, *Reviews of Modern Physics*, 29, 547
- Burris, D. L., Pilachowski, C. A., Armandroff, T. E., et al. 2000, *ApJ*, 544, 302
- Busso, M., Gallino, R., & Wasserburg, G. J. 1999, *Annual Review of Astronomy and Astrophysics*, 37, 239
- Carlsson, J., Sturesson, L., & Svanberg, S. 1989, *Zeitschrift fur Physik D Atoms Molecules Clusters*, 11, 287
- Castro, S., Porto de Mello, G. F., & da Silva, L. 1999, *MNRAS*, 305, 693
- Cescutti, G., Chiappini, C., Hirschi, R., & Meynet, G. 2015, in *IAU General Assembly*, Vol. 29, 2257239
- Cescutti, G., Chiappini, C., Hirschi, R., Meynet, G., & Frischknecht, U. 2013, *A&A*, 553, A51
- Cescutti, G., Hirschi, R., Nishimura, N., et al. 2018, arXiv:1810.04556
- Chang, T. L., Qian, Q.-Y., Zhao, M.-T., & Wang, J. 1994, *International Journal of Mass Spectrometry and Ion Processes*, 139, 95
- Chang, T.-L., Qian, Q.-Y., Zhao, M.-T., Wang, J., & Lang, Q.-Y. 1995, *International Journal of Mass Spectrometry and Ion Processes*, 142, 125
- Chruslinska, M., Belczynski, K., Klencki, J., & Benacquista, M. 2018, *MNRAS*, 474, 2937
- Clayton, D. D. & Rassbach, M. E. 1967, *ApJ*, 148, 69
- Collins, T. L., Rourke, F. M., & White, F. A. 1957, *Physical Review*, 105, 196
- Côté, B., Belczynski, K., Fryer, C. L., et al. 2017, *ApJ*, 836, 230
- Côté, B., Denissenkov, P., Herwig, F., et al. 2018a, *ApJ*, 854, 105
- Côté, B., Eichler, M., Arcones, A., et al. 2018b, arXiv:1809.03525
- Couch, R. G., Schmiedekamp, A. B., & Arnett, W. D. 1974, *ApJ*, 190, 95
- Cowan, J. J. & Rose, W. K. 1977, *ApJ*, 212, 149
- Cristallo, S., Abia, C., Straniero, O., & Piersanti, L. 2015, *ApJ*, 801, 53
- de Laeter, J. R. & Bukilic, N. 2005, *International Journal of Mass Spectrometry*, 244, 91
- Delgado Mena, E., Tsantaki, M., Adibekyan, V. Z., et al. 2017, *A&A*, 606, A94
- Den Hartog, E. A., Lawler, J. E., Sneden, C., & Cowan, J. J. 2003, *Astrophys. J. Suppl. Ser.*, 148, 543, (HLSC)
- Den Hartog, E. A., Lawler, J. E., Sneden, C., & Cowan, J. J. 2006, *Astrophys. J. Suppl. Ser.*, 167, 292, (DLSC)

- Denissenkov, P., Herwig, F., Woodward, P., et al. 2018, arXiv:1809.03666
- Dolk, L., Wahlgren, G. M., Lundberg, H., et al. 2002, *A&A*, 385, 111
- Drout, M. R., Piro, A. L., Shappee, B. J., et al. 2017, *Science*, 358, 1570
- Duggan, G. E., Kirby, E. N., Andrievsky, S. M., & Korotin, S. A. 2018, *ApJ*, 869, 50
- Eugster, O., Tera, F., Burnett, D., & Wasserburg, G. 1970, *Journal of Geophysical Research*, 75, 2753
- Feltzing, S., Howes, L. M., McMillan, P. J., & Stonkutė, E. 2017, *MNRAS*, 465, L109
- Frischknecht, U., Hirschi, R., Pignatari, M., et al. 2016, *MNRAS*, 456, 1803
- Frischknecht, U., Hirschi, R., & Thielemann, F. K. 2012, *A&A*, 538, L2
- Gaia Collaboration, Brown, A. G. A., Vallenari, A., et al. 2018, *A&A*, 616, A1
- Gilmore, G. & Reid, N. 1983, *MNRAS*, 202, 1025
- Gray, D. F. 2005, *The Observation and Analysis of Stellar Photospheres*, 3rd edn., Vol. 3 (Cambridge University Press, The Edingburgh Building, Cambridge CB2 8RU, UK: Cambridge University Press), ch. 13, p. 327
- Grevesse, N., Asplund, M., & Sauval, A. J. 2007, , 130, 105
- Grevesse, N., Scott, P., Asplund, M., & Sauval, A. J. 2015, *A&A*, 573, A27
- Gruyters, P., Lind, K., Richard, O., et al. 2016, *A&A*, 589, A61
- Guiglion, G., de Laverny, P., Recio-Blanco, A., & Prantzos, N. 2018, *A&A*, 619, A143
- Guiglion, G., de Laverny, P., Recio-Blanco, A., et al. 2016, *A&A*, 595, A18
- Gustafsson, B., Edvardsson, B., Eriksson, K., et al. 2008, *A&A*, 486, 951
- Hampel, M., Stancliffe, R. J., Lugaro, M., & Meyer, B. S. 2016, *ApJ*, 831, 171
- Hayden, M. R., Bovy, J., Holtzman, J. A., et al. 2015, *ApJ*, 808, 132
- Haywood, M., Snaith, O. N., Lehnert, M. D., Di Matteo, P., & Khoperskov, S. 2019, arXiv:1903.03188
- Heiter, U. & Eriksson, K. 2006, *A&A*, 452, 1039
- Herwig, F. 2005, *ARA&A*, 43, 435
- Herwig, F., Langer, N., & Lugaro, M. 2003, *ApJ*, 593, 1056
- Hinkle, K., Wallace, L., Harmer, D., Ayres, T., & Valenti, J. 2000, in *IAU Joint Discussion*, Vol. 24, 26
- Holtzman, J. A., Hasselquist, S., Shetrone, M., et al. 2018, *AJ*, 156, 125
- Ivarsson, S., Litzén, U., & Wahlgren, G. M. 2001, *Physica Scripta*, 64, 455, (ILW)

- Ji, A. P., Frebel, A., Simon, J. D., & Chiti, A. 2016, *ApJ*, 830, 93
- Jofré, P., Heiter, U., Soubiran, C., et al. 2015, *A&A*, 582, A81
- Jönsson, H., Allende Prieto, C., Holtzman, J. A., et al. 2018, *AJ*, 156, 126
- Jönsson, H., Ryde, N., Harper, G. M., Richter, M. J., & Hinkle, K. H. 2015, in *Astronomical Society of the Pacific Conference Series*, Vol. 497, *Why Galaxies Care about AGB Stars III: A Closer Look in Space and Time*, ed. F. Kerschbaum, R. F. Wing, & J. Hron, 269
- Jönsson, H., Ryde, N., Nordlander, T., et al. 2017a, *A&A*, 598, A100
- Jönsson, H., Ryde, N., Schultheis, M., & Zoccali, M. 2017b, *A&A*, 600, C2
- Jordi, C., Gebran, M., Carrasco, J. M., et al. 2010, *A&A*, 523, A48
- Käppeler, F., Gallino, R., Bisterzo, S., & Aoki, W. 2011, *Reviews of Modern Physics*, 83, 157
- Karakas, A. I. & Lattanzio, J. C. 2003, *Publications of the Astronomical Society of Australia*, 20, 279
- Karakas, A. I. & Lugaro, M. 2016, *ApJ*, 825, 26
- Kobayashi, C., Umeda, H., Nomoto, K., Tominaga, N., & Ohkubo, T. 2006, *ApJ*, 653, 1145
- Kock, M. & Richter, J. 1968, , 69, 180, (KR)
- Korn, A. J., Grundahl, F., Richard, O., et al. 2007, *ApJ*, 671, 402
- Kratz, K.-L., Farouqi, K., Pfeiffer, B., et al. 2007, *ApJ*, 662, 39
- Lagarde, N., Miglio, A., Eggenberger, P., et al. 2015, in *IAU General Assembly*, Vol. 29, 2246886
- Lambert, D. L. 1991, in *IAU Symposium*, Vol. 145, *Evolution of Stars: the Photospheric Abundance Connection*, ed. G. Michaud & A. V. Tutukov, 299
- Lattanzio, J., Frost, C., Cannon, R., & Wood, P. R. 1996, *Memorie della Societa Astronomica Italiana*, 67, 729
- Lattanzio, J. C. 1989, *ApJ*, 344, L25
- Lawler, J. E., Bonvallet, G., & Sneden, C. 2001a, *Astrophys. J.*, 556, 452, (LBS)
- Lawler, J. E., Sneden, C., Cowan, J. J., Ivans, I. I., & Den Hartog, E. A. 2009, *Astrophys. J. Suppl. Ser.*, 182, 51, (LSCI)
- Lawler, J. E., Wickliffe, M. E., den Hartog, E. A., & Sneden, C. 2001b, *Astrophys. J.*, 563, 1075, (LWHS)
- Lee, B. C., Han, I., Park, M. G., et al. 2014, *A&A*, 566, A67
- Li, R., Chatelain, R., Holt, R. A., et al. 2007, , 76, 577
- Lind, K., Bergemann, M., & Asplund, M. 2012, *MNRAS*, 427, 50

- Lind, K., Korn, A. J., Barklem, P. S., & Grundahl, F. 2008, *A&A*, 490, 777
- Lippuner, J., Fernández, R., Roberts, L. F., et al. 2017, *MNRAS*, 472, 904
- Liu, F., Asplund, M., Yong, D., et al. 2019, arXiv:1902.11008
- Lomaeva, M., Jönsson, H., Ryde, N., Schultheis, M., & Thorsbro, B. 2019, *A&A*, arXiv:1903.01476
- Majewski, S. R., Schiavon, R. P., Frinchaboy, P. M., et al. 2017, *AJ*, 154, 94
- Malkin, Z. 2012, arXiv:1202.6128
- Marigo, P., Girardi, L., Bressan, A., et al. 2017, *ApJ*, 835, 77
- Marshall, J., Hansen, T., Simon, J., et al. 2018, arXiv e-prints, arXiv:1812.01022
- Martig, M., Fouesneau, M., Rix, H.-W., et al. 2016, *MNRAS*, 456, 3655
- Mashonkina, L. & Gehren, T. 2000, *A&A*, 364, 249
- McMillan, P. J. 2011, *MNRAS*, 414, 2446
- McMillan, P. J. 2018, *Research Notes of the American Astronomical Society*, 2, 51
- McWilliam, A. 2016, *Publications of the Astronomical Society of Australia*, 33, e040
- Meléndez, J., Asplund, M., Gustafsson, B., & Yong, D. 2009, *ApJ*, 704, L66
- Mikolaitis, Š., de Laverny, P., Recio-Blanco, A., et al. 2017, *A&A*, 600, A22
- Mishenina, T. V., Pignatari, M., Korotin, S. A., et al. 2013, *A&A*, 552, A128
- Montes, F., Beers, T. C., Cowan, J., et al. 2007, *ApJ*, 671, 1685
- Ness, M., Hogg, D. W., Rix, H. W., et al. 2016, *ApJ*, 823, 114
- Nishimura, N., Takiwaki, T., & Thielemann, F.-K. 2015, *ApJ*, 810, 109
- Nissen, P. E. 2004, in *Origin and Evolution of the Elements*, ed. A. McWilliam & M. Rauch, 154
- Nissen, P. E. 2016, *A&A*, 593, A65
- Nomura, M., Kogure, K., & Okamoto, M. 1983, *International Journal of Mass Spectrometry and Ion Processes*, 50, 219
- Nordlander, T., Korn, A. J., Richard, O., & Lind, K. 2012, *ApJ*, 753, 48
- Palmeri, P., Quinet, P., Wyart, J., & Biéumont, E. 2000, *Physica Scripta*, 61, 323, (PQWB)
- Pinsonneault, M. H., Elsworth, Y. P., Tayar, J., et al. 2018, *The Astrophysical Journal Supplement Series*, 239, 32
- Piskunov, N. & Valenti, J. A. 2017, *A&A*, 597, A16

- Prochaska, J. X. & McWilliam, A. 2000, *ApJ*, 537, L57
- Ramírez, I. & Allende Prieto, C. 2011, *ApJ*, 743, 135
- Reddy, B. E., Lambert, D. L., & Allende Prieto, C. 2006, *MNRAS*, 367, 1329
- Reddy, B. E., Tomkin, J., Lambert, D. L., & Allende Prieto, C. 2003, *MNRAS*, 340, 304
- Romano, D. & Matteucci, F. 2007, *MNRAS*, 378, L59
- Rosswog, S., Korobkin, O., Arcones, A., Thielemann, F. K., & Piran, T. 2014, *MNRAS*, 439, 744
- Rosswog, S., Piran, T., & Nakar, E. 2013, *MNRAS*, 430, 2585
- Rutten, R. J. 2003, *Radiative Transfer in Stellar Atmospheres*
- Ryabchikova, T. A., Savanov, I. S., Malanushenko, V. P., & Kudryavtsev, D. O. 2001, *Astronomy Reports*, 45, 382
- Safarzadeh, M., Sarmiento, R., & Scannapieco, E. 2018, arXiv:1812.02779
- Shi, J. R., Gehren, T., Zeng, J. L., Mashonkina, L., & Zhao, G. 2014, *ApJ*, 782, 80
- Shields, W. R., Goldich, S. S., Garner, E. L., & Murphy, T. J. 1965, *Journal of Geophysical Research*, 70, 479
- Siegel, D. M., Barnes, J., & Metzger, B. D. 2018, arXiv:1810.00098
- Slumstrup, D., Grundahl, F., Brogaard, K., et al. 2017, *A&A*, 604, L8
- Snedden, C., Cowan, J. J., Ivans, I. I., et al. 2000, *The Astrophysical Journal Letters*, 533, L139
- Snedden, C., Gratton, R. G., & Crocker, D. A. 1991, *A&A*, 246, 354
- Souto, D., Allende Prieto, C., Cunha, K., et al. 2019, *ApJ*, arXiv:1902.10199
- Stoehr, F., White, R., Smith, M., et al. 2008, in *Astronomical Society of the Pacific Conference Series*, Vol. 394, *Astronomical Data Analysis Software and Systems XVII*, ed. R. W. Argyle, P. S. Bunclark, & J. R. Lewis, 505
- Telting, J. H., Avila, G., Buchhave, L., et al. 2014, *Astronomische Nachrichten*, 335, 41
- Thielemann, F.-K., Arcones, A., Käppeli, R., et al. 2011, *Progress in Particle and Nuclear Physics*, 66, 346, particle and Nuclear Astrophysics
- Thorsbro, B., Ryde, N., Schultheis, M., et al. 2018, *ApJ*, 866, 52
- Titarenko, A., Recio-Blanco, A., de Laverny, P., Hayden, M., & Guiglion, G. 2019, *A&A*, 622, A59
- Travaglio, C., Galli, D., Gallino, R., et al. 1999, *ApJ*, 521, 691
- Travaglio, C., Gallino, R., Arnone, E., et al. 2004, *ApJ*, 601, 864

- Travaglio, C., Gallino, R., Busso, M., & Gratton, R. 2001, *ApJ*, 549, 346
- Trippella, O., Busso, M., Maiorca, E., Käppeler, F., & Palmerini, S. 2015, in *Astronomical Society of the Pacific Conference Series*, Vol. 497, *Why Galaxies Care about AGB Stars III: A Closer Look in Space and Time*, ed. F. Kerschbaum, R. F. Wing, & J. Hron, 275
- Valenti, J. A. & Piskunov, N. 1996, *Astronomy and Astrophysics Supplement Series*, 118, 595
- Van der Swaelmen, M., Barbuy, B., Hill, V., et al. 2016, *A&A*, 586, A1
- Velichko, A. B., Mashonkina, L. I., & Nilsson, H. 2010, *Astronomy Letters*, 36, 664
- Wanajo, S. 2013, *ApJ*, 770, L22
- Wanajo, S. 2018, *ApJ*, 868, 65
- Wanajo, S., Janka, H.-T., & Müller, B. 2011, *ApJ*, 726, L15
- Wanajo, S., Tamamura, M., Itoh, N., et al. 2003, *ApJ*, 593, 968
- Wu, M.-R., Fernández, R., Martínez-Pinedo, G., & Metzger, B. D. 2016, *MNRAS*, 463, 2323
- Xu, X. D., Shi, J. R., & Yan, H. L. 2019, *ApJ*, 875, 142
- Zhao, M., Zhou, T., Wang, J., et al. 2005, *Rapid Communications in Mass Spectrometry*, 19, 2743



# Appendices

# Appendix A

## Synthetic spectral lines

In this appendix the synthetic spectra (in red) produced for all elements are shown together with the observed spectra (in black) for the red giant, Arcturus ( $\alpha$ -Boo, HD124897, HIP 69673). At the bottom the wavelength regime is noted. The continuum masks can be seen in yellow and the line masks in orange. Above the spectra the sensitivity of the lines to different stellar parameters ( $T_{\text{eff}}$ ,  $\log g$ ,  $[\text{Fe}/\text{H}]$ ,  $v_{\text{mic}}$ , top to bottom) is indicated, going from purple (not sensitive) to green/yellow and red for higher sensitivity. Everything within the blue vertical lines mark the segment (the white area) used to produce the synthetic spectra whilst grey is not used. The stellar parameters used are seen at the top, going from  $T_{\text{eff}}$ ,  $\log g$ ,  $[\text{Fe}/\text{H}]$ ,  $v_{\text{mic}}$  and  $v_{\text{mac}}$ . The last number is the signal-to-noise ratio.

The order of elements goes from increasing atomic number, starting with Cu. The elements, and the lines, are also included in the captions. The GES notification assigned to the lines from Heiter et al. in prep., if any, where Y (yes), U (uncertain) and N (no) represent the usability of the line from their assessment.

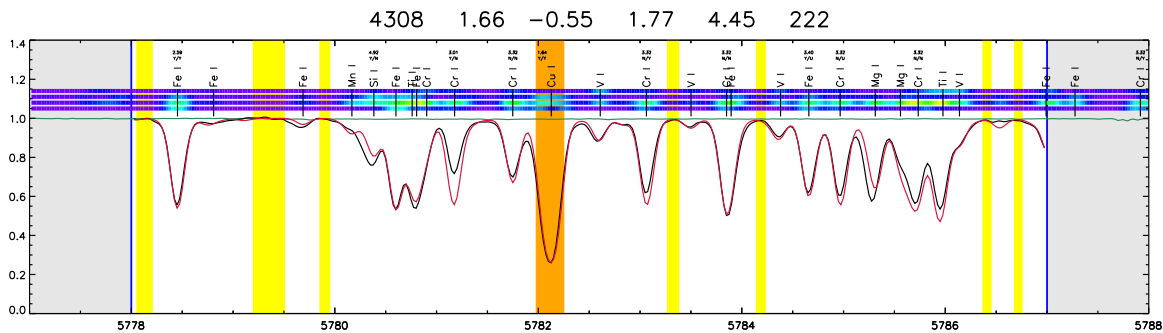


**Figure A.0.1:** Synthetic spectra to fit the Cu line: 5782.11 Å, GES classification Y/Y.

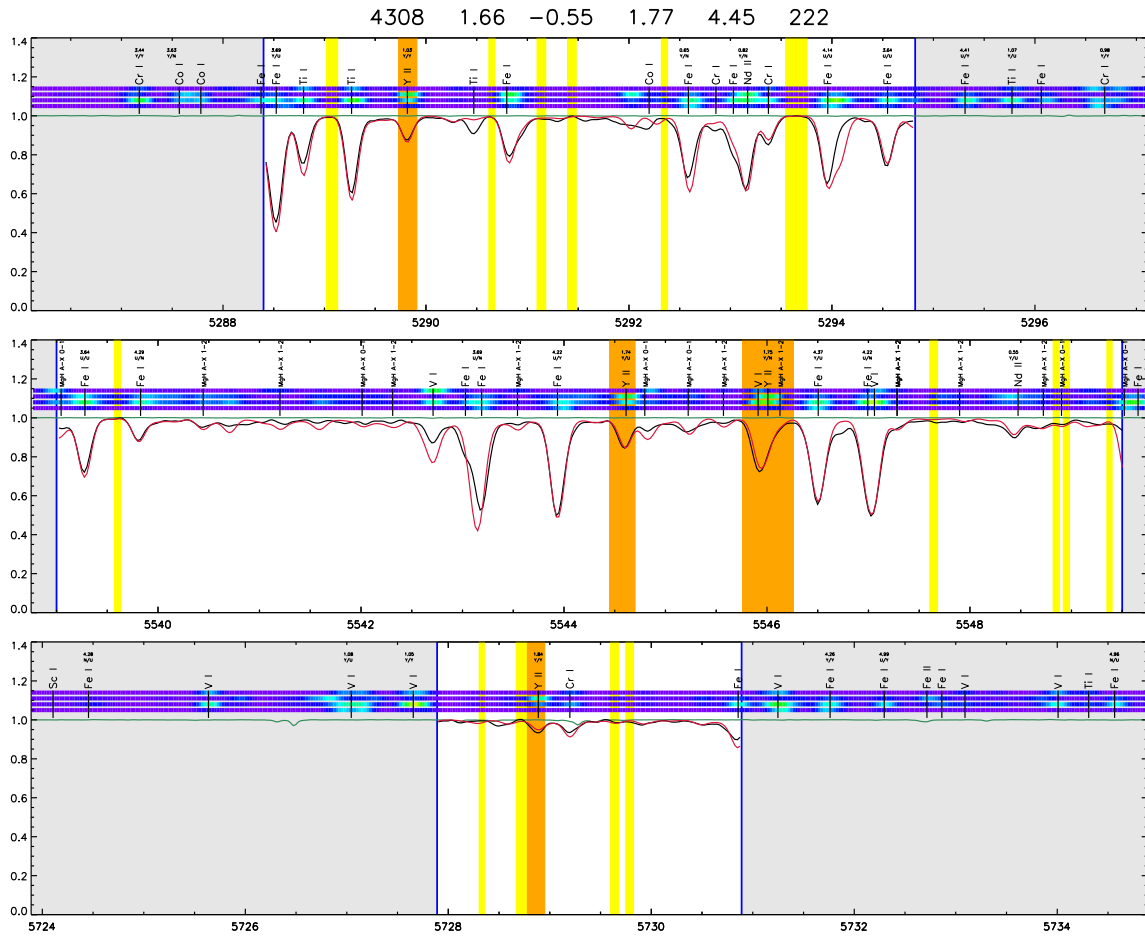


**Figure A.0.2:** Synthetic spectra to fit the three Y lines: 5289.81 Å, GES classification: Y/Y, 5544.61 Å, GES classification: Y/U, 5728.89 Å, GES classification: Y/Y .

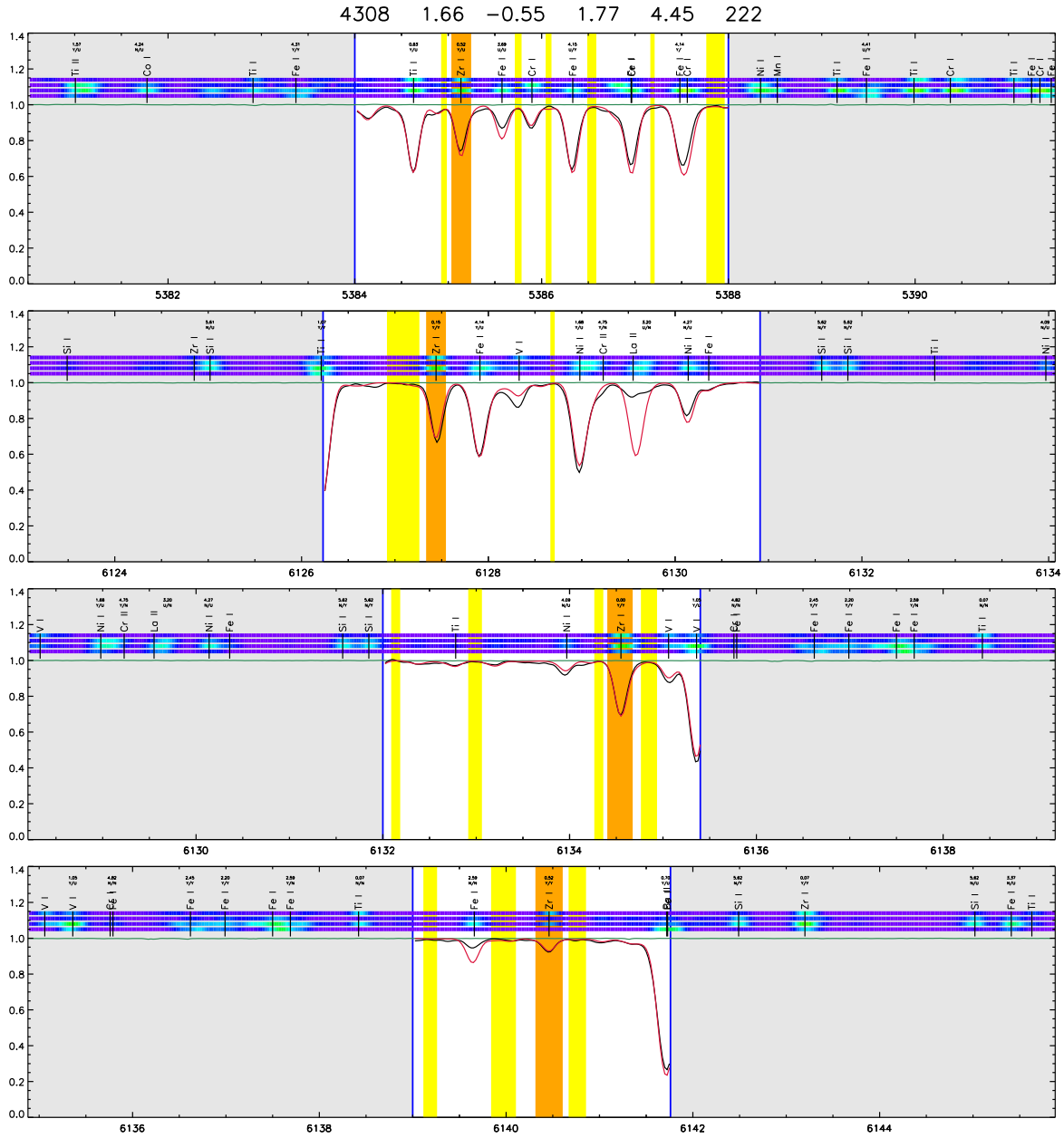


**Figure A.0.3:** Synthetic spectra to fit the four Zr lines: 5385.14 Å, GES classification: Y/U, 6134.55 Å, GES classification: Y/Y, 6140.49 Å, GES classification: Y/Y, 6143.23 Å, GES classification: Y/Y.

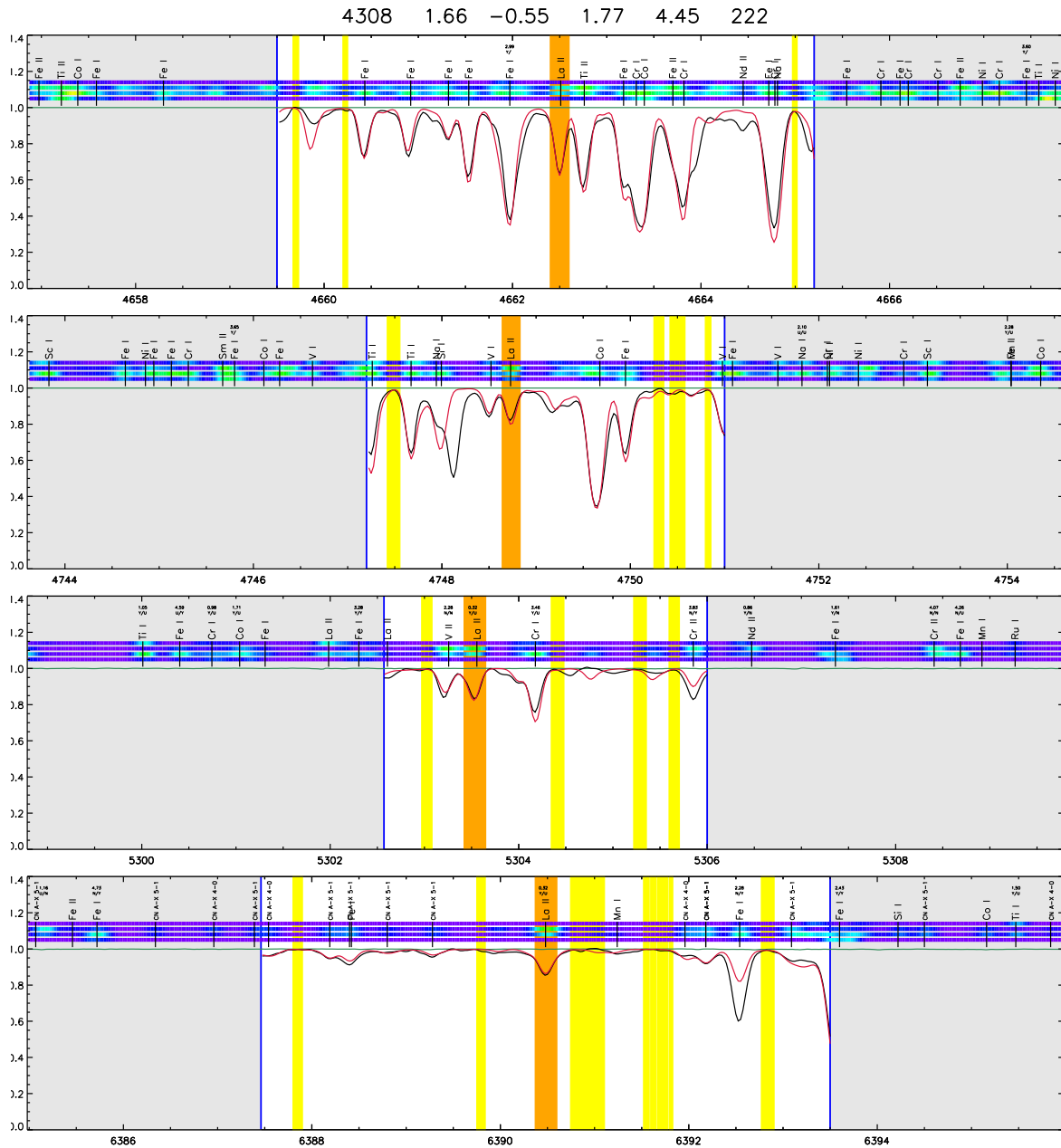


**Figure A.0.4:** Synthetic spectra to fit the four La lines: 4662.51 Å, not classified in GES, 4748.73 Å, not classified in GES, 5303.53 Å, GES classification: Y/U, 6390.48 Å, GES classification: Y/U.

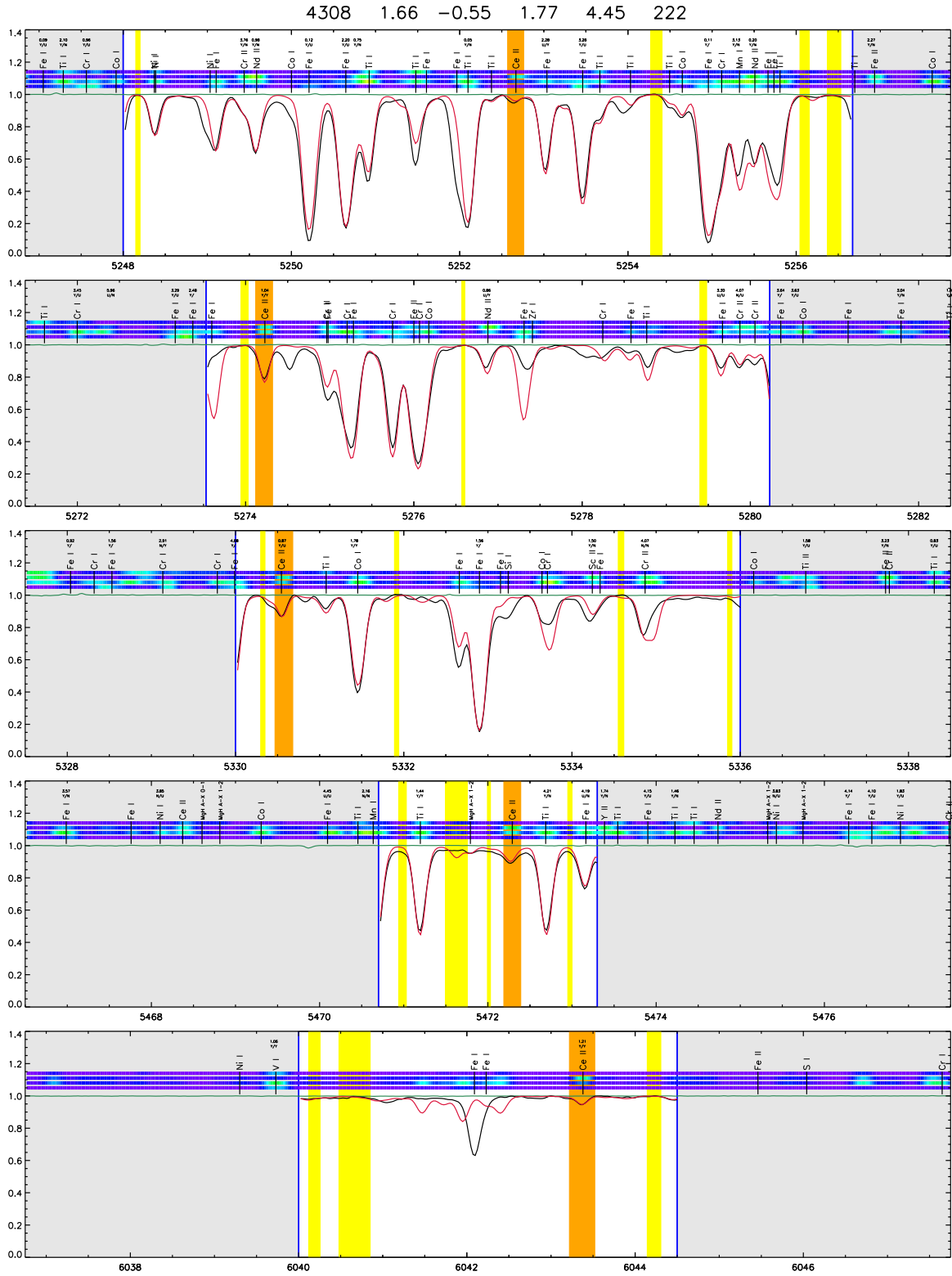


**Figure A.0.5:** Synthetic spectra to fit the five Ce lines: 5252.67 Å, not classified in GES, 5274.23 Å, GES classification: Y/Y, 5330.55 Å, GES classification: Y/U, 5472.29 Å, not classified in GES, 6043.38 Å, GES classification: Y/Y.

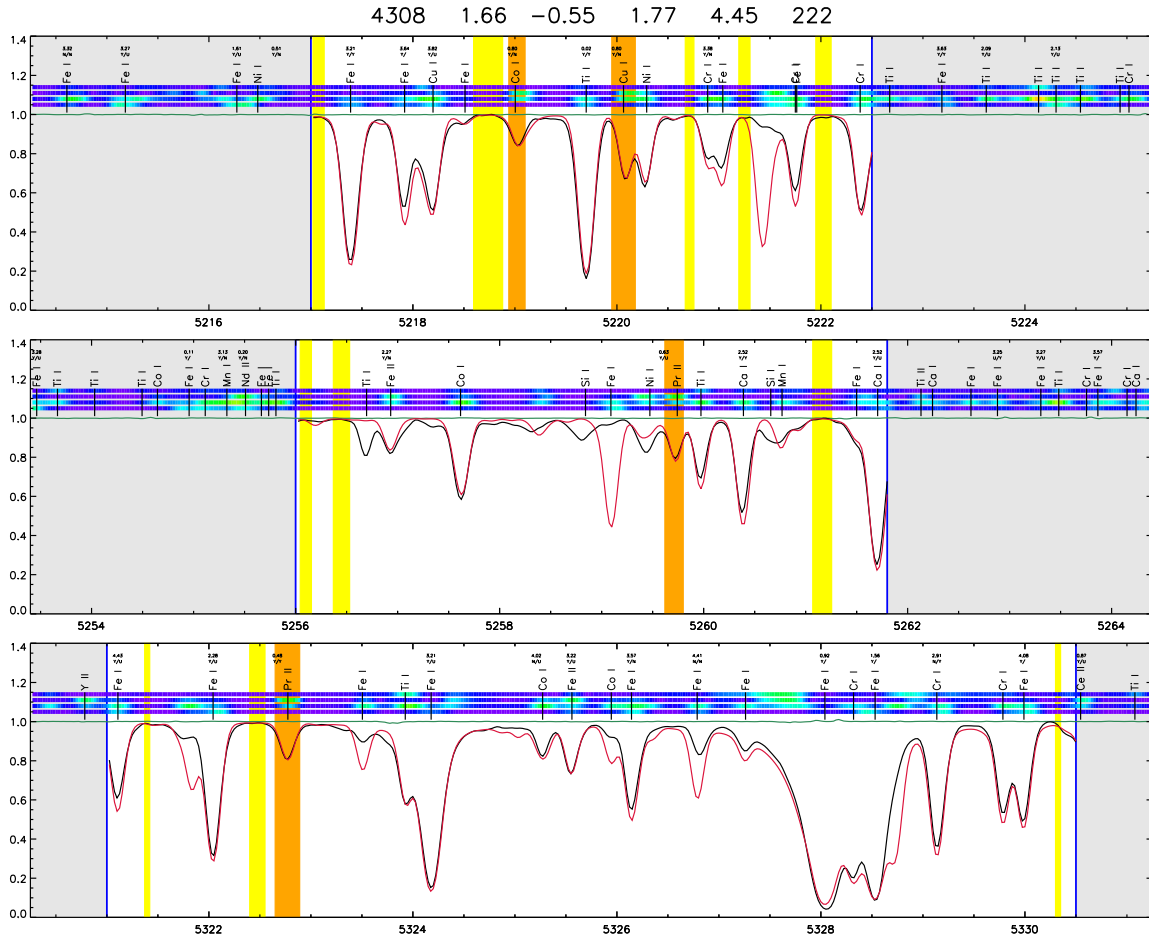


**Figure A.0.6:** Synthetic spectra to fit the three Pr lines: 5220.06 Å, GES classification: Y/N, 5259.68 Å, GES classification: Y/U, 5322.74 Å, GES classification: Y/Y. The first line is classified as Y/N. It is blended with a Cu I line, however, due to the good fit of the synthetic spectra and its contribution to tightening the trend, the line is kept in the analysis.

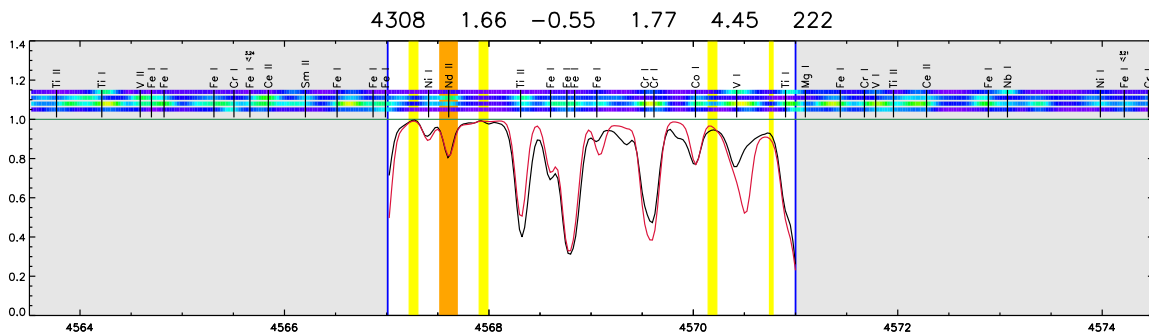


**Figure A.0.7:** Synthetic spectra to fit the Nd line: 4567.61 Å, not classified in GES.

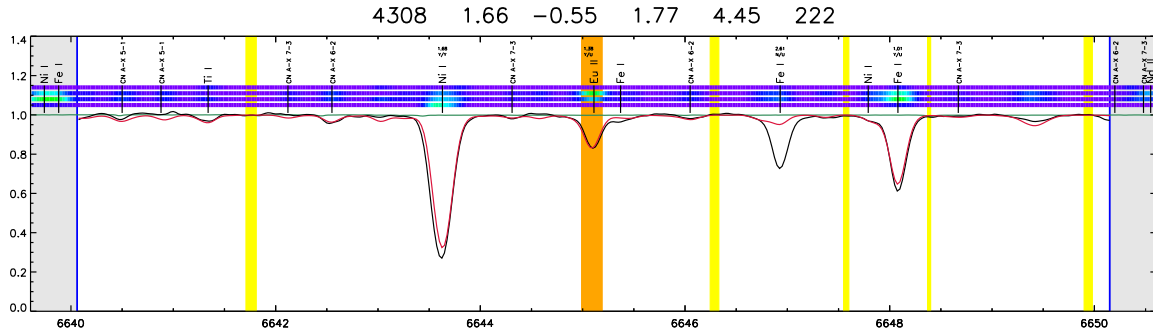


**Figure A.0.8:** Synthetic spectra to fit the Eu line: 6645.10 Å, GES classification: Y/Y. This line is sensitive to  $\log g$ , which possibly could explain the supersolar values.

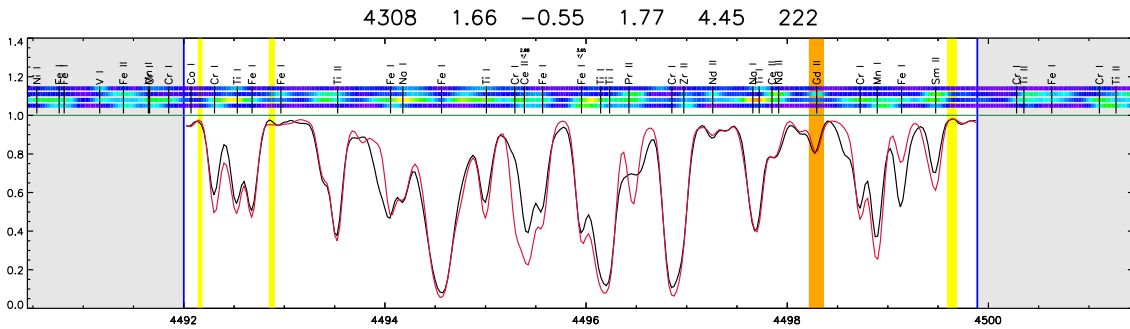


**Figure A.0.9:** Synthetic spectra to fit the Gd line: 4498.29 Å, not classified in GES. As for the Eu line, this line is also sensitive to  $\log g$ , which possible could explain the supersolar values.



## Appendix B

# Atomic data for spectral lines

**Table B.1:** Atomic lines used in the analysis. The elements and ionisation states are given in column 1, the transition wavelength is shown in column 2, and  $\log gf$  values are listed in column 3. The energy of the lower energy level is given in column 4. Finally, column 5 specifies the reference for the  $\log gf$  -values.

Element	Wavelength [ $\text{\AA}$ ]	$\log gf$	$E_{\text{exc}}^{\text{low}}$ [eV]	Reference
Cu I	5782.0385	-3.3280	1.6420	<a href="#">Kock &amp; Richter (1968)</a> ; <a href="#">Carlsson et al. (1989)</a>
Cu I	5782.0570	-3.1060	1.6420	<a href="#">Kock &amp; Richter (1968)</a> ; <a href="#">Carlsson et al. (1989)</a>
Cu I	5782.0680	-2.9771	1.6420	<a href="#">Kock &amp; Richter (1968)</a> ; <a href="#">Carlsson et al. (1989)</a>
Cu I	5782.0852	-2.7551	1.6420	<a href="#">Kock &amp; Richter (1968)</a> ; <a href="#">Carlsson et al. (1989)</a>
Cu I	5782.0877	-3.1060	1.6420	<a href="#">Kock &amp; Richter (1968)</a> ; <a href="#">Carlsson et al. (1989)</a>
Cu I	5782.0998	-3.1060	1.6420	<a href="#">Kock &amp; Richter (1968)</a> ; <a href="#">Carlsson et al. (1989)</a>
Cu I	5782.1137	-2.7551	1.6420	<a href="#">Kock &amp; Richter (1968)</a> ; <a href="#">Carlsson et al. (1989)</a>
Cu I	5782.1250	-2.7551	1.6420	<a href="#">Kock &amp; Richter (1968)</a> ; <a href="#">Carlsson et al. (1989)</a>
Cu I	5782.1554	-2.6590	1.6420	<a href="#">Kock &amp; Richter (1968)</a> ; <a href="#">Carlsson et al. (1989)</a>
Cu I	5782.1774	-2.3081	1.6420	<a href="#">Kock &amp; Richter (1968)</a> ; <a href="#">Carlsson et al. (1989)</a>
Y II	5289.8150	-1.6800	1.0330	<a href="#">Biémont et al. (2011)</a>
Y II	5544.6110	-0.8300	1.7380	<a href="#">Biémont et al. (2011)</a>
Y II	5728.8865	-1.1500	1.8390	<a href="#">Biémont et al. (2011)</a>
Zr I	5385.1400	-0.7100	0.5190	<a href="#">Biemont et al. (1981)</a>
Zr I	6127.4400	-1.0600	0.1540	<a href="#">Biemont et al. (1981)</a>
Zr I	6134.5500	-1.2800	0.0000	<a href="#">Biemont et al. (1981)</a>
Zr I	6140.4600	-1.4100	0.5190	<a href="#">Biemont et al. (1981)</a>
La II	4662.5000	-1.2400	0.0000	<a href="#">Lawler et al. (2001a)</a>
La II	4748.7300	-0.5400	0.9270	<a href="#">Lawler et al. (2001a)</a>
La II	5303.5139	-1.7314	0.3210	<a href="#">Lawler et al. (2001a)</a>
La II	5303.5317	-1.8284	0.3210	<a href="#">Lawler et al. (2001a)</a>
La II	5303.5458	-1.9534	0.3210	<a href="#">Lawler et al. (2001a)</a>
La II	6390.4567	-2.0124	0.3210	<a href="#">Lawler et al. (2001a)</a>

continued table B.1

Element	Wavelength [Å]	$\log gf$	$E_{\text{exc}}^{\text{low}}$ [eV]	Reference
La II	6390.4690	-2.0794	0.3210	Lawler et al. (2001a)
La II	6390.4858	-1.9034	0.3210	Lawler et al. (2001a)
La II	6390.5009	-2.0794	0.3210	Lawler et al. (2001a)
Ce II	5252.6615	-0.6400	1.1550	Palmeri et al. (2000)
Ce II	5274.2290	0.1300	1.0440	Lawler et al. (2009)
Ce II	5330.5560	-0.4000	0.8690	Lawler et al. (2009)
Ce II	5472.2791	-0.1000	1.2470	Palmeri et al. (2000)
Ce II	6043.3730	-0.4800	1.2060	Lawler et al. (2009)
Pr II	5219.9983	-3.7680	0.7960	Ivarsson et al. (2001)
Pr II	5220.0157	-3.4640	0.7960	Ivarsson et al. (2001)
Pr II	5220.0318	-3.4100	0.7960	Ivarsson et al. (2001)
Pr II	5220.0460	-1.8840,	0.7960	Ivarsson et al. (2001)
Pr II	5220.0578	-1.6930	0.7960	Ivarsson et al. (2001)
Pr II	5220.0690	-1.6450	0.7960	Ivarsson et al. (2001)
Pr II	5220.0841	-1.4830	0.7960	Ivarsson et al. (2001)
Pr II	5220.0975	-0.3680	0.7960	Ivarsson et al. (2001)
Pr II	5220.1090	-0.1510	0.7960	Ivarsson et al. (2001)
Pr II	5220.1201	-0.1180	0.7960	Ivarsson et al. (2001)
Pr II	5259.6112	-3.7290	0.6330	Ivarsson et al. (2001)
Pr II	5259.6296	-3.4190	0.6330	Ivarsson et al. (2001)
Pr II	5259.6465	-3.3570	0.6330	Ivarsson et al. (2001)
Pr II	5259.6627	-1.9500	0.6330	Ivarsson et al. (2001)
Pr II	5259.6757	-1.7640	0.6330	Ivarsson et al. (2001)
Pr II	5259.6864	-1.7170	0.6330	Ivarsson et al. (2001)
Pr II	5259.7007	-1.5550	0.6330	Ivarsson et al. (2001)
Pr II	5259.7218	-0.5390	0.6330	Ivarsson et al. (2001)
Pr II	5259.7355	-0.0290	0.6330	Ivarsson et al. (2001)
Pr II	5322.6729	-2.8700	0.4830	Li et al. (2007)
Pr II	5322.7082	-1.6820	0.4830	Li et al. (2007)
Pr II	5322.7189	-1.8440	0.4830	Li et al. (2007)
Pr II	5322.7313	-1.0610	0.4830	Li et al. (2007)
Pr II	5322.7444	-1.1000	0.4830	Li et al. (2007)
Pr II	5322.7587	-1.0160	0.4830	Li et al. (2007)
Pr II	5322.7743	-0.9330	0.4830	Li et al. (2007)
Pr II	5322.7913	-0.8540	0.4830	Li et al. (2007)
Pr II	5322.8095	-0.7780	0.4830	Li et al. (2007)
Nd II	4567.6100	-1.3100	0.2050	Den Hartog et al. (2003)
Eu II	6645.0572	-0.8375	1.3800	Lawler et al. (2001b)
Eu II	6645.0598	-0.7774	1.3800	Lawler et al. (2001b)
Eu II	6645.0677	-2.1345	1.3800	Lawler et al. (2001b)
Eu II	6645.0744	-0.8374	1.3800	Lawler et al. (2001b)
Eu II	6645.0830	-0.9135	1.3800	Lawler et al. (2001b)
Eu II	6645.0858	-0.9034	1.3800	Lawler et al. (2001b)

continued table [B.1](#)

Element	Wavelength [Å]	$\log gf$	$E_{\text{exc}}^{\text{low}}$ [eV]	Reference
Eu II	6645.0978	-0.6014	1.3800	<a href="#">Lawler et al. (2001b)</a>
Eu II	6645.1006	-0.9455	1.3800	<a href="#">Lawler et al. (2001b)</a>
Eu II	6645.1205	-1.0135	1.3800	<a href="#">Lawler et al. (2001b)</a>
Eu II	6645.1366	-1.0935	1.3800	<a href="#">Lawler et al. (2001b)</a>
Eu II	6645.1490	-1.1915	1.3800	<a href="#">Lawler et al. (2001b)</a>
Gd II	4498.2860	-1.0800	0.4270	<a href="#">Den Hartog et al. (2006)</a>

# Appendix C

## Additional abundance plots

In Figure C.0.1 the abundances determined in this work can be seen for the entire stellar sample, without any of the quality cuts done in the final analysis. In Figures C.0.2 and C.0.3, the abundances separated into the stellar populations are plotted, but with respect to the magnesium abundance,  $[X/Mg]$  over  $[Mg/H]$ , instead of the metallicity. Magnesium is created solely by massive stars through SNe II which makes it a better proxy for age than iron. However, these plots do not add anything significant to the discussion, and are therefore placed in this appendix for completeness.

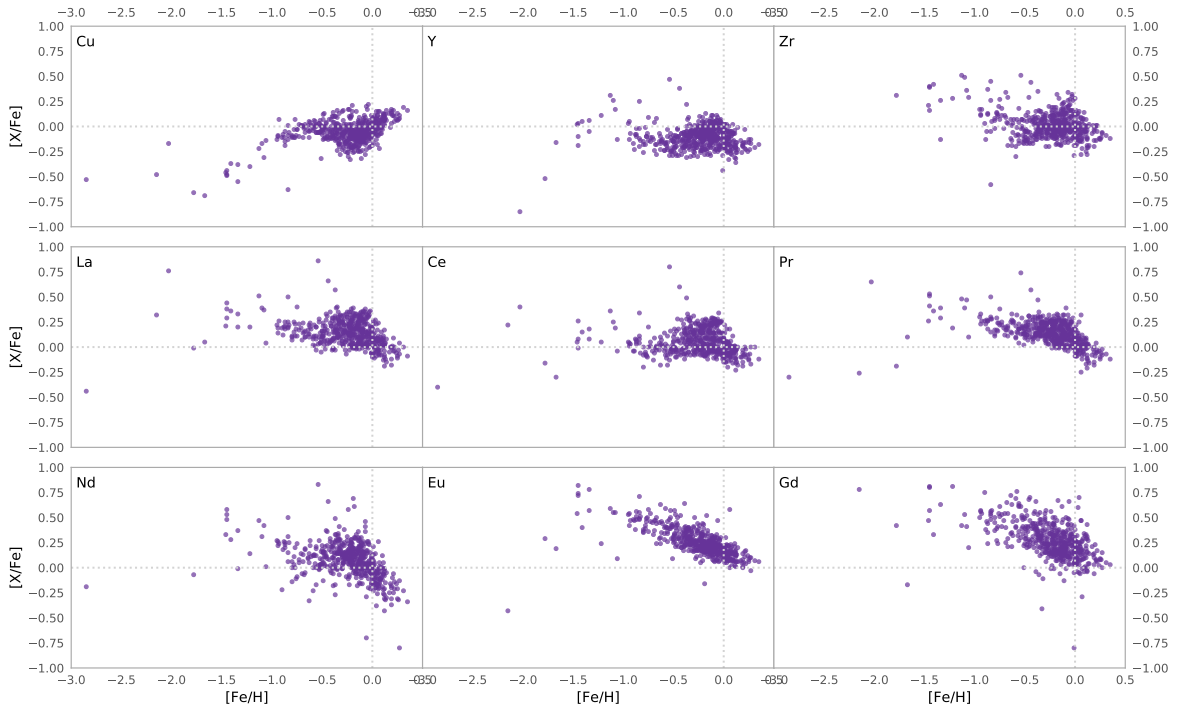


**Figure C.0.1:** Determined abundances against iron,  $[X/Fe]$  against  $[Fe/H]$ . This set includes all 523 stars in the stellar sample, without quality cuts.

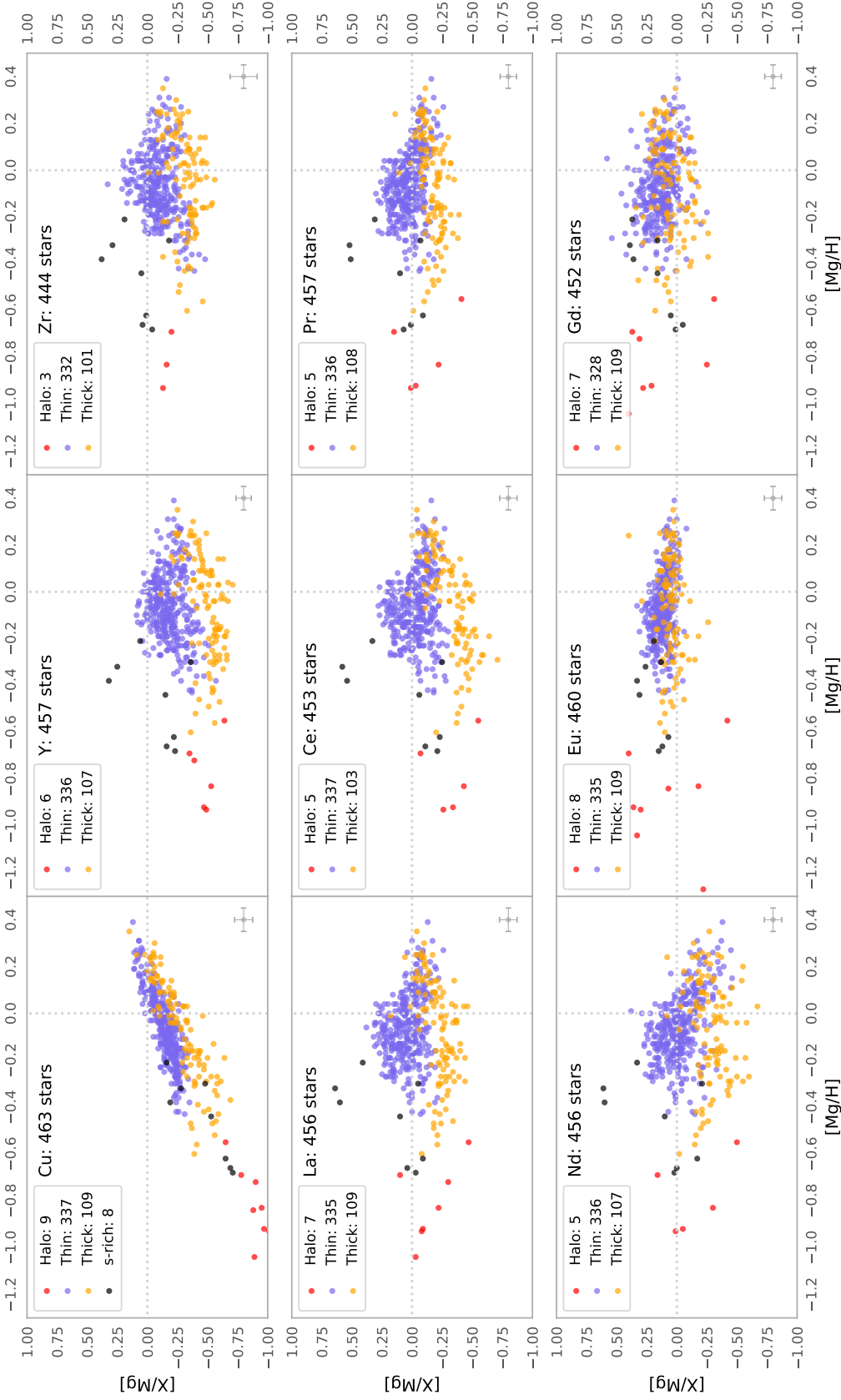


**Figure C.0.2:** Determined abundances,  $[X/Mg]$ , plotted against the magnesium abundance  $[Mg/H]$  for the different stellar classifications, as described in Section 4.4. The number of stars for each element and each stellar population is indicated in each plot, where the number of s-enriched stars is the same for all elements. The typical uncertainty, seen in Table 4.5, is indicated in the lower right corner of each plot.

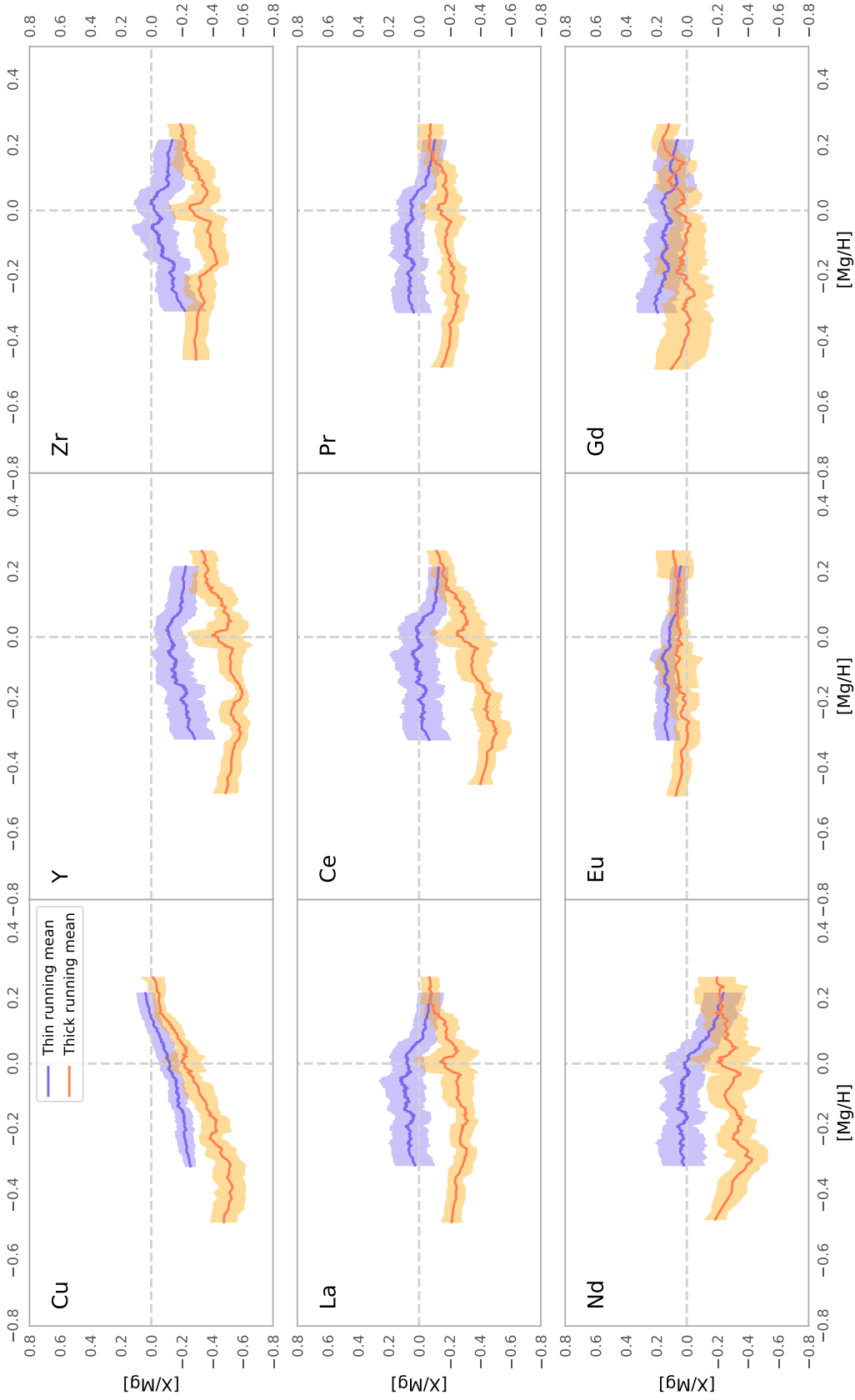



**Figure C.0.3:** The running mean of the thin and thick disk trends as well as a  $1\sigma$  deviation. The width of the moving running mean boxes is set to be 10 % of the stellar sample.

# Appendix D

## Conference

During the period of this work I attended the *Chemical Evolution and Nucleosynthesis Across the Galaxy* (CENAG)- conference in Heidelberg (26-30 November, 2018, <http://www2.mpia-hd.mpg.de/homes/cenag2018/>). I presented a poster at the conference (see below) and won the best poster prize, allowing me to give a 15 minute talk about my work.




### Neutron Capture Elements in the Local Disk determined from 500 giant stars

Rebecca Forsberg & Henrik Jönsson  
Lund Observatory, Departments of Astronomy & Theoretical Physics, SE 221-00, Lund, Sweden  
For more information, please contact: rebecca.forsberg.89@student.lu.se

---

#### Overview

We present preliminary results from our ongoing project to determine the abundances of neutron capture elements in local giant stars. The purpose of this effort is threefold: **firstly**, we want to identify and eliminate possible systematic uncertainties when analysing giants such that these luminous stars can be used to determine the chemical evolution of more distant stellar populations with high accuracy (e.g. the inner/outer disk, the bulge). **Secondly**, we aim to provide a reference sample of giant stars for validation of the automatic chemical analysis of ongoing and planned big spectroscopic surveys (e.g. APOGEE). **Thirdly**, this work will provide input to Galactic chemical evolution modelers and might help put constraints on the formation channels of the relatively poorly understood neutron capture elements.



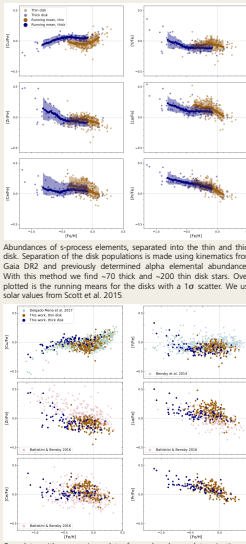
#### Which Elements?

**Cu: weak s-process**  
The weak s-process has a primary production channel in supernova type II and a secondary process in massive stars.

**Y, Zr: main s-process, 1st peak**  
The production of the main s-process elements takes place in thermal pulses in low-intermediate mass AGB-stars. The neutron source differs between main- and weak s-process, due to the temperature of the stars.

**La, Ce, Pr: Main s-process, 2nd peak**  
The first, second and third peak of the s-process is found at the stable magic numbers of nuclei with  $N = 50, 82$  and 126. For the third peak, we have not found any suitable lines in our giant stars.

**Nd, Sm, Eu, Gd: main s/r-process (upcoming work)**  
The r-process becomes more important in the production of heavier elements. The formation location is proposed to be transient events, such as neutron star mergers and supernovae.



#### Stellar Sample


We have observed our targets using the **FIES spectrograph** at the Nordic Optical Telescope, La Palma.

<b>Present sample</b>	~300 stars
<b>Final sample</b>	~500 stars
<b>Spectral range</b>	4100-7360 Å
<b>Resolution</b>	67000

We are currently determining the stellar parameters and abundances from newly observed targets, giving a final sample of **500 high resolution giant stars**.

#### Methodology

We make a detailed abundance analysis with thorough determination of the stellar parameters and abundances from the spectra using the code Spectroscopy Made Easy (SME). A careful placement of the local continuum and investigation of blends is done.



#### Continued Work

We will continue determining the abundances of 200 newly observed targets and include more s- and r-process elements, such as neodymium, samarium, europium and gadolinium, in the analysis. By comparing s- and r-process elements with each other and our results with current evolutionary galactic models we can get a better understanding of neutron capture elements and our galaxy.

#### Why Giant Stars?

We use K-giants as tracers in this work since they preserve their initial chemical composition. Spectroscopic analysis of giants can, however, be complicated; compared to dwarfs, giants have:

- More lines** in the spectra, making the placement of the zero level, the continuum, more difficult, and increases the risk of blending lines.
- Stronger spectral lines**, increasing the risk of lines of interest being saturated, which can give rather large uncertainties in the determined abundances.

Comparisons to abundance trends of published work using dwarf stars convince us that we are overcoming these obstacles.